

Analysis of physiological signaling mechanisms in reproductive and neuronal systems

Von der Fakultät für Mathematik, Informatik und Naturwissenschaften der RWTH Aachen
University zur Erlangung des akademischen Grades einer Doktorin der Naturwissenschaften
genehmigte Dissertation

vorgelegt von

Master of Science
Nadine Mundt

aus Düren-Birkesdorf

Berichter: *Prof. Dr. rer. nat. Marc Spehr*
Prof. Polina Lishko, Ph.D.

Tag der mündlichen Prüfung: 20.08.2021

Diese Dissertation ist auf den Internetseiten der Universitätsbibliothek verfügbar.

Table of Contents

1 Introduction.....	1
1.1 <i>The male reproductive system</i>	1
1.2 <i>Olfaction</i>	13
1.3 <i>Aims</i>	26
2 Materials and methods.....	30
2.1 <i>Reagents</i>	30
2.2 <i>Solutions and buffers</i>	33
2.3 <i>Antibodies</i>	36
2.4 <i>Primers</i>	36
2.5 <i>Plasmids</i>	37
2.6 <i>Equipment</i>	39
2.7 <i>Software</i>	41
2.8 <i>Mouse strains</i>	41
2.9 <i>Cell lines</i>	42
2.10 <i>Human sperm donation and sperm processing</i>	42
2.11 <i>Preparation of acute AOB and MOB slices</i>	43
2.12 <i>Preparation of acute VNO vibratome slices</i>	44
2.13 <i>Electrophysiology</i>	44
2.14 <i>Optogenetic stimulation of axon terminals in the OB</i>	50
2.15 <i>Synthesis of recombinant darcin</i>	51
2.16 <i>Ectopic expression of V2R27 in the VNO</i>	53
2.17 <i>Ca²⁺ Imaging</i>	53
2.18 <i>Whole-mount seminiferous tubule imaging</i>	55
2.19 <i>RT-PCR and Cloning</i>	56
2.20 <i>Immunochemistry</i>	56
2.21 <i>Immunoblotting</i>	58
3 Results	60

<i>Project A: ATP activation of peritubular cells drives testicular sperm transport</i>	60
<i>Project B: Electrophysiological characterization of "DSper"</i>	69
<i>Project C: Establishing an optogenetic stimulation paradigm in the murine olfactory bulb</i>	88
<i>Project D: Decoding of receptor-ligand interactions in the VNO</i>	98
4 Discussion	108
<i>Project A: ATP activation of peritubular cells drives testicular sperm transport</i>	108
<i>Project B: Electrophysiological identification of "DSper"</i>	110
<i>Project C: Establishing an optogenetic stimulation paradigm in the murine olfactory bulb</i>	116
<i>Project D: Decoding of receptor-ligand interactions in the VNO</i>	117
5 Summary	120
6 Abbreviations	121
7 Contributions by others	123
8 Funding	124
9 References	125
10 Acknowledgement	151
11 Curriculum vitae	153
12 Eidesstattliche Erklärung	157

1 Introduction

In biology, a "signal" is defined as an entity that codes or conveys information in living organisms. The sensing and processing of information are vital since they integrate and coordinate the function of the many individual cells that make up an organism. In this sense, signals can be exchanged between cells (i.e., endo-/paracrine signaling), directed at the same cell (i.e. autocrine signaling), or simply be provided by external environmental factors. Biological processes are so complex that they require many such signals, and signaling pathways are found in each living organism. Sensing and processing information is enabled by various signaling molecules and the corresponding receptors expressed on a cell's surface. Each cell is programmed to respond to a set of signals, which usually entails the following steps:

1. Synthesis and release of the signal by the initiator cell or environment
2. Transport of the signal to its target
3. Binding of the signal by a specific receptor leading to its activation
4. Initiation of signal-transduction pathways inside the target cell [1].

Understanding signaling pathways provides fundamental knowledge of an organism's physiology and pathology. This body of work aims to investigate a set of exemplary signaling mechanisms in reproductive and neuronal systems.

1.1 The male reproductive system

The mammalian testes are paired genital organs, which play an essential role in both steroid synthesis and production of haploid germ cells. Each testis is surrounded by a connective tissue capsule, the *tunica albuginea*, and is structurally compartmentalized in extensively coiled tubules [2] (Fig. 1.1). These "seminiferous tubules" comprise up to 16-26 m/cm³ in mice

1 Introduction

[3] and constitute the functional unit of sperm production. In several stereotyped mitotic and meiotic divisions, collectively referred to as "spermatogenesis", diploid germ line-derived stem cells (i.e., spermatogonial stem cells, SSCs) develop into haploid germ cells, spermatozoa. Spermatogenesis is a continuous process extending throughout a man's fertile years. Given its significance for male fertility, it is surprising how rudimentary our current knowledge about this intricate sequence of massive cell proliferation and differentiation still is.

Spermatogenesis takes place within a highly specialized environment, the seminiferous epithelium. A heterogeneous pool of germ cells is supported by somatic Sertoli cells that span the seminiferous epithelium from the basal lamina to the lumen and fulfill essential nutritive and regulatory functions [2]. Due to their large surface area, Sertoli cells can support and nourish 30-50 germ cells [4]. Via tight junction formation between Sertoli cells, the "blood-testis-barrier" controls diffusion inside the tubules, thereby providing a protective environment for maturing germ cells. The blood-testis-barrier prevents autoimmune responses directed against developing spermatozoa and, thus, ensures constant gamete supply.

Developing germ cells are distributed from the basal to the adluminal compartment according to their developmental stage (Fig. 1.1). A_{single} spermatogonia are considered *bona fide* SSCs, a pool of undifferentiated, continuously self-renewing stem cells [5]. A_{single} spermatogonia will divide mitotically into various types of spermatogonia (A_{paired} to A_{aligned} to type-B), which are considered irreversibly committed to differentiating [6]. Type B spermatogonia detach from the basal lamina and enter meiosis as preleptotene spermatocytes [7]. During subsequent meiotic divisions and morphological maturation steps, germ cells progress from primary to secondary spermatocytes, to round spermatids, and eventually to elongated spermatids.

Spermatogenesis is schematized by sequential cellular "stages" that progress in a wave-like fashion through a coordinated repeating cycle [8]. Each stage contains a distinct subset of maturing germ cells. In mice, each spermatogenic cycle comprises 12 stages with an average duration of 8.7 days for completion [9]. It takes 4.5 cycle repetitions (39 days) for

1 Introduction

complete spermatogenesis and release of immotile, haploid spermatozoa into the seminiferous tubule lumen (spermiation).

The peritubular space contains blood vessels, lymphatics, and sparse neuronal innervation [10], [11]. Leydig cells are scattered in groups in the peritubular compartment and serve a critical function in steroid synthesis and regulation of intra-tubular signaling pathways. The seminiferous tubules converge in the *rete testis*, which terminates in the *ductuli efferentes*. Immotile spermatozoa pass the *ductuli efferentes* to reach the epididymis, where they undergo further maturation steps [2]. Due to acidic epididymal pH, spermatozoa are stored in a quiescent state [12], [13]. Upon ejaculation, they are mixed with seminal fluid which renders spermatozoa motile [14].

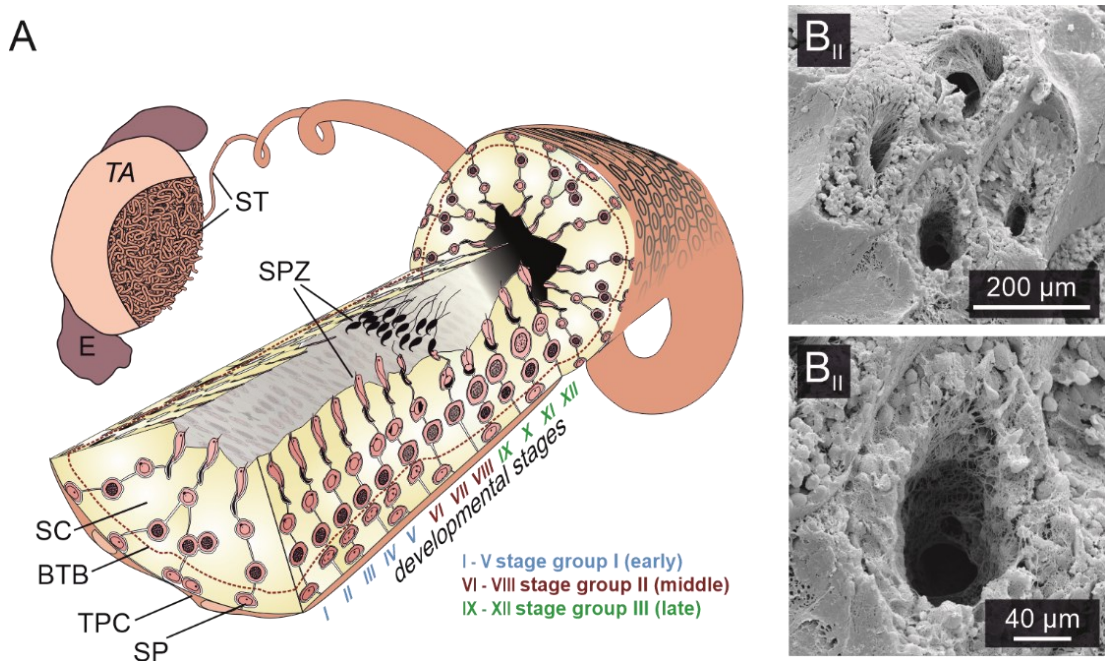


Figure 1.1: Cellular architecture of the mammalian seminiferous tubule. (A) Schematic illustration of the seminiferous tubule (ST) highlighting 12 consecutive stages (I – XII) of the spermatogenic cycle [8] along the length of the tubule. A single layer of flat testicular peritubular cells (TPC) lines the tubular wall. Sertoli cells (SC) span the tubule from the basal lamina to the lumen. Developing germ cells (GC) are distributed between Sertoli cells. Spermatogonia are located near the basal membrane. Prophase spermatocytes move across the blood-testis barrier (BTB) to the adluminal compartment, where they complete meiosis. The resulting haploid spherical cells (round spermatids) differentiate into elongated spermatids and, eventually, into highly condensed and compartmentalized spermatozoa. These mature yet still immotile germ cells are then released into the lumen (spermiation). E, epididymis; TA, tunica albuginea; adapted from [15]. (B) Freeze-fracture scanning electron microscopy

1 Introduction

images of testicular tissue samples from adult mice. The seminiferous tubule's dimensions and the epithelium's complex anatomy and fully developed lumen become apparent; provided by [16].

1.1.1 The role of purinergic signaling within the testis and putative implications in peritubular cell contractions

Being ubiquitously synthesized in all mammalian cells, adenosine triphosphate (ATP) serves as an important intracellular source of free energy involved in various metabotropic cycles. Moreover, ATP acts as an extracellular ligand by activation of P2 purinoceptors [17]. Purinergic signaling is involved in a cohort of physiological events, such as contractions of smooth muscle cells [18] and cardiac myocytes [19], as well as immune cell function [20]. Apart from that, a growing body of evidence suggests widespread purinergic signaling within the mammalian testis. Expression of different P2 purinoceptor isoforms has been reported in Leydig cells [21], [22], Sertoli cells [23], both pre- and postmeiotic germ cells [16], [24], [25], human testicular peritubular cells (hTPCs) [26], as well as murine spermatozoa [27]. Due to a lack of direct, live-cell approaches, however, demonstration of a functional role of P2 receptor expression is often lacking.

ATP-gated P2 purinoceptors are subdivided into two classes, namely P2X, a family of ionotropic P2 receptors [28], [29], and P2Y, a metabotropic receptor family [30], [31]. P2Y receptors belong to the superfamily of G-protein-coupled receptors (GPCR). The majority of P2Y receptors couple to $G_{\alpha q}$, thus activating Phospholipase C (PLC), which in turn hydrolyzes phosphatidylinositol-4,5-bisphosphate (PIP₂) to inositol-1,4,5-trisphosphate (IP₃) and diacylglycerol (DAG). IP₃ eventually triggers Ca²⁺ release from internal stores. P2X receptors are members of the ligand-gated cation channel (LGCC) superfamily. Upon ATP-binding, conformational changes lead to the opening of a cation-permeable channel pore [32]. All P2X isoforms share substantial Ca²⁺ permeability but are easily distinguished by ligand affinities, desensitization kinetics, and pharmacological fingerprints [33].

In mice, both Sertoli and germ cells were reported as a source for extracellular ATP [34], [35] and cellular secretion may itself be under endocrine control [35], [36]. However, the mechanism(s) of cellular ATP release remains subject to debate.

1 Introduction

Once detached from the Sertoli cells, sperm must be transported to the *rete testis* and epididymis for final maturation. Given that spermatozoa are still immotile upon spermiation, precisely regulated tubular transport mechanisms are indispensable for male fertility [15]. Testicular peritubular cells (TPCs) are smooth muscle-like cells (myoid cells), which combine with the extracellular matrix and form a small tubule-surrounding compartment [37], [38]. Due to their contractile character, TPCs are attractive candidates for mediating sperm transport along the tubules. This idea has gained widespread support from several, mostly indirect, *in vitro* studies [39]–[42]. However, quantitative physiological measurements of seminiferous tubule contractions are rare and controversial [43]–[46].

Several P2 receptor isoforms affect smooth muscle cell physiology, with P2X1, P2X2, P2X4, P2X7, P2Y1, and P2Y2 acting as the principle subunits [47]. Whether mouse TPC physiology is also under purinergic control and putative ATP-induced tubular contractions could mediate sperm transport is an intriguing notion.

1.1.2 Fertilization

Fertilization ranks amongst the most fundamental processes in life. Upon fertilization, two haploid gametes (ovum and spermatozoon) fuse and restore the original diploid set of chromosomes, thereby combining maternal and paternal genetic information, which initiates the development of a new organism. In contrast to aquatic organisms, terrestrial animals release male germ cells directly into the female reproductive tract, a confined and strictly regulated environment [2]. To gain complete fertilizing competence, spermatozoa must undergo final maturation steps, collectively termed "capacitation". The female reproductive tract orchestrates these processes, thus defining it as an active male gamete recipient with the capacity to select and orient sperm [48].

The molecular mechanisms, that allow spermatozoa to successfully navigate to the egg, demand the sperm cell detects environmental signals and adapts its motility accordingly. Here, fundamental regulatory parameters are sperm intracellular pH, membrane voltage, and cytosolic Ca^{2+} concentration $[\text{Ca}^{2+}]_i$ collectively controlled by ion channels and transporters in the sperm plasma membrane [49].

1.1.3 Sperm morphology

Due to their unique morphology, physiology, and given role in reproduction, spermatozoa have fascinated researchers since their discovery in 1677 by Antoni van Leeuwenhoek [50]. A spermatozoon defines a haploid cell that harnesses ATP-driven motility to deliver its genetic information to its female counterpart, the ovum.

Mammalian spermatozoa have a diverse yet simple morphology comprising two structural elements: the head-region, tightly packed with DNA, and the flagellum that accounts for motility [2] (Figure 1.2). The sperm head consists of a condensed nucleus and the acrosome – a Golgi-derived vesicle. Exocytosis of the acrosomal vesicle (i.e., the acrosome reaction) happens upon contact with the egg's protective vestments. Hydrolytic enzymes released by the acrosome digest the egg-surrounding *zona pellucida*, facilitating sperm motion towards the egg's surface [51]–[53].

Structurally similar flagella are present in all spermatozoa across the animal and plant kingdom [53]. They resemble the classical structure of a motile cilium with a central axoneme (9+2 microtubule assembly) and specialized structural components such as the molecular motor dynein, that drives flagellar bending. According to the "geometric clutch model", dynein arms pull and push on outer microtubule doublets and induce strain force that causes the flagellum to bend [54], [55]. Microtubule sliding is powered by ATP hydrolysis, a pH-dependent process augmented by an elevation of intraflagellar Ca^{2+} [56]–[60]. Therefore, sperm $[\text{Ca}^{2+}]_i$, pH, and ATP are the key regulatory elements of motility changes [61]. The flagellum is tripartite as it comprises the mitochondria containing midpiece, the principal piece, which is primarily responsible for motility, and the endpiece with few structural components [62]. A circular septin structure - termed "the annulus" - separates the midpiece and principal piece, thus restricting laminar diffusion of plasma membrane proteins between those two flagellar compartments [63] (Figure 1.2 C). The sperm plasma membrane is tightly attached to all underlying structures. Many membrane-located proteins appear to be anchored to the underlying fibrous sheath, ensuring their strict compartmentalization. The so-called "cytoplasmic droplet" (CD; ~1-2 μm diameter), a remnant of the precursor cell's

1 Introduction

cytosol [64], represents the only region in which the plasma membrane is loosely attached to the cytoskeleton. Located at the midpiece-region, the CD is likely to serve as a reservoir for adaptation to osmotic stress and, in contrast to other species, many human spermatozoa retain their CD after ejaculation [64]. This small area of plasma membrane bears a technical advantage since the CD allows for the formation of a tight, gigaohm contact between sperm membrane and the recording electrode during sperm patch-clamp approaches [49], [65], [66] (see chapter 2.13.2).

As spermatozoa migrate through an environment of changing pH, osmolarity, and stimulating extracellular cues, sperm ion channels control membrane potential and cytosolic ion concentrations to regulate hyperactivation of motility and trigger physiological responses like capacitation and the acrosome reaction.

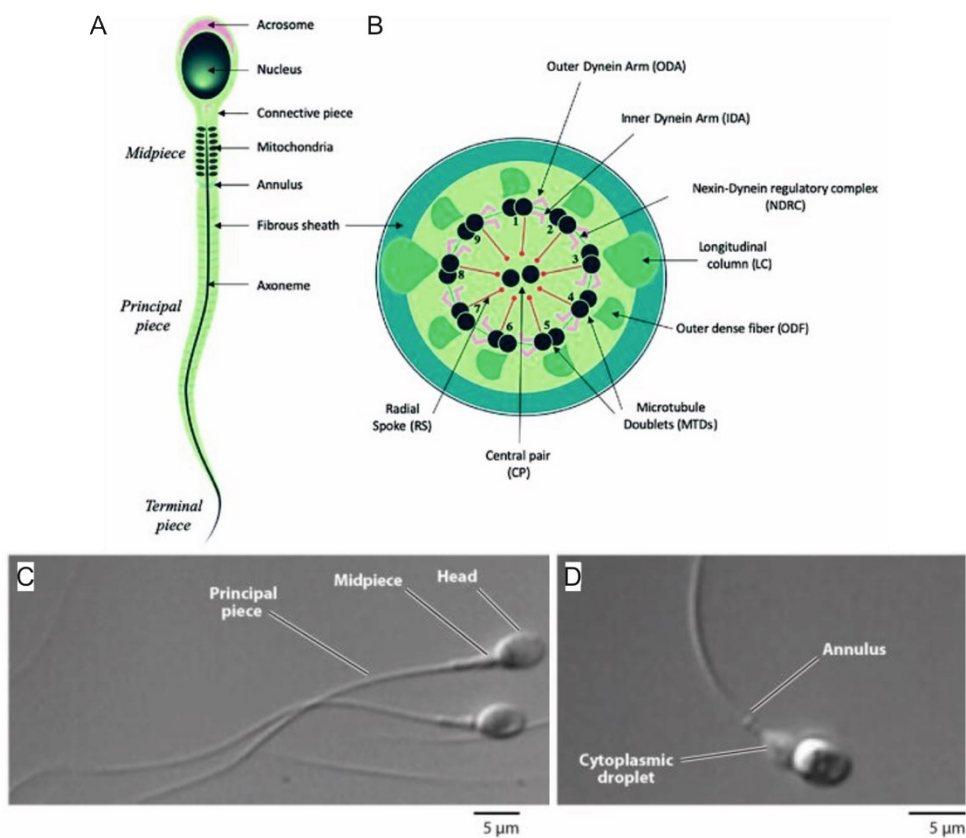


Figure 1.2: Morphology of human spermatozoa. (A) Schematic illustration of a human spermatozoon shows structural components of the head- and tail-region. Note that the cytoplasmic droplet is not shown; (B) Cross-section from the principal piece of the flagellum

1 Introduction

shows the axoneme's organization with classical 9+2 microtubule assembly. Dynein motor proteins slide along outer microtubule doublets to elicit flagellar bending - a process that is enhanced by intraflagellar Ca^{2+} (C) DIC image of human spermatozoa with the head, the midpiece, and the principal piece as indicated (D) Human spermatozoon with cytoplasmic droplet and annulus labeled (Adapted from Touré (2019) and Lishko et al. (2012) [67], [68])

1.1.4 Interdependency of ion channel complexes in the human sperm flagellum

Ca^{2+} conductance

Ca^{2+} is of great importance for intracellular signaling processes in all cell types, sperm being no exception [69]. Therefore, maintaining a low cytosolic Ca^{2+} level is essential to enable fine-tuned regulation of downstream Ca^{2+} -induced responses. This prerequisite is carried out by exchangers, ion channels, or organelles that conduct, import, export, or sequester Ca^{2+} ions. Although basic sperm motility, which is produced by symmetrical bending of its flagellum, occurs at low (nanomolar) $[\text{Ca}^{2+}]_i$, elevation of cytoplasmic Ca^{2+} triggers changes dynein motor protein behavior resulting in an asymmetric and high-amplitude flagellar beat pattern with enhanced swimming force. This whip-like bending is commonly referred to as "hyperactivation" and is vital for the sperm's ability to detach from the cilia of the ampullar oviduct [70] and to overcome the egg's protective vestments during fertilization [71].

Before 2001, voltage-gated Ca^{2+} -channels (Cav) were thought to carry out the major Ca^{2+} conductance in sperm flagella. This notion was supported by electrophysiological identification of Cav channels in testicular precursor cells [13]. However, they fulfill a redundant function since male mice deficient in Cav2.2, Cav2.3, and Cav3.1 are entirely fertile [73]–[75].

In 2001, the first member of an undescribed family of Ca^{2+} -selective ion channel subunits was discovered. Exclusively expressed by sperm cells, CatSper1 was found to be essential for male fertility [76]. The heteromeric CatSper (cation channels of sperm) topology comprises four pore-forming α -subunits (CatSper1-4) plus at least six auxiliary subunits (CatSper β , CatSper γ , CatSper δ , CatSper ϵ , CatSper ζ , and EFCAB9), of which CatSper1-4, CatSper δ , and CatSper ζ are indispensable for proper channel formation and function [76]–[82]. Sperm cells isolated from mice deficient for any of these mentioned CatSper subunits have no measurable CatSper

1 Introduction

current ($I_{CatSper}$). Furthermore, they share an identical male infertility phenotype due to loss of hyperactivated motility [79]. Humans with mutated CatSper1 or CatSper2 genes are also infertile, revealing CatSper's importance as a general mammalian fertility component [83]. The establishment of the sperm patch-clamp technique in 2006 enabled the recording of CatSper activity for the first time and identified CatSper as the main Ca^{2+} channel in mouse [84] and human sperm [85]. Recordings from fragments of mouse spermatozoa revealed that $I_{CatSper}$ originates from the flagellar principal piece [84], concurring with the localization of CatSper1 using immunocytochemistry.

Human CatSper (hCatSper) channels exhibit weak voltage-dependency with half-maximal activation ($V_{1/2 \text{ human}}$) at +85 mV. Given this unusually high $V_{1/2}$, only a small fraction of hCatSper channels are open at physiological-relevant membrane potentials. Murine CatSper exhibits pronounced pH_i gating, as intracellular alkalinization from 6.0 to 7.0 induced a sevenfold increase of murine $I_{CatSper}$, corresponding to a 70 mV leftward shift of $V_{1/2 \text{ mouse}}$ [84]. hCatSper is potently activated by intracellular alkalinization as well. The abundance of histidine residues in the CatSper1 N-terminal domain is likely the cause for its pH_i sensitivity.

Given its high $V_{1/2}$, hCatSper requires an additional activation-mechanism to induce significant CatSper currents at physiological membrane potentials [86]. As indicated by Brenker *et al.* [87], CatSper serves as a polymodal sensor for various chemical cues, e.g. neurotransmitter, chemokines, and odors, which may potentiate CatSper activity and assist sperm during their voyage across the female reproductive tract. In their recent work, Miller *et al.* (2016) [88] revealed the mechanistic basis of a non-genomic fast potentiation effect of progesterone (P4, $EC_{50} \sim 7.7 \text{ nM}$) [89] on hCatSper. P4, a steroid hormone released by the ovaries and cumulus cells surrounding the egg, induces robust Ca^{2+} influx into human sperm [90] and triggers both hyperactivation [89] and the acrosome reaction [91]. Miller and coworkers revealed mechanistic details of indirect P4 action on CatSper. The human sperm P4 receptor was characterized as the orphan enzyme ABHD2 (alpha/beta hydrolase domain-containing protein 2) that acts as P4-dependent lipid hydrolase. ABHD2 activation leads to depletion of 2AG (endocannabinoid 2-arachidonoylglycerol) from the sperm plasma membrane, which relieves 2AG inhibition of CatSper and therefore causes Ca^{2+} influx [88].

1 Introduction

Together, voltage, pH_i , and P4 collectively regulate CatSper-mediated Ca^{2+} influx, while other, yet undescribed, regulatory mechanisms may exist.

CatSper is organized in quadrilateral longitudinal nanodomains along the sperm flagellum in both mice and humans [81], [82], [92], [93]. Notably, dSTORM microscopy revealed colocalization with ABHD2 along those quadrilateral axes. Hv1, the sperm proton channel, is responsible for local alkalization and distributed asymmetrically within bilateral longitudinal lines. Hv1 inhibition results in decreased sperm rotation along its longitudinal axis. Thus, the distinct compartmentalization of sperm signaling units is thought to provide the structural basis for selective activation of CatSper and subsequent flagellar rotation [61].

Proton conductance

Intracellular alkalization is a critical component in various sperm physiological processes, e.g. hyperactivation, acrosome reaction, capacitation, and chemotaxis. Even basal sperm motility is pH-sensitive, as dynein's ability to hydrolyze ATP and induce flagellar bending significantly increases with rising pH_i . Sperm motility and pH_i are inversely proportionally related, since the motile flagellum continuously generates protons via glycolysis, ATP hydrolysis, and $\text{H}^+/\text{Ca}^{2+}$ exchange [53]. Therefore, sperm requires a mechanism to compensate for intracellular acidification. Lishko *et al.* (2010) revealed a large voltage-activated outward rectifying H^+ current via direct patch-clamp recordings from human sperm cells [85]. The aptly named HSper (H^+ channel of sperm) is highly proton selective, activated by membrane depolarization, governed by pH-gradients across the plasma membrane, and significantly inhibited by extracellular Zn^{2+} . These biophysical properties identify HSper as the voltage-gated proton channel Hv1. Hv1 is not a traditional ion channel but rather a hybrid between a transporter and an ion channel without a classical pore. Molecular dynamic simulations of Hv1 homology models indicate that Hv1 conducts via an internal water wire inside the voltage-sensing domain and movement of the charged S4 helix [94]–[96].

Hv1 is known to form dimers, though each Hv1 subunit can function independently as a voltage-gated proton channel [94]. Hv1 channels are abundantly expressed in human sperm cells within the principal piece, located along bilateral longitudinal axes [61]. This distribution

1 Introduction

makes Hv1 ideally positioned to activate pH-dependent proteins of the axoneme and adjacent plasma membrane ion channels, e.g., CatSper, by conducting H^+ unidirectionally to the extracellular space and producing local alkalization. An additional role assigned to Hv1 is regulating intracellular Ca^{2+} homeostasis. A flagellar Ca^{2+} -ATPase exports cytoplasmic Ca^{2+} ions entering through CatSper. This process is accompanied by the import of extracellular H^+ , which results in intracellular acidification and can cause CatSper inhibition. Hv1 might function as a critical component to balance this scenario.

Full-length Hv1 and an N-terminal cleaved variant of Hv1 have been reported in human sperm [97], of which both forms are activated by a combination of pH gradient and membrane depolarization [85]. As there is a permanent outward chemical gradient for protons, sperm membrane potential might be a major determinant of Hv1 activity.

Potassium conductance

Since both Hv1 and CatSper activity are regulated by membrane depolarization, a mechanism that sets and regulates voltage is vital for fertility. Non-capacitated epididymal murine sperm cells are slightly depolarized (-40 mV). During capacitation, the membrane potential is changed to more hyperpolarized values of -60 mV. This shift is attributed to increased potassium permeability [98]. CatSper permeability would be inconsequential under resting conditions, even under slight alkaline pH-values. Therefore, the molecular origin of membrane depolarization is of significant importance and possibly linked to the inhibition of membrane potassium channels. The identity of the principal human potassium channel (KSper) has been first suggested by Mannowetz *et al.* (2013), who recorded a Ca^{2+} -sensitive potassium current in ejaculated human spermatozoa [99]. The biophysical properties and pharmacological profile of human KSper resembled hybrid characteristics of the mouse sperm potassium channel, SLO3, which is pH-sensitive, and SLO1, which is Ca^{2+} -sensitive. This unusual combination has resulted in controversy regarding the exact molecular composition of human KSper [92], [99], [100]. One possibility is the formation of Slo1/Slo3 heteromers that carry out the principal potassium conductance in human sperm flagella. Uncovering the

1 Introduction

precise molecular basis of hKSper remains an essential step towards a general understanding of sperm membrane potential control. Intriguingly, the hKSper-mediated current can be inhibited by micromolar concentrations of extracellular P4 ($EC_{50} = 7.5 \mu M$)[99], a proposed mechanism to induce membrane depolarization and voltage-driven activation of Hv1 and CatSper [99].

The unknown origin of sperm membrane depolarization

P4 has been shown to potentiate CatSper activity by shifting $V_{1/2}$ to more negative membrane potentials [89]. However, CatSper still requires intracellular alkalization and membrane depolarization to function properly. Hv1 was revealed as the principal pH_i regulator. By transporting protons unidirectionally to the extracellular environment, Hv1 represents a key component in the CatSper activation cascade, but it can also cause membrane hyperpolarization by exporting positive charges out of the cell. Since Hv1 is also voltage-dependent and requires membrane depolarization to be activated, it must rely on yet unidentified depolarizing ion channels.

Given its inhibitory effect on KSper [99], P4 is one of the potential origins for membrane depolarization. However, depolarization by KSper inhibition would result in Hv1-mediated H^+ efflux that would counterbalance KSper-mediated depolarization by hyperpolarizing the membrane. Hv1 therefore represents a negative feedback loop inhibiting both itself and CatSper. Furthermore, efficient KSper inhibition requires micromolar concentrations of P4, which are only present in close vicinity of the egg. Sperm hyperactivation, however, occurs in the fallopian tubes, where P4 concentrations are insufficient to block KSper [101]. Hence, the current model is missing a fourth member – the "Depolarizing Channel of Sperm" (DSper) [102], [103]. Activation of this hypothesized DSper ion channel would induce long-lasting membrane depolarization and provide the necessary positive net charge influx for CatSper/Hv1 activation. Despite its central role, the molecular correlate of DSper remains elusive.

1.2 Olfaction

A species' evolutionary success has been primarily determined by its ability to adapt to its environment. As a logical corollary, the detection and processing of environmental cues that lead to a percept of the outside world, is a critical requirement in doing so. The detection of volatile and nonvolatile chemical cues is guided by the olfactory system, a highly conserved sensory system found in fish, amphibians, reptiles, insects, and mammals [104]–[109]. Olfaction plays a vital role in detecting and evaluating food sources, locating suitable mating partners, and avoiding predators, which ultimately ensures the survival of both the individual and the species [110]. To cope with the staggering heterogeneity of stimuli that must be identified, the olfactory system has evolved into several distinct anatomical subsystems [111]–[114], that are depicted in Figure 1.3. These include the main olfactory epithelium (MOE), the vomeronasal organ (VNO), the Grüneberg ganglion (GG) [115], and the septal organ of Masera (SO) [116]. Each subsystem is made of sensory neurons in a defined location within the nasal cavity, is endowed with a distinct set of chemosensory receptors and signal transduction pathways, and projects to specific regions within the olfactory forebrain [114]. According to the dual olfactory hypothesis [117], the MOE is defined as the primary detector of general volatile odors, while the VNO is regarded as a detector for nonvolatile social cues (i.e., pheromones). This established orthodox theory, however, has been challenged by several more recent studies that suggest an overlapping set of activators for both subsystems [118]–[124].

The GG is likely to detect gaseous or other highly membrane-permeant stimuli, since GG neurons lack direct access to the nasal lumen [112]. Despite its discovery decades ago, the SO's functional role is still enigmatic [114].

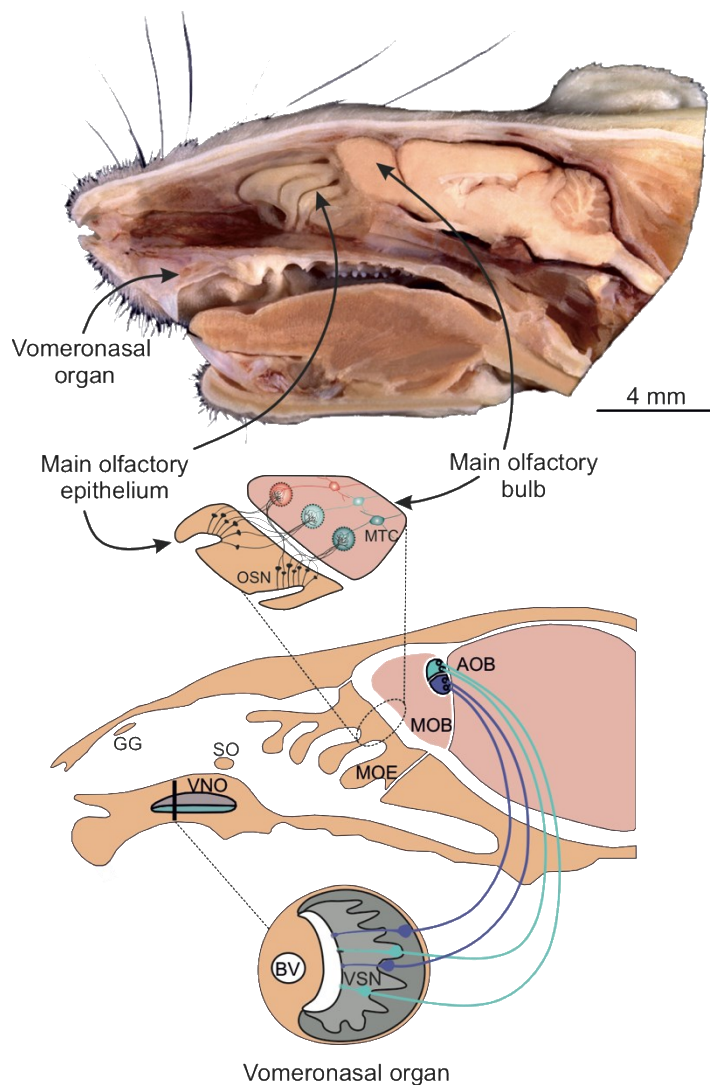


Figure 1.3: Anatomical organization of the olfactory system in rodents. Top: Sagittal cross-section of a mouse head showing the vomeronasal organ (VNO) at the base of the nasal septum, above the palate. The main olfactory epithelium (MOE) lines the posterior part of the nasal septum and the endo-turbinates' dorsolateral surface. The olfactory bulb (only the main bulb here, MOB) is located in the olfactory forebrain and is separated from the MOE by the porous cribriform plate (CP) (image kindly provided by Adam C. Puche) Bottom: Simplified schematic illustration of the above image showing the organization of the rodent nose into chemosensory subsystems with the MOE, VNO, septal organ (SO) and Grüneberg ganglion (GG). Vomeronasal sensory neurons (VSNs) project their axons to the accessory olfactory bulb (AOB). An enlarged depiction of the MOE illustrates how olfactory sensory neurons (OSNs) converge in a receptor-dependent pattern onto mitral and tufted cell (MTC) dendrites in the MOB. (Adapted from: Spehr et al. (2006) [123])

1.2.1. The Main Olfactory System

The best-studied and, thus, termed "main olfactory system" consists of the MOE as the peripheral sensing unit, and the main olfactory bulb (MOB), the first central processing station

1 Introduction

in the forebrain. The MOE is located in the posterior region of the nasal cavity and lines the dorsal nasal septum and the dorsolateral surface of the endoturbinates [123]. The MOE's chemosensory function is carried by olfactory sensory neurons (OSNs). Apart from OSNs, the MOE harbors sustentacular cells that nourish and communicate with OSNs [125], and basal cells, which serve as OSN precursor cells [126].

In the MOB, OSN axons target discrete spherical neuropil structures called glomeruli. This happens in a receptor-dependent pattern: axons of all OSNs expressing a given receptor converge in 1-2 glomeruli per bulb, which creates an odotopic map (Fig. 1.4). Thus, a given odor signal will result in a specific spatiotemporal glomerular activation pattern and integration of OR-specific sensory information [127]–[129]. The odotopic map is largely conserved between individuals [130]. In a given glomerulus, OSN axons form synaptic connections with apical dendrites of both mitral cells (MCs) and tufted cells (TCs), the principal MOB projection neurons [131]. At this stage, one mitral/tufted cell (MTC) receives input within a single glomerulus and one glomerulus is innervated by a single mitral/tufted cell. Thus, the incoming olfactory signal of a given receptor population is integrated by a single MTC, highlighting their importance in olfactory coding (Fig. 1.4) [132]. Extensive microcircuit formation between MTCs and local interneurons process the incoming olfactory information before it is relayed to higher brain centers of the ipsilateral hemisphere. MTCs project to the primary olfactory cortex, which includes the piriform cortex, entorhinal cortex, anterior olfactory nucleus, olfactory tubercle, and lateral amygdala [113], [131], [133]–[135].

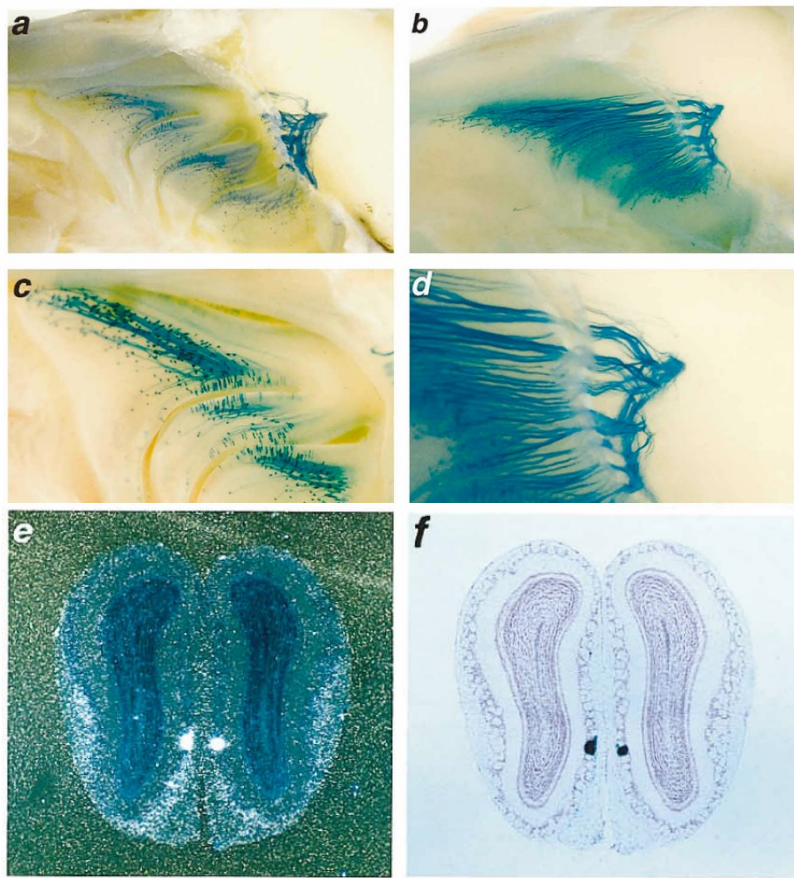


Figure 1.4: MOE and MOB of the P2-IRES-tau-lacZ mouse-line: X-Gal staining visualizes axons of the P2-receptor neuron population converging into one glomerulus per medial MOB. (a) Whole-mount view of the wall of the nasal cavity and the medial aspect of the bulb (b) View of the nasal septum and the medial aspect of the bulb (c) Higher power view of the turbinates (d) Higher power view of the glomerulus (e-f) Adjacent coronal sections through olfactory bulbs, subjected to *in-situ* hybridization with a P2 probe (e) and X-Gal staining (f). P2 sensory input coalesces in one glomerulus per bulb. (From: Mombaerts et al. (1996) [127])

1.2.2 The Accessory Olfactory System

In most mammals, chemical cues have evolved as the predominant source for individuality information. This includes endocrine state, social status, sexual maturity, receptivity, as well as self-identification and discrimination of others [136]–[138]. Volatile or nonvolatile molecules that convey said information are considered "pheromones", a term that derives from the greek "φέρειν" (to carry) and "օρμόνη" (hormone, i.e. to excite, to stimulate) [139]. To detect and identify pheromones, animals are equipped with the accessory olfactory system (AOS), which consists of the peripheral vomeronasal organ (VNO) and the central accessory olfactory bulb (AOB). While we have a relatively clear understanding of peripheral and early central processing in the main olfactory system, the mechanistic principles of AOS function remain obscure.

The vomeronasal organ

Barring humans, some apes, dolphins, and whales, all mammalian and many nonmammalian species are equipped with a functional vomeronasal organ (VNO), that represents the site of pheromone detection and primary sensory transduction steps in the AOS [109], [138]. The VNO was first described in 1813 by the Danish anatomist Ludwig L. Jacobson, hence the alternative name "Jacobson's organ" [140].

The VNO is a paired encapsulated cylindrical organ (Fig. 1.5), situated just above the palate. Anatomically it is built as a blind-ended tube, which opens anteriorly to the nasal cavity via the vomeronasal duct [141], [142]. The current prevailing notion is that the lateral major blood vessel serves as a vascular pump to mediate pheromone uptake into the vomeronasal lumen [143], [144]. However, this idea is difficult to prove *in vivo*, given the VNO's challenging anatomical location.

The sensory epithelium of the VNO harbors 100.000 to 200.000 vomeronasal sensory neurons (VSNs) [145], which gain both structural and metabolic support from sustentacular cells, located in the most superficial layer of the crescent-shaped epithelium [146]. VSNs are bipolar cells with a basal unmyelinated axon and a single unbranched apical dendrite that emanates into the mucus-filled lumen to gain pheromone contact. VSN dendrites terminate in a paddle-shaped structure covered with sensory microvilli. The microvillar surface represents a vast expansion of the VSN interface with the external pheromone-containing environment. At the basal lamina, VSN axons fasciculate into the vomeronasal nerve. Together with OSN nerve fibers, VSN axon bundles enter the olfactory bulb through the cribriform plate, bypass the medial MOB and eventually reach the AOB glomerular layer (Fig. 1.5 B) [141], [147], [148].

1 Introduction

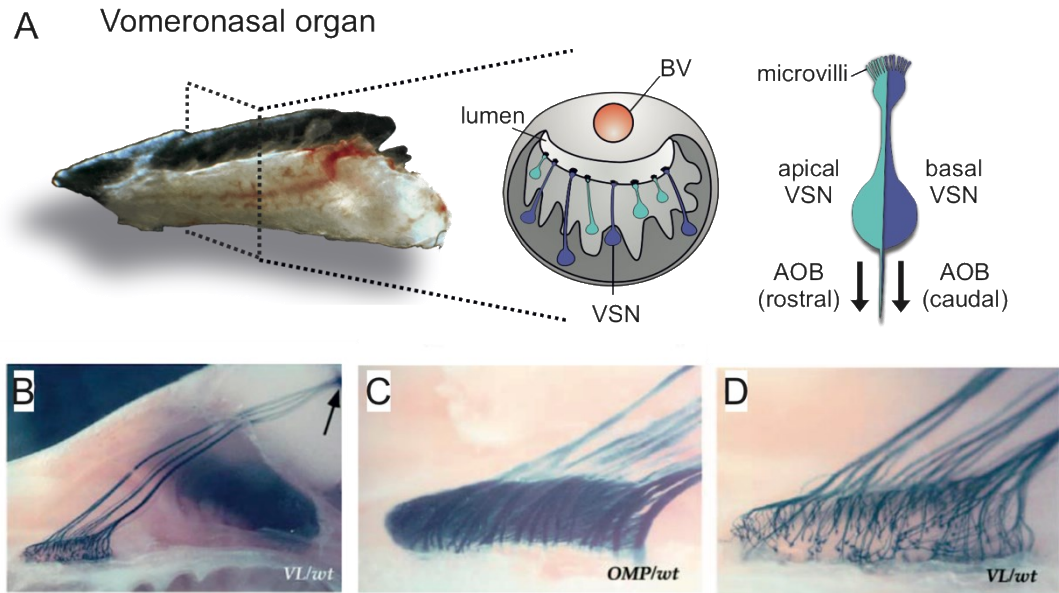


Figure 1.5: Anatomical organization of the vomeronasal organ. (A) The VNO consists of two symmetrical blind-ended tubes at the anterior base of the nasal septum. Vascular contractions of lateral blood vessels (BV) trigger suction of stimuli into the VNO lumen. Two subpopulations of microvillous vomeronasal sensory neurons (VSNs) reside in either the apical (turquoise) or basal (blue) layer of the sensory epithelium and extend their dendrites into the lumen. The spatial organization of apical and basal VSNs is maintained in the AOB, as apical VSNs project their axons to the rostral part of the AOB, whereas basal VSNs innervate the caudal AOB (adapted from Mohrhardt et al., (2018) [138]). (B-D) X-Gal staining visualizes axon trajectories of VSNs. (B) Whole-mount view of the right half of the head of a VR_i2-IRES-taulacZ mouse line, stained with X-gal. VR_i2-expressing neurons are labeled intense blue from the cell bodies (bottom left) to the axon terminals (top right). The arrow indicates the AOB. (C) Lateral whole-mount view of a VNO from a heterozygous OMP-taulacZ mouse. The entire VSN population becomes apparent. (D) Same whole-mount specimen as in (B) with a higher-power view of the VNO. Note that only a small selection of VSNs (VR_i2 expressing) is stained (from: Rodriguez et al., (1999) [148]).

Vomeronasal stimuli

In the past, the VNO was commonly referred to as a sole "pheromone detector" [120], [149], [150]. By definition, pheromones are semiochemicals secreted by one individual of a given species and received by a second individual of the same species, in which the pheromone initiates an innate behavioral or physiological response [139]. Pheromones thus mediate *intraspecific* communication. For the mammalian VNO, however, the idea of a sole pheromone detector is incomplete, since chemical signaling can also occur on an *interspecific* level by allelomones (greek "αλληλο-", of each other/reciprocal). Vomeronasal signaling is reportedly involved in predator odor detection and prey localization [151], [152].

1 Introduction

Furthermore, many chemosignals detected by VNO are not single compounds - as dictated by the original definition of a pheromone - but rather species-specific or individual-specific combinations of molecules in precise ratios [153]. And finally, although pheromones elicit innate and fixed responses in the recipient, behavioral responses to many AOS signals can require learning and neuronal plasticity [137], [154], [155]. Therefore, the former dogma has been revised and it is now clear that the VNO is not exclusively dedicated to pheromone detection [136], [156].

Sources for pheromones in mice are bodily fluids such as saliva, tears, urine, vaginal secretions, and other scent secretions [157]–[160]. Among those, much research focus has been attracted by urine as a source of both small volatile pheromones [157], [158], [161] and larger nonvolatile peptides or proteins [137], [155], [162]–[164]. 99% of the urine protein repertoire is comprised of members of the major urinary protein (MUP) family [165], [166]. Besides a plethora of small volatiles, urine also contains sulfated steroids [167], which are associated with the dynamic endocrine state of an individual, and major histocompatibility complex (MHC) class I peptide ligands, which represent an individually unique immunological fingerprint [168], [169].

The significance of MUPs can be appreciated by their huge abundance in urine - up to 30 mg/ml [166] - indicating a substantial and irreversible investment in protein synthesis, which occurs in the liver [165]. While MUPs have long been considered a male-specific trait, Černá *et al.* recently reported cycle-dependent low concentrations of MUPs in vaginal discharge [170]. The MUP gene cluster is relatively small, with 21 loci in the mouse genome [171], [172]. MUPs are members of the lipocalin family and, thus, exhibit the classical lipocalin β -barrel structure. The internal ligand-binding pocket renders them perfectly suitable as small molecule carriers. Therefore, MUPs were suggested to serve as carriers for otherwise short-lived volatile pheromones in urine [173]. Moreover, MUPs themselves serve as pheromones and carry intrinsic information. For one, a self-identifying MUP code was discovered in male mice since each individual expresses a discrete subset of 4-12 MUPs [174]. This unique signature remains unchanged throughout lifetime and serves as a combinatorial code to discriminate between "self" and others [137].

1 Introduction

Interestingly, sex-specific behavioral output is elicited by MUP20 (also termed "darcin" [175]), the best-studied member of the MUP family. Darcin acts as a single stimulus and does not require a combinatorial blend of other MUPs. In males, darcin promotes territorial aggression in a "hard-wired" (i.e., experience-independent), but context-dependent fashion [137], [176]. Darcin is, however, highly sexually attractive for females, in which it induces conditioned place preference after a single exposure [155], [175]. The attribution of memory formation to the AOS has been a novel and important discovery. On that note, Hoffman *et al.* suggest darcin-induced hippocampal neurogenesis and cell proliferation in the subventricular zone in a recent publication [177]. Since darcin effects depend on the recipient's sex, the darcin-activated sensory pathway is ideal for studying sex-specific differences in the AOS.

Another class of potent VNO activators are exocrine gland– secreting peptides (ESPs). The ESP gene cluster consists of 38 loci and codes for low molecular weight peptides that are secreted into mouse saliva and tear fluid [159]. Unraveled by Haga *et al.*, the ESP1-dependent sensory pathway is initiated by activation of the vomeronasal receptor V2Rp5, continues with the first, second, and third layer of central processing within the AOS, and eventually induces a stereotyped response in the female recipient: Lordosis [178], [179].

ESP22 is expressed in an age-dependent manner with maximum expression in juvenile mice of postnatal week one. By acting on its dedicated receptor V2Rp4, ESP22 incorporates limbic circuitry to suppress sexual displays from adult males [160], [180].

Work on ESP1 and ESP22, respectively, suggests a labeled-line coding strategy in the AOS. Future endeavors will have to reveal additional sensory pathways for a given stimulus before we can start to understand how pheromones act in a complex blend.

Vomeronasal receptors and signal transduction

VSNs are dedicated to transform specific binding of an external chemical cue into electrical output (i.e., action potentials) that is relayed to and processed by the central nervous system. The exact underlying mechanisms are only partially understood, but several signal transduction pathways have been proposed over the years [181]–[184].

1 Introduction

The first step of vomeronasal signal transduction is the binding of a given pheromone to its vomeronasal receptor (VR) that is expressed in high densities in the dendritic microvillous membrane. Currently, known vomeronasal receptors belong to either of the three gene families: *Vmn1r*, *Vmn2r*, and *Fpr-rs*. These translate into the protein families of V1R receptors, V2R receptors, and Formyl peptide receptor-like proteins (FPR) [109], respectively, which share the characteristic seven-transmembrane topology of G-protein coupled receptors. The number of members in each of the three families of vomeronasal receptors varies considerably. V1R and V2R receptor families developed a phylogenetic diversity of more than 100 functional members each [185]–[187]. In contrast, there are only five identified vomeronasal FPR receptors [188], [189].

Each receptor family couples to trimeric G-proteins that include either the $G_{\alpha i2}$ - or the $G_{\alpha o}$ -subunit. Interestingly, the vomeronasal sensory epithelium displays a dichotomic distribution of G-protein α -subunits and the co-expressed VR: While $G_{\alpha i2}$ and V1R-expressing VSNs are preferentially located in the apical layer, $G_{\alpha o}$ / V2R-expressing VSNs are found in the basal region of the neuroepithelium. *Fpr-rs1* is co-expressed with $G_{\alpha o}$ in basal sensory neurons, the remaining vomeronasal *Fpr-rs* genes are all co-expressed with $G_{\alpha i2}$ in the apical layer. The VSN pool is thus characterized by distinct molecular profiles and corresponding topographic segregation within the sensory epithelium [109], [114], [188]–[192].

Vmn1r, *Vmn2r*, and *Fpr-rs* gene expression is VSN specific and occurs in a monoallelic fashion. Each VSN follows the "one neuron - one receptor" rule and can be identified by its expressed VR isoform [147], [148], [186], [188], [189], [193], [194].

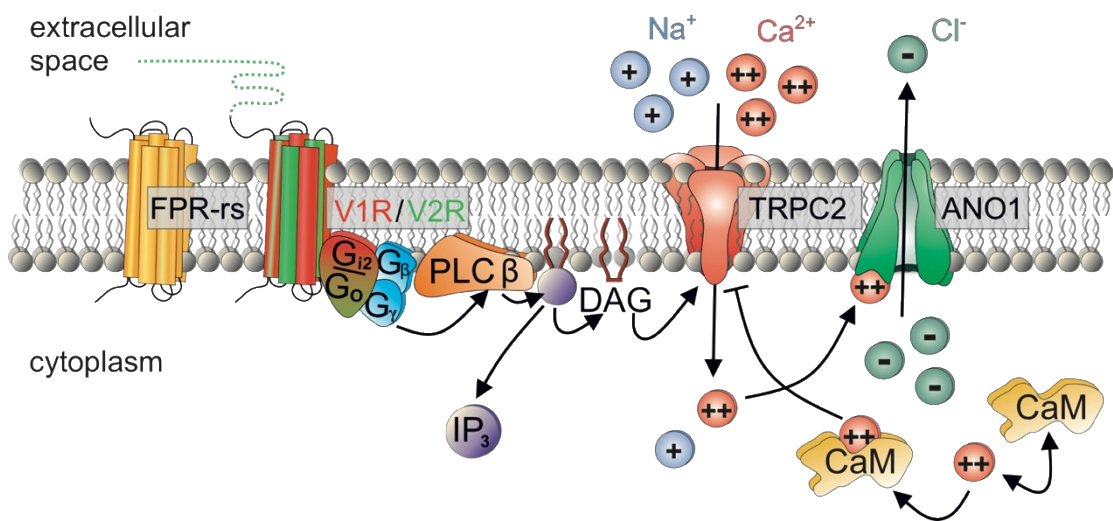


Figure 1.6: Primary signal transduction in VSNs. Activation of either of the three classes of vomeronasal receptors—formyl peptide receptor-like (FPR-rs) proteins, V1R, and V2R receptors—initiates G protein signaling and downstream PLC β activity that results in phosphoinositide turnover. The consequent elevation of both IP₃ and DAG lead to secondary events, including Ca²⁺ release of internal stores and activation of the cation channel TRPC2. TRPC2-mediated Ca²⁺ entry underlies initial depolarization and gating of a Ca²⁺-activated Cl⁻ channel ANO1, a subsequent depolarization boost. Negative feedback inhibition is exerted by Ca²⁺-bound calmodulin (CaM) and its inhibition of TRPC2. If TRPC2- and ANO1-dependent membrane depolarization reaches the VSN's threshold, action potential firing is set off (adapted from Mohrhardt et al., (2018) [138]).

Following VR activation, the associated G-Protein will disassemble and regulate downstream effectors. In VSNs, this is primarily β -isoforms of phospholipase C (PLC β) [182], [183], [195], [196] (Fig. 1.6). Activated PLC β hydrolyzes phosphatidylinositol-4,5-bisphosphate (PIP₂) into inositol-1,4,5-trisphosphate (IP₃) and diacylglycerol (DAG). Both metabolites, IP₃ and DAG, as well as polyunsaturated fatty acids (DAG metabolites, e.g., arachidonic acid) have been suggested to open the transient receptor potential cation channel, subfamily C, member 2 (TRPC2) in VSNs [181]–[183]. IP₃ additionally operates Ca²⁺ release from internal stores. The resulting accumulation of cytosolic Ca²⁺, either from TRPC2-dependent influx [183] and/or IP₃-mediated release from internal stores, activates the Ca²⁺-activated Cl⁻ channel anoctamine1 (ANO1/TMEM16A). ANO1-induced Cl⁻ efflux represents a response amplification [197]–[199].

1 Introduction

Given their remarkably high input resistance of several gigaohms, minimal transduction current (in the picoampere range) is sufficient to elicit VSN action potential discharge [200]–[202], which is then relayed to the AOB glomerular layer via the vomeronasal nerve. A calmodulin-operated negative feedback loop balances this sensitive current-voltage relationship. Ca^{2+} -bound CaM acts as a direct TRPC2 inhibitor, a mechanism that was suggested to mediate sensory VSN adaptation [203] (Fig. 1.6).

The accessory olfactory bulb - structure and circuitry

Axons from both apical and basal VSNs reach the AOB in a topologically segregated pattern. While basal sensory neurons terminate in the caudal AOB, apical VSNs target the rostral AOB. Here, they form sophisticated axonal branching and synapse onto AOB mitral cells (AMCs) – the AOB projection neurons. Similar to the MOB, VSN-to-AMC neuropil is structurally organized in glomeruli, albeit smaller in size (10-30 μm) and not as clearly defined (Fig. 1.7). Inhibitory periglomerular cells are scattered around each glomerulus and might shape VSN-to-AMC transmission [204]. Their concrete function in chemosensory processing is, however, completely unexplored. The AOB has long been deemed a “copy” of the MOB. Yet, AOB circuitry is wired fundamentally different, resulting in huge implications for the AOB coding logic. For a start, VSNs expressing the same receptor project to multiple glomeruli [147], [148], [205], [206]. This organization differs from the MOB labeled-line, where one glomerulus gets input from a single OSN population with the same OR. Secondly, AMCs are not organized in a distinct monolayer, as their MOB counterparts. AMCs exhibit a strikingly different morphology than MTCs. As described above, MOB projection neurons extend one apical dendrite to a single glomerulus [132]. AMCs, however, are smaller and possess several apical dendrites that reach 3-9 glomeruli in various locations of the glomerular layer (GL). The AMC dendritic arborization is enriched by 1-2 lateral dendrites that emanate from each AMC soma [207]–[209]. How is VR-identity, and therefore pheromone identity, encoded at the AOB level if a labeled-line is not clearly apparent? First hints are provided by Wagner *et al.*, who apply a multireceptor genetic approach for fluorescent tagging of V1R populations. Combined with intracellular dye injection into AMCs, they investigated mitral cell-glomerular

1 Introduction

connectivity and found that individual mitral cells extend dendrites to glomeruli associated with different, but closely related V1Rs. The authors suggest that AOB wiring serves information integration among several VRs with related pheromone information [206].

In the AOB, AMC axons bundle in the lateral olfactory tract (LOT), where they converge with MOB fibers and project into higher brain centers (Fig. 1.7). The LOT separates the mitral cell layer (MCL) from the neighboring granule cell layer (GCL), which harbors spiny, axon-less interneurons (internal granule cells, iGCs). A few GCs are also found within the MCL, called external granule cells (eGCs). GCs form recurrent dendrodendritic synapses with AMCs, that harness glutamate/GABA as neurotransmitters. Given that mitral-to-granule cell synaptic transmission is glutamatergic (excitatory), and granule-to-mitral cell transmission is GABAergic (inhibitory), AMC firing will result in self-inhibition and/or lateral inhibition of neighboring AMCs that connect to the same GC [207], [210]–[212]. Therefore, the dendrodendritic synapse likely plays an essential role in "sharpening" a pheromone representation [138].

Like MTCs, AMCs display periodic bursts of activity in an "idle" state. Other than their MOB analogs, AMCs oscillate independently of the breathing-rhythm in an infra-slow frequency spectrum (<0.1-1 Hz). This oscillatory resting state has been observed both *in vivo* and *in vitro* by several groups, including ours [213]–[215], testament to its physiological relevance.

1 Introduction

A subpopulation of AMCs intrinsically generates these oscillations independent of fast GABAergic and glutamatergic synaptic transmission [218], and oscillations are synchronized within several microcircuits across the AOB [214]. Whether such oscillations are transmitted via mitral-to-mitral cell lateral dendrites and whether they play a role in chemosensory processing is still a matter of ongoing research.

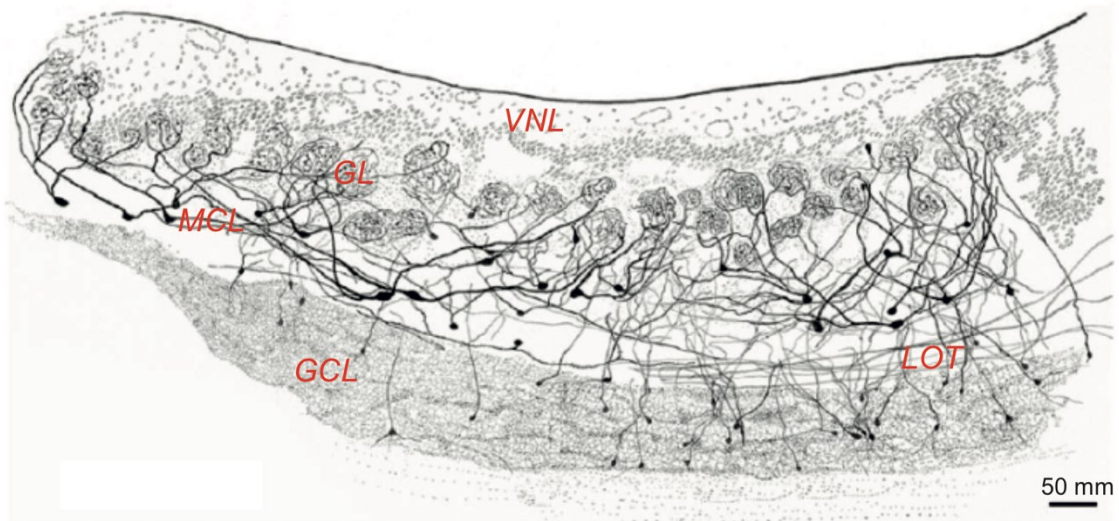


Figure 1.7: Cytological heterogeneity and anatomical organization of the rat accessory olfactory bulb. Drawing of the sagittal AOB from a Golgi-Cox specimen counterstained with Nissl shows the vomeronasal nerve layer (VNL) with incoming vomeronasal sensory neuron axons, the glomerular layer (GL), the mitral cell layer (MCL) containing the AOB projection neurons, the granule cell layer (GCL) with axon-less interneurons, and the lateral olfactory tract (LOT) that directs MOB and AOB projections to higher brain centers (from: Larriva-Sahd (2008)[207]).

Downstream processing

Compared to other sensory systems, AOS circuitry is rather unusual and intriguingly simple - an aspect that makes it an ideal model to study chemosensory coding. After AOB filtering and processing, vomeronasal information is directly passed onto limbic nuclei, including the medial amygdala and posteromedial cortical nucleus (together forming the “vomeronasal amygdala”), as well as the bed nucleus of the stria terminalis (BNST) and the nucleus of the accessory olfactory tract [121], [216]–[218]. Previously segregated information from the rostral and caudal region of the AOB, is integrated within the limbic system [142]. Yet, only the anterior AOB projects to the bed nucleus of the stria terminalis and only the posterior

1 Introduction

AOB projects to the dorsal anterior amygdala. These partially segregated pathways target discrete regions within the hypothalamus [219].

From the vomeronasal amygdala, information is relayed to the ventromedial and medial preoptic area, the ventromedial hypothalamus, and the premammillary and supraoptic nuclei in the hypothalamus [220], [221]. Olfactory inputs to the hypothalamus are eventually involved in endocrine regulation of reproduction, puberty, parental behavior, and other social interactions [222]–[224]. The AOS is therefore a powerful system with merely three synapses that link sensory input to behavioral output. Given the "hard-wired" nature of the limbic system and the absence of prominent cortical connections in the AOS [141], this system is considered a mediator for innate, genetically pre-determined responses. However, a significant body of evidence suggests that the AOS functions rather dynamic and involves learning and state-dependency [155], [225], [226]. This is achieved by rich top-down modulation from the corticomedial amygdala, the bed nucleus of the stria terminalis, the locus coeruleus, the horizontal limb of the diagonal band of Broca, and the raphe nuclei [227]–[230]. These feedback loops enter the AOB via the LOT or through the bulbar core white matter [207]. The precise nature of the bottom-up and top-down interplay in the AOS is an intricate subject and its revelation a long-term goal for ongoing research.

1.3 Aims

Infertility constitutes a global problem and affects an estimated 15 % of couples worldwide. This amounts to 48.5 million couples, 97 million individuals. Males are solely responsible for 20 - 30 % of infertility cases and contribute to 50 % of cases overall [231], [232]. Today, up to 58 % of male infertility cases are of unknown origin and considered idiopathic [233], [234]. Furthermore, the available options for male contraception are still, euphemistically speaking, limited. This massive gap in our understanding of male (in)fertility is partially attributed to insufficient knowledge of both spermatogenesis (i.e., sperm production) and mature sperm physiology. Thus, this body of work will address the reproductive "black box" by pursuing two research projects:

1 Introduction

Project A: ATP activation of peritubular cells drives testicular sperm transport

In the seminiferous tubules of the testes, spermatozoa are generated continuously through a complex multi-step process (spermatogenesis). The basic physiological principles, however, that control both maturation and luminal transport of the still immotile spermatozoa within the seminiferous tubules are largely unknown. The aim of this subproject is to elucidate mechanisms of luminal sperm transport and investigate a potential involvement of extracellular ATP as an activation mechanism of testicular smooth muscle cells (TPCs). I will investigate, whether extracellular ATP triggers TPC contractions and whether ATP is sufficient to activate luminal transport of spermatozoa. If so, I will examine whether sperm transport is executed in a preferred direction along the longitudinal axis of the tubulus. Screening for purinoceptor transcripts will inform about the TPC expression profile and P2X receptor functionality will be determined via electrophysiological recordings of TPCs upon ATP-stimulation.

Project B: Electrophysiological identification of DSper

Sperm transition to hyperactivated motility is a crucial requirement for fertilization. Hyperactivation provides the propulsion force required to navigate through viscous luminal fluids of the female reproductive tract and penetrate the protective vestments of the egg. The CatSper channel is a key player in the transition to hyperactivated motility [76], [79], [235]–[240]. However, proper CatSper function requires three concurrent activation mechanisms: (1) membrane depolarization, (2) intracellular alkalization, and, for primate CatSper specifically, (3) abundance of P4 [49], [86], [89], [241], [242]. While the two latter mechanisms have been described in detail, the source of membrane depolarization remains puzzling. One goal of my work is, therefore, to record and characterize DSper, the "depolarizing ion channel of human sperm", and eventually resolve its molecular identity in human spermatozoa.

1 Introduction

The sense of smell is a vital tool for many species to perceive and adapt to the outside world. Given the overwhelming complexity of olfactory stimuli, several olfactory subsystems have evolved. While we have a relatively clear understanding of primary olfactory processing in the main olfactory system, the accessory olfactory system that is involved in social information processing, remains relatively unexplored. The overall aim of this work is, therefore, to gain a more profound understanding of chemosensory signaling mechanisms in the accessory olfactory system:

Project C: Establishing an optogenetic stimulation paradigm in the murine olfactory bulb

The organization of the AOB sensory map differs dramatically from the main olfactory system. Differences in VSN targeting have important implications for the AOS olfactory coding logic, which is not understood. One aim of this thesis is therefore to establish an *in vitro* presynaptic stimulation paradigm that mimics sensory input to AMCs. I will utilize the OMP-ChR2-YFP mouse line in which channelrhodopsin is knocked into the *Omp* locus and, thereby, renders all mature VSNs and OSNs light-activatable. Spatiotemporally defined laser exposure will then elicit a user-defined glomerular activation pattern and the impact on connected AMCs can be studied by electrophysiology. I will establish this toolkit in a comparative study including the AOB and the MOB.

Project D: Decoding of receptor-ligand interactions in the VNO

One of the major hurdles for a complete understanding of olfactory information processing is our limited knowledge about cognate ligand-receptor pairs, particularly in the AOS. Since receptor activation is the first step in chemosensory processing, this missing information creates a major bottleneck in AOS research. However, attempts to express recombinant V1R and V2R receptor proteins in heterologous systems for high-throughput ligand screening have largely failed. This work aims to describe the darcin receptor. Darcin is active as a single compound and induces a sexually dimorphic response in recipient mice. Unraveling the molecular identity of the darcin receptor will, thus, provide the knowledge to trace the darcin-

1 Introduction

dependent sensory pathway from sensory input to behavioral output. For this purpose, I will apply a multidisciplinary approach that combines *in silico* modeling of ligand-receptor interactions, AAV-driven ectopic expression of VRs, and Ca^{2+} imaging in acute VNO slices.

2 Materials and methods

2.1 Reagents

1, 5-bis{[2-(di-methylamino)ethyl]amino}-4, 8-dihydroxyanthracene-9, 10-dione (DRAQ5™)	Thermo Fisher Scientific
1,2-bis(<i>o</i> -aminophenoxy)ethane- <i>N,N,N',N'</i> -tetraacetic acid (BAPTA)	Sigma Aldrich
1,4-Dithiothreitol (DTT)	Diagonal
2-(<i>N</i> -Morpholino)ethanesulfonic acid hydrate (MES)	Sigma Aldrich
2-[Bis(2-hydroxyethyl)amino]ethanesulfonic acid (BES)	VWR
4-(2-Hydroxyethyl)-1-Piperazine-1-Ethanesulfonic Acid, N-(2-Hydroxyethyl)-Piperazine-N'-2-Ethanesulfonic Acid (HEPES)	Diagonal
4',6-Diamidin-2-phenylindol dihydrochloride (DAPI)	Thermo Fisher Scientific
acetic acid	VWR
adenosine 5'-triphosphate disodium salt (NaATP)	Sigma Aldrich
adenosine 5'-triphosphate magnesium salt (MgATP)	Sigma Aldrich
agarose, low-melt	BioRad
Amersham™ Protran® nitrocellulose membrane	GE Healthcare
Amicon Ultra-4 Centrifugal Filter Unit, 10 K MWCO	Merck Millipore
ATTO 633	ATTO-Tec
bovine serum albumine	Sigma Aldrich
bromophenol blue sodium salt	AppliChem
Cal-520(TM) AM	Biomol
calcium chloride (CaCl ₂)	Sigma Aldrich
capsaicin	Cayman
carvacrol	Sigma Aldrich
cesium chloride (CsCl)	Sigma Aldrich
cesium hydroxide (CsOH)	Sigma Aldrich

2 Materials and methods

cesium methansulfonate (CsMeSO ₃)	Sigma Aldrich
chloroform	VWR
cOmplete™ mini EDTA-free protease inhibitor cocktail	Roche
Coomassie® brilliant blue	Sigma Aldrich
D-glucose	Sigma Aldrich
Dimethyl sulfoxide (DMSO)	Thermo Fisher Scientific
ECL SuperSignal West Pico kit	Pierce
ethylene glycol-bis(β-aminoethyl ether)-N,N,N',N'-tetraacetic acid (EGTA)	Sigma Aldrich
ethylenediaminetetraacetic acid (EDTA)	Sigma Aldrich
Fast Green	Sigma Aldrich
fetal bovine serum	Thermo Fisher Scientific
Fluo-4/AM	Invitrogen
glycerin	Diagonal
glycine	AppliChem
guanosine 5'-triphosphate sodium salt hydrate (NaGTP)	Sigma Aldrich
HC067047	Tocris
HisPur™ Ni-NTA Spin Column, 1 ml	Thermo Fisher Scientific
ISolate	Irvine Scientific
imidazole	Sigma Aldrich
isopropyl alcohol	Thermo Fisher Scientific
ivermectin	Sigma Aldrich
kanamycin	Diagonal
L-menthol	Cayman
lipofectamine	Invitrogen
Luria Broth Agar (LB plates)	Thermo Fisher Scientific
Luria Broth Base™ (LB medium)	Thermo Fisher Scientific
magnesium chloride (MgCl ₂)	Sigma Aldrich

2 Materials and methods

magnesium sulfate (MgSO_4)	Sigma Aldrich & AppliChem
methanol	VWR
NNC 55–0396	R and D systems
phenamil (methansulfonate)	Cayman
Phosphate buffered saline (PBS)	Sigma Aldrich
Phosphatidylinositol 4,5-bisphosphate (PIP_2)	Echelon Bioscience
Pluronic F-127	Thermo Fisher Scientific
potassium chloride (KCl)	Sigma Aldrich
potassium dihydrogenphosphate (KH_2PO_4)	Sigma Aldrich
potassium hydroxide (KOH)	Supelco
pregnenolone sulfate	Sigma Aldrich
RN1734	Tocris
RN1747	Tocris
S.O.C. medium	Thermo Fisher Scientific
skim milk powder	AppliChem
sodium azide	Sigma Aldrich
sodium chloride (NaCl)	Sigma Aldrich
sodium dodecyl sulfate (SDS)	Sigma Aldrich
sodium hydroxide (NaOH)	Supelco
sodium lactate (60% w/w)	Sigma Aldrich
sodium methansulfonate (NaMeSO_3)	Sigma Aldrich
sodium pyruvate	Sigma Aldrich
streptavidin, Alexa Fluor TM 488 conjugate	Invitrogen
suramin sodium salt	Sigma Aldrich
Terrific Broth Overnight Express TM Medium (TB medium)	Sigma Aldrich
Tris(hydroxymethyl)aminomethane (TRIS)	VWR
Triton X-100	Sigma Aldrich
Trizol	Thermo Fisher Scientific

2 Materials and methods

Tween 20

AppliChem

2.2 Solutions and buffers

All solutions were prepared with distilled water of the highest purity grade, filtered for sterility, and stored at 4 °C for up to one month or at -20 °C (long-term).

S1: Extracellular solution for TPC physiology (in mM):

145 NaCl, 5 KCl, 1 CaCl₂, 0.5 MgCl₂, 10 HEPES

pH: 7.3 adjusted with NaOH

Osmolarity: 300 mOsm adjusted with glucose

S2: Intracellular solution for TPC patch-clamp (in mM):

143 KCl, 2 KOH, 1 EGTA, 0.3 CaCl₂, 10 HEPES, 0.5 NaGTP

pH: 7.1 adjusted with KOH

Osmolarity: 290 mOsm adjusted with glucose

[Ca²⁺]_{free} = 110 nM

S3: Sperm high saline extracellular solution (in mM):

135 NaCl, 5 KCl, 2 CaCl₂, 1 MgSO₄, 20 HEPES, 5 glucose, 10 sodium lactate, 1 sodium pyruvate

pH: 7.4 adjusted with NaOH

Osmolarity: 320 mOsm adjusted with sucrose

S4: Artificial human tubal fluid solution (in mM):

98 NaCl, 5 KCl, 0.4 KH₂PO₄, 2 CaCl₂, 0.2 MgSO₄, 20 HEPES, 3 glucose, 20 sodium lactate, 0.4 sodium pyruvate

pH: 7.4 adjusted with NaOH

2 Materials and methods

Osmolarity: 280 mOsm adjusted with sucrose

S5: Divalent-free extracellular solution, cesium-based (in mM):

140 CsMeSO₃, 1 EDTA, 20 HEPES

pH: 7.4 adjusted with CsOH

Osmolarity: 320 mOsm adjusted with sucrose

S6: Extracellular solution for isolated DSper currents, cesium-based (in mM):

140 CsMeSO₃, 1 MgCl₂, 20 HEPES

pH: 7.4 adjusted with CsOH

Osmolarity: 320 mOsm adjusted with sucrose

S7: Extracellular solution for isolated DSper currents, sodium-based (in mM):

140 NaMeSO₃, 1 MgCl₂, 20 HEPES

pH: 7.4 adjusted with NaOH

Osmolarity: 320 mOsm adjusted with sucrose

S8: Intracellular solution for sperm patch-clamp, cesium-based (in mM):

140 CsMeSO₃, 10 BAPTA, 4 NaATP, 1 CsCl, 20 HEPES

pH: 7.4 adjusted with CsOH

Osmolarity: 330 mOsm adjusted with sucrose

S9: Oxygenated (95% O₂/5% CO₂) artificial CSF for AOB slice physiology (in mM):

124 NaCl, 26 NaHCO₃, 3 KCl, 1.25 NaH₂PO₄, 1.3 MgSO₄, 1.3 CaCl₂, 10 glucose

pH: 7.4 with carbogen saturation

Osmolarity: 300 mOsm adjusted with glucose

S10: Sucrose-based oxygenated (95% O₂ / 5% CO₂) aCSF for AOB slice preparation (in mM):

220 sucrose, 26 NaHCO₃, 3 KCl, 1.25 NaH₂PO₄, 2.6 MgSO₄, 10 glucose

2 Materials and methods

pH: 7.4 with carbogen saturation

Osmolarity: 300 mOsm adjusted with glucose

S11: Intracellular solution for AOB mitral cell electrophysiology (in mM):

125 K-gluconate, 10.5 KCl, 10 HEPES, 1 EGTA, 0.39 CaCl₂, 2 MgCl₂, 2 MgATP, 0.5 NaGTP, fluorophore (20 µM Alexa Fluor 488 hydrazide or 20 µM ATTO 633), 0.3 % biocytin (optional)

pH: 7.1 adjusted with KOH

Osmolarity: 290 adjusted with glucose

[Ca²⁺]_{free} = 200 nM

S12: Extracellular Solution for VNO slice physiology (in mM):

145 NaCl, 5 KCl, 1 CaCl₂, 1 MgCl₂, 10 HEPES

pH: 7.3 adjusted with NaOH

Osmolarity: 300 adjusted with glucose

S13: Oxygenated (95% O₂ / 5% CO₂) extracellular solution for VNO slice physiology (in mM):

120 NaCl, 25 NaHCO₃, 5 KCl, 1 CaCl₂, 1 MgSO₄, 5 BES

pH: 7.3 with carbogen saturation

Osmolarity: 300 adjusted with glucose

S14: High potassium extracellular solution for VNO physiology (in mM):

100 NaCl, 50 KCl, 1 CaCl₂, 1 MgSO₄, 10 HEPES

pH: 7.3 adjusted with NaOH

Osmolarity: 300 adjusted with glucose

*S15: Lysis buffer for *E. coli* lysis:*

50 µl Triton X-100, 1 cOmplete™ Protease Inhibitor Tab (EDTA-free) in 50 ml PBS^{-/-}

S16: Laemmli sample buffer:

2 Materials and methods

100 mM TRIS, 20 % glycerine, 4% SDS, 0.2% bromophenol blue sodium salt,

200 mM DTT in H₂O

2.3 Antibodies

Host species	Antigen	Conjugation	Clonality	Applied concentration	Supplier, ID
rabbit	α-TRPV4		polyclonal	1:100 for ICC 1:2000 for WB	Abcam, ab39260
mouse	α-actin, α-smooth muscle	FITC	monoclonal	1:500	Sigma Aldrich, #F3777
mouse	α-6xHis tag [®]		monoclonal	1:5000	Abcam, ab18184
goat	α-MUP20		polyclonal	1:1000	MyBioSource, #MBS448104
mouse	α-rabbit	DyLight488	monoclonal	1:2000	Jackson, #211-482-171
goat	α-mouse	peroxidase	polyclonal	1:4000	Sigma Aldrich, #AB-19.0077
rabbit	α-goat	peroxidase	polyclonal	1:50000	Sigma Aldrich, #A8919

2.4 Primers

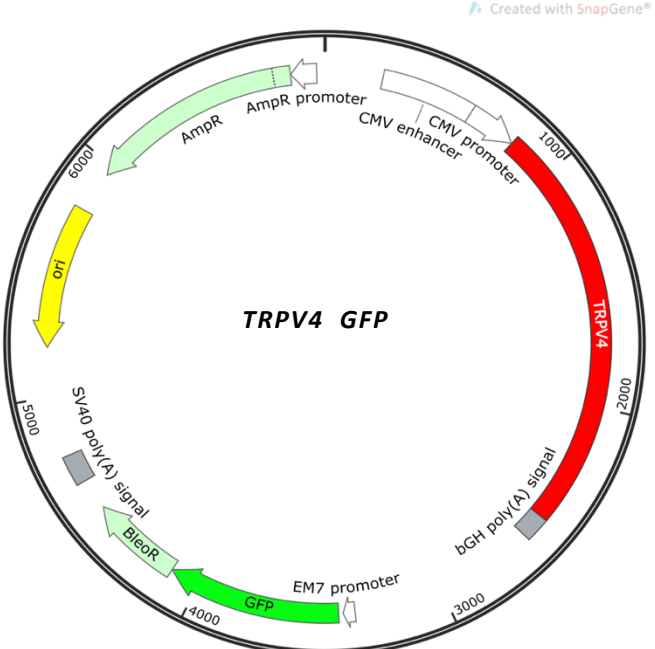
Target gene	Forward primer 5'-3'	Reverse primer 5'-3'
TRPV4	ACAGATATCACCATGGCGGATT CCAGCG	AACACAGCGGCCCTAGAGCGGGGC GTCATC
P2RX1	CCGAAGCCTTGCTGAGAA	GGTTGCAGTGCCGTACAT
P2RX2	GACCTCCATGGGGTGGGCT	TGGGGTCCGTGGATGTGGAGT
P2RX3	CTGCCTAACCTCACCGACAAG	AATACCCAGAACGCCACCC

2 Materials and methods

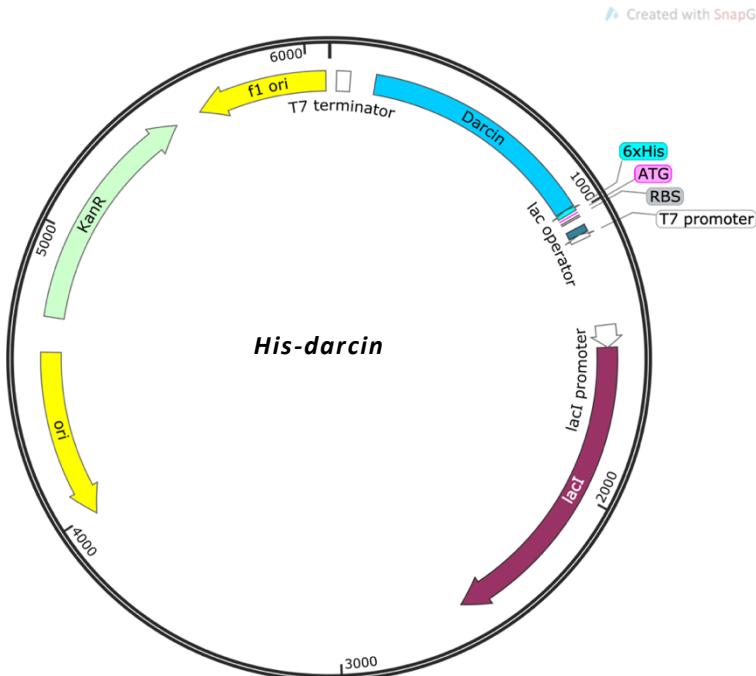
P2RX4	CCCTTGCCCTGCCAGATAT	CCGTACGCCTGGTGAGTGT
P2RX5	GCTGCCTCCCCTGCAACCC	AAGCCCCAGCACCCATGAGC
P2RX6	CCCAGAGCATCCTCTGTTCC	GGCACCAAGCTCCAGATCTCA
P2RX7	GTCTCGCCTACCGGAGCAACG	ATGTCCTGGGAGCCGAAGCG
P2RY1	CGACAGGGTTATGCCACTT	TCGTGTCTCCATTCTGCTTG
P2RY2	CGTGCTCTACTCGTCACCA	GACCTCCTGTGGTCCCATAA
P2RY4	ACTGGCTTCTGCAAGTTCGT	AGGCAGCCAGCTACTACCAA
P2RY6	CATTAGCTTCCAGCGCTACC	GCTCAGGTCGTAGCACACAG
P2RY12	CATTGCTGTACACCGTCCTG	AACTTGGCACACCAAGGTT
GAPDH	CAAGGTCATCCATGACAACTTG	GTCCACCAACCTGTTGCTGTAG

2.5 Plasmids

Figure 2.1: TRPV4 - GFP Plasmid for heterologous expression in HEK293 cells. Transfected cells express two separate transcripts, which are 1) Green Fluorescent Protein (GFP) under EM7 promoter control and 2) TRPV4 cloned from human sperm cDNA under CMV promoter control for high-level constitutive expression in eukaryotic cells. Ampicillin resistance gene is encoded for selectivity in E.coli. (Plasmid kindly provided by Prof. Polina Lishko, UC Berkeley)



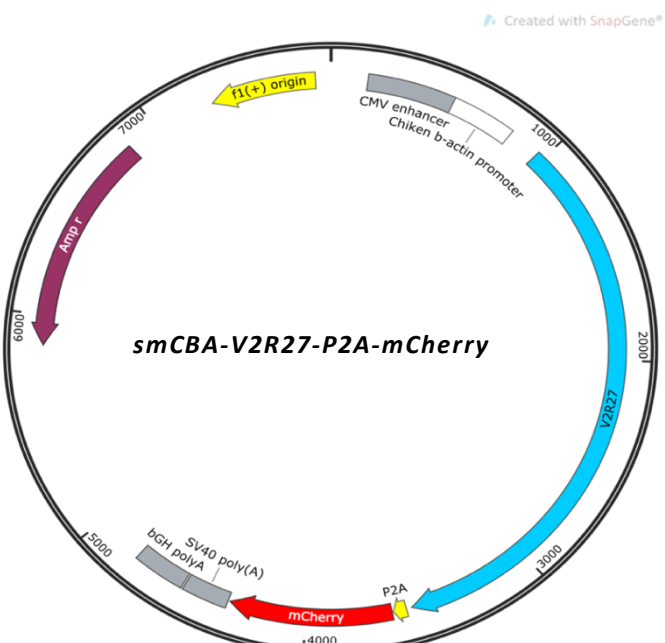
2 Materials and methods



Beynon, University of Liverpool)

Figure 2.2: Plasmid for recombinant darcin ex-expression in *E.coli*: T7 RNA polymerase operated trans-cription of darcin is regulated within the Lac operon. The Lac repressor is encoded by the lacI gene and binds to the Lac operator to suppress darcin transcription. In the presence of intracellular allolactose or IPTG, the transcription block is released. The darcin sequence includes an N-terminal His-tag for protein detection and purification. A Kanamycin resistance gene facilitates selection in *E.coli*. (RBS = ribosomal binding site, ATG = start codon, Plasmid kindly provided by Em. Prof. Rob

Figure 2.3: AAV8 smCBA-V2R27-P2A-mCherry construct for ectopic V2R27 expression and fluorescent tagging with mCherry. AAV8-mediated delivery of the shown plasmid initiates bicistronic transcription of the vomeronasal receptor V2R27 and mCherry. The transcript is under the chicken β -actin promoter. Both protein sequences are separated by a P2A site, inducing ribosomal skipping and, thus, the translation into two separate peptides. An ampicillin resistance gene facilitates selection in *E.coli*. The negative control plasmid contains no V2R27 insert. (AAV carrying this plasmid kindly provided by Prof. Jeremy McIntyre, University of Florida).



2.6 Equipment

8-in-1 multi-barrel perfusion pencil	AutoMate Scientific
Amplifier EPC-10 USB double	HEKA Electronic
Axon™ Digidata 1550A	Molecular Devices
AXOPATCH 200B amplifier	Molecular Devices
BioPhotometer	Eppendorf
Borosilicate glass capillary (1.5 mm OD / 0.86 mm ID)	Science Products
Borosilicate glass capillary (1.5 mm OD / 0.86 mm ID)	Sutter instruments
Cameras:	Leica Microsystems: cooled CCD-camera DFC365FX DFC450C camera DFC365FX camera Hamamatsu: ORCA-ER CCD camera Photometrics: PrimeBSI sCMOS
Centrifuge mini spin	Eppendorf AG
Criterion Gel Electrophoresis cell	Bio-Rad
Cryostat CM 1950	Leica Microsystems
Diode laser 473 nm	Rapp Opto Electronic
glass imaging chambers	World Precision Instruments
Hot plate magnetic stirrer	Snijders
Microforge MF-830	Narishige
Micromanipulator Luigs-Neumann Device	Luigs & Neumann
Micropipette puller P1000	Sutter Instruments
Micropipette puller PC-10 vertical two-step puller	Narishige

2 Materials and methods

Microscopes:	Leica DM6000 FS Leica Multiphoton SP8 Leica TCS SP4 Leica DMI 4000B, inverse Leica MacroFluo Z16 APO A Olympus IX71, inverse
MPC 385 micromanipulator	Sutter Instruments
Noise eliminator 50/60 Hz (HumBug)	Quest Scientific
Objectives:	Leica 20x (HCX APO L U-V-I 20x/0.50) Leica 63x (HCX APO L U-V-I 63x/0.90) Leica 25x (HC IRAPO L 25x/1.00 W) Leica 20x (HCX APO L20x/1.00 W) Leica 1x (PLANAPO 1.0x / WD 97) Leica 5x (PLANAPO 5.0x /0.50 LWD) Olympus 60x UplanSApo
Oscilloscope TDS 1001B	Tektronik
Perfusion system 8-in-1	AutoMate Scientific
pH electrode InLab routine	Mettler Toledo
pH Meter five easy	Mettler Toledo
PowerPac Universal power supply	Bio-Rad
Prior Lumen 200 Fluorescence Illumination System	Prior Scientific
ProScanTMIII control unit	Prior Scientific
Slice mini chamber	Luigs & Neumann
Spectra X light engine	Lumencore
Stimulation isolation unit SIU-202	Warner Instrument Corporation
Temperature control device TC-324B	Warner Instrument Corporation
Trans-Blot Turbo system (semi-dry)	Bio-Rad

2 Materials and methods

Trigger interface TIB-14 S	HEKA Elektronik
UGA-42 Firefly	Rapp Opto Electronic
UGA-42 Geo	Rapp Opto Electronic
Vibration-damping air table (IsoStation)	Newport Inc.
Vibratome VT 1000 S	Leica Microsystems

2.7 Software

Clampex 10.5	Molecular Devices
Clampfit 10.3	Molecular Devices
CorelDRAW 2019	Corel Corporation
Igor Pro 8	WaveMetrics Inc.
ImageJ 1.51n	NIH Image
JPCalcW	Barry, 1994
Leica LAS X	Leica Microsystems
MetaMorph	Molecular Devices
Office 2019	Microsoft
OriginPro 8.6	OriginLab Corporation
Patchmaster	HEKA Electronik
Photoshop CS5	Adobe Corporation
Python	Python Software Foundation
Spyder	SpyderIDE
SysCon	Rapp Opto Electronic GmbH

2.8 Mouse strains

All animal procedures were approved by local authorities and in compliance with both European Union legislation (Directive 2010/63/EU) and recommendations by the Federation of European Laboratory Animal Science Associations (FELASA). When possible, mice were housed in littermate groups of both sexes (room temperature (RT); 12:12 h light-dark cycle;

2 Materials and methods

food and water available *ad libitum*). If not stated otherwise, experiments used adult (>12 weeks) mice. Mice were killed by CO₂ asphyxiation and decapitation using sharp surgical scissors. We used C57BL/6J mice (Charles River Laboratories, Sulzfeld, Germany) as well as offspring from crossing SMMHC-CreERT2 (JAX #019079) mice with either Ai95D (JAX #028865) or Ai14D (JAX #007914) mice, respectively. For optogenetic stimulation of OSN and VSN axon terminals in the olfactory bulb, heterozygous OMP-ChR2-YFP mice (JAX #014173) were used.

2.9 Cell lines

HEK293 (ATCC #CRL-1573) cells were transfected during passages 2 to 15 using a standard lipofectamine protocol (Invitrogen). Transfected cells were identified as green fluorescent, and successful transfection was verified via western blotting and electrophysiology. The cell line was not tested for mycoplasma and is not on the list of commonly misidentified cell lines maintained by the International Cell Line Authentication Committee:

http://iclac.org/wp-content/uploads/Cross-Contaminations-v8_0.pdf

Murine testicular peritubular cells (mTPCs) were isolated from adult C57BL/6J mice and cultured as described in [15]. Patch-clamp experiments on TPCs were performed during passages 1 or 2. Primary cultures retained high purity for ≥14 days in vitro [15].

2.10 Human sperm donation and sperm processing

A total of 5 healthy male volunteers were recruited for this study, which was conducted with the Committee on Human Research's approval at the University of California, Berkeley (protocol 10-01747, IRB reliance #151). Informed consent was obtained from all participants. Ejaculates were obtained by masturbation, and samples liquefied for 60 minutes at 22 °C. Spermatozoa were purified following the swim-up protocol as previously described [243]. Briefly, 1 ml of liquefied ejaculate was carefully pipetted at the bottom of a 50 ml falcon tube containing 7 ml of preheated (37 °C) solution S4. Swim-up was performed for 1 hour at 37 °C. For patch-clamp experiments, the top 1 ml section of the supernatant was collected. For Ca²⁺

2 Materials and methods

imaging experiments, the supernatant's top 2 ml was used. Ejaculated purified spermatozoa were generally viable for up to 12 hours after isolation. *In vitro* capacitation was accomplished by 4 h incubation in 20% fetal bovine serum, 25 mM NaHCO₃ in S4 buffer at 37 °C and 5% CO₂. Electrophysiological properties of non-capacitated and capacitated spermatozoa from the same donor were routinely compared on the same day.

2.11 Preparation of acute AOB and MOB slices

Adult mice were euthanized by brief exposure to CO₂ preceding decapitation. First, the lower jaw, fur, and eyeballs were quickly removed. All further steps were then carried out with the cranium/tissue submerged in ice-cold oxygenated S10. Following a bilateral craniotomy, the left and right olfactory bulbs were rapidly dissected (Fig. 2.4) and embedded in 4% low-gelling agarose (in S1, 42 °C). Parasagittal 250 µm slices were cut in ice-cold oxygenated S10 with a Leica VT1000S vibratome (speed: 3.5 a.u. = 0.15 mm/s; frequency: 5.5 a.u. = 55 Hz; amplitude = 0.6 mm; Leica Biosystems, Nussloch, Germany). Acute slices containing the AOB and MOB were transferred to a storage chamber for ≥1 h recovery in oxygenated S9 at RT.

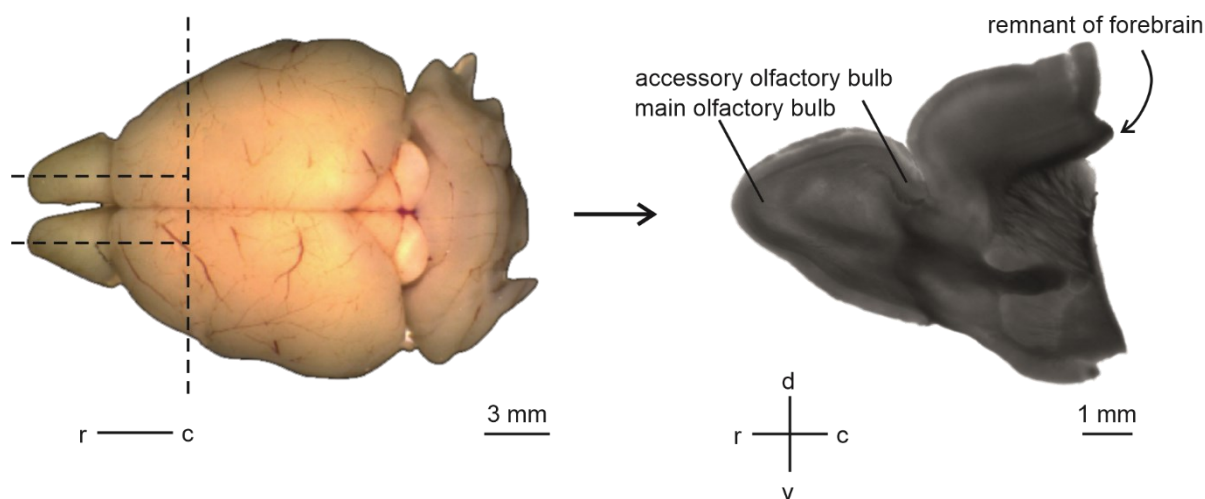


Figure 2.4: Preparation of parasagittal acute AOB and MOB slices. **Left:** First, the dissected mouse brain is cut coronally (vertical dashed line). Next, both hemispheres are separated and sliced parasagittally (horizontal dashed lines) to access the AOB. **Right:** Sagittal view of a 250 µm mouse olfactory bulb / forebrain slice.

2 Materials and methods

2.12 Preparation of acute VNO vibratome slices

Mice were euthanized by brief exposure to CO₂ followed by decapitation. All steps were performed in ice-cold solution S12 and/or on a cooling-pad. The lower jaw and the soft palate were removed, allowing access to the VNO. The two VNO halves were separated and dissociated from the cartilage capsule. The dissected VNO was then embedded in 5% low-gelling temperature agarose (in S12, 42 °C) and 150 µm coronal slices were cut in ice-cold oxygenated S13 with a Leica VT1000S vibratome (speed: 3.5 a.u. = 0.15 mm/s; frequency: 7.0 a.u. = 75 Hz; amplitude: 0.6 mm; Leica Biosystems, Nussloch, Germany). The acute slices were transferred to a storage chamber with circulating ice-cold, oxygenated S13 until use.

2.13 Electrophysiology

2.13.1 The patch-clamp technique

Due to their widespread role in cellular signaling mechanisms, ion channel physiology has always been a major topic of interest. As a refinement of early voltage-clamp experiments in giant squid axons (Hodgkin & Huxley, 1952, [244]), Erwin Neher and Bert Sackmann invented the “patch-clamp technique” in the late 1970s [245], which gave electrophysiologists new prospects and the two inventors the Nobel Prize in Physiology or Medicine (Nobelprize.org, 2014). The principle is based on establishing a tight seal between a biological membrane and a recording electrode. Due to the high seal-resistance (GΩ), ionic currents across the membrane and the resulting membrane potential can be recorded. Even single-channel opening events can be resolved with this technique.

A fire-polished patch pipette filled with an electrolyte solution is tightly sealed onto the cell membrane. This results in the electrical isolation of a small membrane patch. Ion flux across this patch will flow into the pipette tip and be recorded by an electrode connected to a highly sensitive differential amplifier. Continuous comparison with a reference electrode placed in the extracellular environment enables electrophysiological recordings in two distinct configurations: In the “voltage-clamp” configuration, a current is injected into the cell via a negative feedback loop to compensate deviation in membrane potential from a

2 Materials and methods

predetermined potential (V_{hold}). Recording this current allows conclusions about the membrane conductance. In the "current-clamp" mode, the injected current is controlled and membrane potential changes are recorded. This configuration enables the cell to behave in its physiological way electrically.

To achieve the described high-resistance connection between the patch pipette and the cell surface, positive pressure is applied to the pipette before it is dipped into extracellular solution. This prevents the pipette tip from clogging. Under optical control, the pipette is advanced to the target cell. Once the tip is positioned in close proximity to the cell membrane, a slight increase in pipette resistance occurs. The positive pressure is then rapidly withdrawn and reversed to gentle negative pressure. Invagination of the membrane into the tip leads to a steep increase in pipette resistance and eventually the establishment of a tight, high resistance ($G\Omega$) seal, the "gigaseal". In this "cell-attached" configuration, recordings from single or few channels situated in the isolated membrane patch can be performed with any intracellular mechanisms that could possibly influence a channel's function remaining unperturbed. To study the entire population of ion channels in the target cell, the "whole-cell" configuration is established. The membrane patch under the pipette is ruptured by a short, gentle suction and/or voltage pulse event, establishing direct electrical coupling of the recording electrode and the cytosol. Upon "break-in", the cytosol is rapidly replaced with pipette solution, which allows for control of intracellular and extracellular ion concentrations. However, dialysis also dilutes cytosolic constituents that might regulate physiological processes. All recordings in the present work were performed in whole-cell configuration.

2.13.2. Human sperm patch-clamp recordings

The classical and the most straightforward method to study ion channel characteristics - the patch-clamp technique - was long believed to be inapplicable to sperm cells due to their motility and unique morphology (Fig. 1.2). Specifically, the minuscule volume of the sperm cytoplasm and the tight plasma membrane attachment to rigid intracellular structures such as the fibrous sheath and nucleus pose the main challenges.

2 Materials and methods

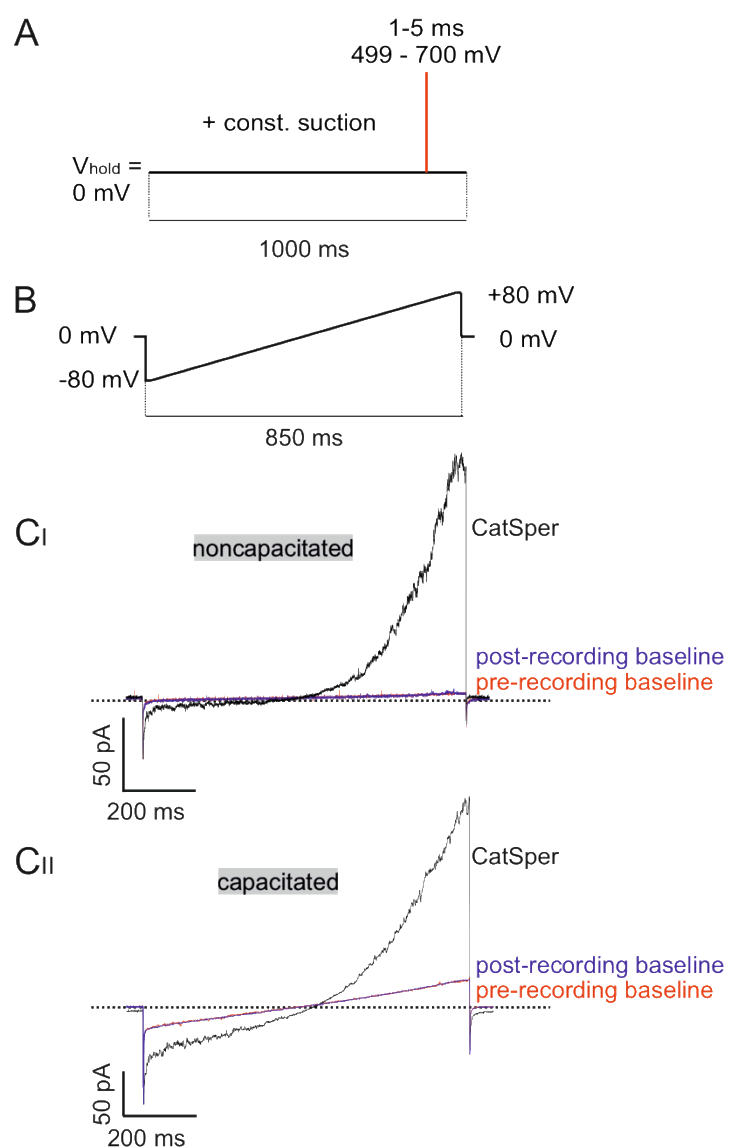
Single cells were visualized with an inverse microscope (Olympus IX71) equipped with a differential interference contrast, a 60 x Objective (Olympus UPlanSApo, water immersion, 1.2 NA, $\infty/0.13$ –0.21/FN26.5) and a 1.6 magnification changer. An AXOPATCH 200B amplifier and an AxonTM Digidata 1550A digitizer with an integrated Humbug noise eliminator were used for data acquisition. Hardware was controlled with Clampex 10.5 software (Molecular Devices). We monitored and compensated offset voltages and pipette capacitance (C_{fast}). Gigaohm seals were established at the cytoplasmic droplet of highly motile cells in standard bath solution (S3). Patch pipettes (~9–15 M Ω) were pulled from borosilicate glass capillaries with filament (1.50 mm OD / 0.86 mm) on a P-1000 horizontal micropipette puller (Sutter Instruments), fire-polished, and filled with Cs-based S8 solution. For recordings from capacitated spermatozoa, BAPTA was substituted for 5 mM EGTA and 1 mM EDTA. We confirmed that changing the chelator composition did not affect DSper current amplitudes in noncapacitated cells. Transition into whole-cell mode was achieved by applying voltage pulses (499–700 mV, 1–5 ms, $V_{hold} = 0$ mV) and simultaneous suction (Fig. 2.5). Electrophysiological recordings of human sperm were routinely performed in the voltage clamp configuration. After establishing the whole-cell mode, inward and outward currents were elicited via 0.2 Hz stimulation with voltage ramps (–80 mV to +80 mV in 850 ms, $V_{hold} = 0$ mV). Data were not corrected for liquid junction potential changes. To ensure stable recording conditions, only cells with minimal baseline currents (in S3 solution ≤ 10 pA for noncapacitated and ≤ 20 pA for capacitated cells at –80 mV) were used for experiments (Fig. 2.5). Under this condition, CatSper, DSper, KSper, and Hv1 were considered to be minimal. Thus, any remaining baseline current represented the cell's leak current. During whole-cell voltage-clamp experiments, the cells were continuously perfused with varying bath solutions utilizing a gravity-driven perfusion system. Electrophysiological experiments were performed at 22°C if not stated otherwise. The bath solution temperature was controlled and monitored with automatic temperature control. Both CatSper and DSper currents were recorded under symmetric conditions for the major permeant ion. Under these conditions, the bath solution was divalent-free (S3). To isolate DSper conductances, monovalent currents through CatSper channels were inhibited by supplementing 1 mM extracellular Mg²⁺ in the absence of EDTA (S6). To study the Na⁺

2 Materials and methods

conductance of DSper, extracellular Cs^+ was replaced by equimolar Na^+ concentrations (S7). Experiments with different bath solutions were performed on the same cell. Signals were sampled at 10 kHz and low-pass filtered at 1 kHz (Bessel filter; 80 dB/decade). Access resistance was 21–100 $\text{M}\Omega$, membrane resistance was $\geq 1.5 \text{ G}\Omega$, and membrane capacitance was 0.8–1.3 pF and served as a proxy for the cell surface area and normalized current amplitudes (i.e., current density). Capacitance artifacts were graphically removed. Representative whole-cell recordings of noncapacitated and capacitated human spermatozoa are shown in Figure 2.5 [103].

2 Materials and methods

Figure 2.5: Recording electrical currents across the plasma membrane of human spermatozoa. (A) Pulse protocol for membrane break-in. After the formation of a tight giga-ohm seal between the cytoplasmic droplet and the glass pipette, short voltage pulses combined with constant negative pressure serve to establish the whole-cell configuration. (B) Ramp protocol to elicit electrical currents across the plasma membrane. This protocol is recorded in the voltage-clamp configuration and gradually depolarizes the cell from -80 mV to +80 mV over 850 ms. The combination of intra- and extracellular solutions may selectively isolate distinct channel conductances. (C) Original current traces from representative whole-cell patch-clamp recordings of noncapacitated (C_I) and capacitated (C_{II}) human spermatozoa. Inward- and outward currents were elicited with voltage ramps as depicted in (B) every 5 s. Represented are three conditions – pre-recording baseline (in S3 solution), monovalent CatSper currents (in S5 solution), and post-recording baseline currents (in S3). Whole-cell currents returned to baseline level after switching back to S3 solution, indicating stable and minimal leak current [103].



2 Materials and methods

2.13.3. HEK cell patch-clamp recordings

HEK293 cells were transfected with the TRPV4-GFP plasmid (Fig. 2.1) as described in chapter 2.9. Electrophysiological characterization of recombinant sperm TRPV4 was then performed as described above (chapter 2.13.2). GFP-emitted fluorescence served as an indicator for TRPV4 expression. Hence, data was compared between GFP-positive and GFP-negative cells.

2.13.4. mTPC patch-clamp recordings

Whole-cell patch-clamp recordings were performed as described [15], [16], [23]. Briefly, mouse TPCs were transferred to the stage of an inverse microscope (DMI 4000B), equipped with phase contrast objectives and a cooled CCD-camera (DFC365FX, Leica Microsystems). Cells were continuously superfused with solution S1 (~ 3 ml/min; gravity flow; $\sim 22^\circ\text{C}$). Patch pipettes (~ 5 M Ω) were pulled from borosilicate glass capillaries with filament (1.50 mm OD / 0.86 mm) on a PC-10 vertical two-step micropipette puller, fire-polished, and filled with S2 solution. An agar bridge (150 mM KCl) connected reference electrode and bath solution. An EPC-10 amplifier controlled by Patchmaster 2.9 software (HEKA Elektronik) was used for data acquisition. Pipette and membrane capacitance (C_{mem}) and series resistance (R_{series}) were monitored and compensated. C_{mem} values served as a proxy for the cell surface area and, thus, for the normalization of current amplitudes (i.e., current density). Cells with unstable R_{series} values were excluded from further analysis. Liquid junction potentials were calculated by the JPCalcW software (Barry, 1994) and corrected online. Signals were low-pass filtered [analog 3- and 4-pole Bessel filters (-3 dB); adjusted to 1/3 - 1/5 of the sampling rate (10 kHz)]. Holding potential (V_{hold}) was -60 mV for continuous voltage-clamp recordings.

2.13.5. Patch-clamp recordings from mitral cells in the mouse olfactory bulb

For electrophysiological recordings from MOB or AOB mitral cells, acute parasagittal slices (chapter 2.11) were transferred to a Slice Mini Chamber and fixed with a stainless-steel anchor stringed with approximately 0.1 mm thick human hair. Care was taken not to place the hair strings on the AOB or MOB target regions. An upright fixed-stage microscope with infrared-optimized differential interference contrast (IR-DIC) optics (Leica DM LSFA) equipped with a

2 Materials and methods

20x / 0.50 NA water immersion and a 63x / 0.90 NA water immersion objective as well as a sCMOS camera (Photometrics, PrimeBSI sCMOS) was used to visualize neurons. Slices were continuously superfused with oxygenated S9 (~ 3 ml/min; gravity flow; RT). Patch pipettes (6-8 M Ω) were pulled from borosilicate glass capillaries with filament (1.50 mm OD / 0.86 mm ID) on a PC-10 micropipette puller, fire-polished, and filled with pipette solution S11. Alexa Fluor 488 hydrazide or ATTO 633 was routinely added to the pipette solution to enable on-line tracing of dendritic projections. In some recordings, biocytin [0.3% (w/v)] was added to the pipette solution to enable *post-hoc* morphological reconstruction. An agar bridge (150 mM KCl) connected the reference electrode and bath solution. An EPC-10 amplifier coupled to a 50/60 Hz noise eliminator (HumBug, Quest Scientific) was controlled by Patchmaster software (HEKA Elektronik) and was used for data acquisition. Pipette and membrane capacitance, as well as series resistance, were monitored and compensated. Liquid junction potentials were calculated using JPCalcW software (Barry, 1984) and corrected on-line. Signals were low-pass filtered [analog three-pole and four-pole Bessel filters (-3 dB); adjusted to 1/3 to 1/5 of the sampling rate (10 kHz)]. Holding potential was $V_{hold} = -70$ mV and recordings were performed in continuous voltage-clamp or current-clamp mode at varying hyperpolarizing or depolarizing potentials or injected currents, respectively. For initial characterization of the target cell, voltage-clamp step IV protocols (steps -100 mV to +80 mV, 10 mV increments, 100 ms/step, -120 mV pre-pulse for 50 ms) were performed.

2.14 Optogenetic stimulation of axon terminals in the OB

For optogenetic activation of VSN or OSN axon terminals, acute olfactory bulb slices from heterozygous OMP-ChR2-YFP mice (JAX #014173) were prepared as described in chapter 2.12. First, whole-cell configuration was established for a mitral cell and intracellular fluorophore diffusion loading occurred while the cell underwent standard characterization procedures (chapter 2.13.5). Dendritic projections were then traced online and the glomerular target region was identified. Utilizing the SysCon-operated UGA-42 Firefly and UGA-42 Geo modules (473 nm diode laser, Rapp Opto Electronic), spatiotemporally defined laser pulses were elicited within the glomerular target region while mitral cell activity was recorded in

2 Materials and methods

continuous voltage- or current-clamp mode. Cells were slightly hyperpolarized to minimize spontaneous firing interference with optogenetic responses. Various stimulation paradigms were applied (Fig. 2.6).

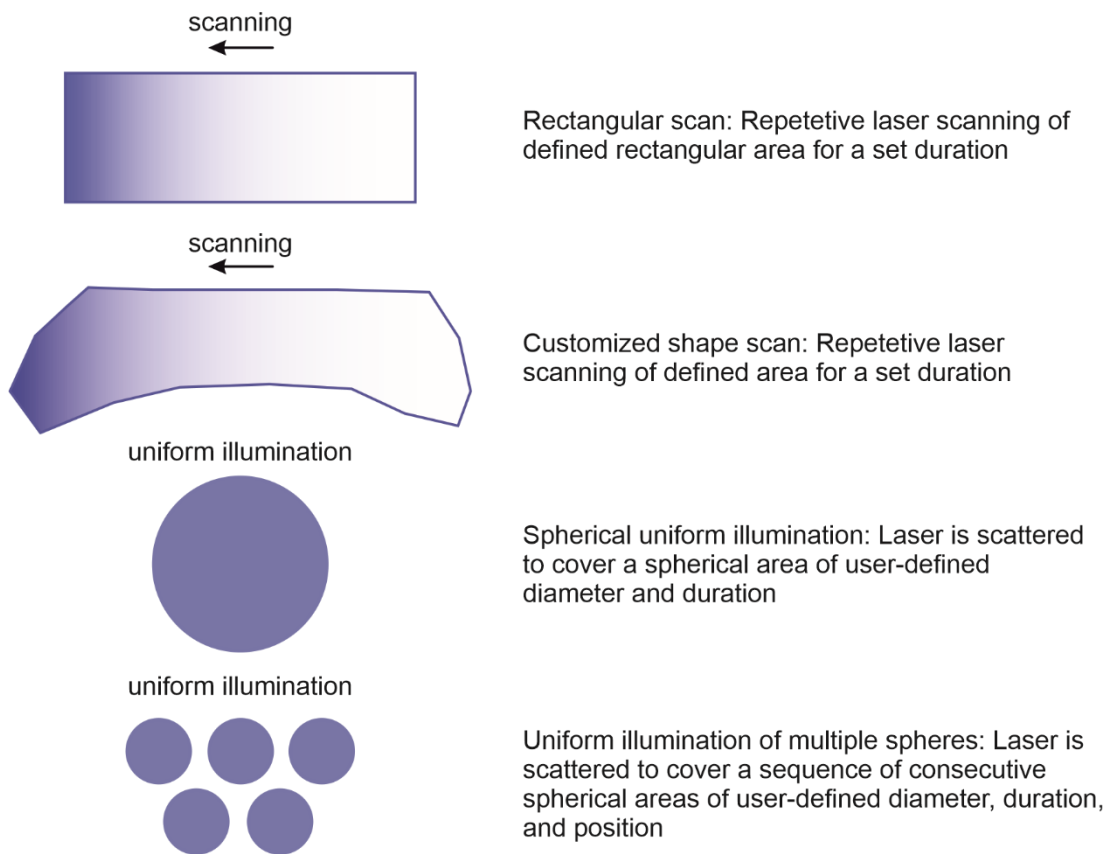


Figure 2.6: Optogenetic stimulation patterns in the glomerular layer of the olfactory bulb. Channelrhodopsin-expressing OSN or VSN axon terminals in the glomerular layer (GL) are illuminated with a 473 nm laser following the above stimulation paradigms. Dendritic tracing enables the identification of glomerular targets and precise positioning of the stimulation area. Rectangular scans and customized shape scans span the entire GL, while uniform illumination areas are targeted at and around the patched mitral cell's dendritic ending. Stimulation is performed at various durations and laser intensities.

2.15 Synthesis of recombinant darcin

2.15.1 Transformation and protein expression in *E. coli*

Chemically competent *E. coli* (BL21(DE3)) cells were transformed with the His-darcin plasmid (Fig. 2.2) by applying the heat-shock method (40 s, 42 °C) followed by incubation in SOC-

2 Materials and methods

medium (1 h, 37 °C). The cell suspension was then plated on kanamycin-containing (+Kan, 50 µg/ml) LB agar plates and incubated (37 °C, ON). A non-transformed *E. coli* suspension served as negative control. Successful transformation was confirmed by antibiotic selection on the following day. A single colony was diluted in 10 ml LB-media (+ Kan), incubated (37 °C, ON, 270 rpm), and diluted 1:500 in 600 ml autoinduction TB-medium (+ Kan) on the following day. Next, the autoinduction TB-culture was incubated for 3h at 37 °C and 21 h at RT (270 rpm). Cells were then harvested by ultracentrifugation (20 min, 4500 rcf, 4 °C), and lysed with lysis buffer S15 and sonication (1 min, cycle 0.5, Amplitude 80 %, on ice). After centrifugation (10 min, 3000 rcf, 4 °C) the supernatant contained the soluble protein fraction and the pellet was discarded.

2.15.2. *Immobilized Metal Affinity Chromatography (IMAC)*

For darcin purification, a HisPur™ Ni-NTA Spin Column was used according to the manufacturer's instructions. Briefly, the protein extract was diluted 1:1 with equilibration buffer (10 mM imidazole in 2xPBS). The column was washed with 2 ml of equilibration buffer (2 min, 700 rcf) and loaded with the protein sample. Efficient binding was ensured by 30 min incubation on an orbital shaker (270 rpm, RT). The sample was then removed by centrifugation (2 min, 700 rcf) and washed with 6 ml of washing buffer (25 mM imidazole in 2xPBS). Darcin was eventually eluted with 3x 1 ml of elution buffer (250 mM, 500 mM, 1000 mM imidazole gradient in 2xPBS). Each washing and elution step were collected in a separate tube. The column was regenerated by washing with 5 ml of MES buffer (20mM MES, 100 mM NaCl) and 5 ml of aqua dest.

2.15.3. *Rebuffering and concentration of purified darcin*

According to the manufacturer's instructions, the purified darcin eluate was rebuffered into S12 by utilizing an Amicon Ultra-4 Centrifugal Filter Unit (10 K MWCO). The final protein concentration was measured with a biophotometer (280 nm, Eppendorf) and adjusted to 1.68 mg/ml (final dilution 1:100 results in 16.8 µg/ml). The final concentration of the darcin

2 Materials and methods

stock was verified with a DC protein assay externally (UK Aachen, AG Stegmüller). Darcin was aliquoted and stored frozen at -80 °C until use.

2.16 Ectopic expression of V2R27 in the VNO

Ectopic expression of the vomeronasal receptor V2R27 was achieved by AAV-mediated gene transfer via the temporal vein as published by Lee *et al.* (2019) [246]. AAV8-smCBA-V2R27-P2A-mCherry (Fig. 2.3) was produced by the University of Florida Vector Core Lab in collaboration with Prof. Jeremy McIntyre. A 50 µl aliquot of 2.79×10^{12} vg/ml virus was injected into the temporal vein of mice on postnatal day 1 or 2 [247]. AAV8-smCBA-mCherry (1.32×10^{12} vg/ml) served as negative control. Two to four weeks after viral injection, the VNOs were dissected and acute coronal slices were investigated as described in chapter 2.12.

2.17 Ca²⁺ Imaging

2.17.1. Ca²⁺ imaging of human spermatozoa

All Ca²⁺ imaging experiments were performed in S3 solution. Before fluorescence recording, swim-up purified human spermatozoa were bulk loaded with 9 µM fluo-4/AM (dissolved in DMSO) and 0.05% pluronic (dissolved in DMSO) in S3 solution for 30 min at room temperature. Cells were then washed with dye-free S3 solution and allowed to adhere to glass imaging chambers for 1 min. Via continuous bath perfusion, the attached spermatozoa were presented with alternating extracellular conditions (S3 ± agonist/antagonist; the constant presence of 1 µM NNC55-0396 as CatSper inhibitor). Fluorescence was recorded at 1 Hz, 100 ms exposure time for different durations. Widefield fluorescence imaging was performed using a Spectra X light engine and a Hamamatsu ORCA-ER CCD camera on an inverse microscope (Olympus IX71). Fluorescence change over time was determined as $\Delta F/F_0$, where ΔF is the change in fluorescence intensity ($F - F_0$) and F_0 is the baseline intensity as calculated by averaging the fluorescence signal of the first 20 s in S3 solution. Regions of interest (ROI) were restricted to each cell's flagellar principle piece by

2 Materials and methods

manual selection in ImageJ. Statistical data are presented as mean \pm standard error of the mean (SEM), and (n) indicates the number of recorded cells[103].

2.17.2. Ca^{2+} imaging of acute VNO slices

Acute coronal VNO slices were bulk loaded with the Ca^{2+} indicator Cal520/AM (90 min, circulating ice-cold S13, 4.5 μ M Cal520/AM, 0.0005 % pluronic F-127). After extensive washing with S13, slices were transferred to an imaging chamber and fixed with a stainless-steel anchor stringed with approximately 0.1 mm thick human hair. Slices were allowed to settle for approx. 10 min to reduce movement artifacts. Continuous superfusion with oxygenated S13 (at RT) was guaranteed by a gravity-driven bath perfusion system (\sim 3 ml/min). For focal stimulation, solutions and stimuli were applied dissolved in S12 from air pressure-driven reservoirs via an 8-in-1 multi-barrel ‘perfusion pencil’. Changes in focal superfusion [23] were software-controlled and, if required, synchronized with data acquisition by TTL input to 12V DC solenoid valves using a TIB 14S digital output trigger interface. CAL520 was excited using a 488 nm laser, mCherry was excited with a 552 nm laser and emission was detected via photon-counting hybrid detectors (Leica). VNO slices were imaged on an upright fixed-stage scanning confocal microscope (Leica Multiphoton SP8 or Leica TCS SP5) equipped with 25x /1.0 NA or 20x / 1.0 NA water immersion objectives, respectively. Changes in cytosolic Ca^{2+} were monitored at 1 Hz framerate, 520 Hz unidirectional scanning speed, 1024 x 512-pixel XY resolution, and a pinhole of 3.81 airy units. Darcin or pheromone blends were applied as doublets or triplets for 10 s / stimulus with an inter-stimulus interval of \geq 3 min to avoid adaptation (dissertation Maximilian Nagel, 2020). Stimuli were: male urine, female urine, lacrimal gland extract, estrus vaginal smear (each diluted 1:100 in S12), and recombinant darcin (16.8 μ g/ml in S12). A control stimulus with a standard extracellular solution (S12) was routinely included to control for application-induced movement artifacts. A high-potassium stimulus (10 s, 50 mM, S14) at the end of each experiment served as a proxy for the number of depolarization-sensitive (i.e., viable) cells per slice and, thus, for the calculation of response rates.

2 Materials and methods

For data analysis, the average pixel intensity within user-selected regions of interest (ROIs) encompassing all depolarization-sensitive (S14) somata per field of view were calculated with ImageJ. Time-lapse fluorescence images were movement corrected with the StackReg/Rigid Body transformation plugin [248] in ImageJ. Data was processed and analyzed by Python as follows: Intensity values were background corrected and changes in relative fluorescence intensity were calculated as $\Delta F/F$ in arbitrary units, where F was defined as the mean intensity of the 20 s before the first stimulus presentation. Data was filtered by a bandpass Butterworth filter (high cutoff: 0.35 Hz; low cutoff: 0.45 mHz). Neurons were then classified as 'responsive' when showing stimulus-dependent Ca^{2+} elevations according to the following three criteria: a) exposure to high extracellular K^+ concentrations induced a robust Ca^{2+} transient, b) the peak intensity value of at least two identical stimulus presentations exceeded the average pre-stimulation baseline intensity plus two standard deviations (SDs) for at least 3 s, and c) the increase in fluorescence intensity was observed within the time window of stimulus application plus 30 s tolerance. Every responsive cell was visually verified and neurons showing potentially unspecific responses (e.g., because of high spontaneous activity or movement artifacts) were excluded.

2.18 Whole-mount seminiferous tubule imaging

Isolated tubules (>1 cm length) were transferred onto a membrane within a custom-built 3D printed two-compartment recording chamber and constantly superfused with S1. Small membrane perforations under the tubules and surrounding a defined stimulation area allowed for (i) gentle fixation of the tubules and (ii) focal ATP perfusion of selected tubular regions by vacuum-generated negative pressure (80-180 mmHg) in the submembrane chamber compartment and continuous suction of S1 from the top compartment. After visual determination of the tubular stage group (**I – III**) [249], the perfusion pencil was positioned to selectively stimulate an area of known and homogeneous cycle stage. Focal stimulation in the desired area was routinely confirmed by transient dye perfusion (Fast Green) before ATP exposure. ATP stimulations (100 μM ; 10 s) and corresponding negative controls with S1 were compared to identify ATP-dependent Ca^{2+} signals (offspring from crossing SMMHC-CreERT2

2 Materials and methods

and Ai95D mice) or tubular contractions and luminal sperm transport. For low-magnification brightfield or fluorescence imaging, a MacroFluo Z16 APO A system (Leica Microsystems) equipped with either a DFC450C camera and a PLANAPO 1.0x / WD 97 mm objective (brightfield) or with a monochrome DFC365FX camera and a 5.0x /0.50 LWD PLANAPO objective (fluorescence) was used. Images were acquired at 1 Hz [15].

2.19 RT-PCR and Cloning

2.19.1 Spermatozoa RT-PCR

Total donor-specific RNA was extracted from purified spermatozoa with a QIAGEN RNAeasy mini kit followed by complementary DNA synthesis with a Phusion RT-PCR kit (Finnzymes, MA, USA). Controls in which the reverse transcriptase was omitted were routinely performed. The donor-specific translated region of TRPV4 (cDNA) was amplified with the TRPV4-directed primer pair indicated in table 2.4. PCR amplification was performed during 30 thermal cycles (95°C, 10 s; 56°C, 30 s; 72°C, 1:30 min) and visualized via gel-electrophoresis. Sperm TRPV4 was then subcloned into a pTracer-CMV2 vector (Invitrogen) using the restriction sites: EcoRV and NotI. TRPV4 identity was sequence verified.

2.19.2. TPC RT-PCR

Total RNA was isolated and purified from cultured mouse TPCs (passage 1) by Trizol/chloroform precipitation, followed by complementary DNA synthesis with a RevertAidTM H Minus kit (#K1632, Thermo Fisher) according to the manufacturer's instructions. Negative controls in which the reverse transcriptase enzyme was omitted were routinely performed. PCR amplification was performed during 30 thermal cycles (95°C, 20 s; 58°C, 20 s; 72°C, 20 s) with primers as indicated in table 2.4.

2.20 Immunochemistry

2.20.1. Immunocytochemistry of human spermatozoa

Purified spermatozoa were plated onto 20 mm coverslips in S1 and allowed to attach for 20 min. The cells were fixed with 4% paraformaldehyde (PFA) in PBS for 20 min and washed twice

2 Materials and methods

with PBS^{-/-}. Additional fixation was performed with 100% ice-cold methanol for 1 min with two washing steps in PBS^{-/-}. Cells were blocked and permeabilized by 1 h incubation in PBS^{-/-} supplemented with 5% immunoglobulin-γ (IgG)-free BSA and 0.1% Triton X-100. Immunostaining was performed in the same blocking solution containing the primary antibody, polyclonal α-TRPV4 (1:100, overnight at 4°C). After extensive washing in PBS^{-/-}, secondary antibodies (mouse monoclonal α-Rabbit-DyLight488, 1:2000) were added for 45 min at RT. After vigorous washing, cells were mounted with ProLong Gold Antifade with DAPI reagent (Life Technologies, Carlsbad, CA) and imaged with a confocal microscope. Digital images were uniformly adjusted for brightness and contrast using Adobe Photoshop CS6 [103].

2.20.2 Immunocytochemistry of cultured TPCs

Immunostaining of cultured mouse TPCs was performed as described in [15]. In detail, cells were washed (3x; PBS^{-/-}), fixed with ice-cold 4% PFA in PBS^{-/-} (20 min; RT), and washed again (3x; PBS^{-/-}). For blocking, cells were incubated in PBS^{-/-} containing Tween-20 (0.1%)/BSA (3%) solution (1 hr; RT). After washing (PBS^{-/-}; 2 × 5 min), cells were incubated with FITC-conjugated monoclonal anti-actin, α-smooth muscle antibody (1:500 in 3% BSA; 1 hr; RT). Excess antibodies were removed by washing (2 × 5 min PBS^{-/-}). Nuclear counterstaining was performed by incubation in PBS^{-/-} and either DAPI (5 µg ml⁻¹; 10 min; RT) or DRAQ5 (1:500; 5 min; RT).

Fluorescent images were taken using either an inverted microscope (Leica DMI4000B, Leica Microsystems) or an upright fixed stage scanning confocal microscope (TCS SP4 DM6000 CFS; Leica Microsystems) equipped with a 20 × 1.0 NA water immersion objective (HCX APO L; Leica Microsystems). To control for non-specific staining, experiments in which the primary antibody was omitted were performed in parallel with each procedure. Digital images were uniformly adjusted for brightness and contrast using Adobe Photoshop CS6.

2 Materials and methods

2.20.3 Immunohistochemistry of testicular cryosections

For immunochemistry of testicular cryosections, testes were fixed with 4% (w/v) paraformaldehyde (PFA) in PBS^{-/-} (10 mM, pH 7.4; ≥12 h; 4°C) and subsequently cryoprotected in PBS^{-/-} containing 30% sucrose (≥24 h; 4°C). Samples were then embedded in Tissue Freezing Medium (Leica Biosystems), sectioned at 20 µm on a Leica CM1950 cryostat (Leica Biosystems), and mounted on Superfrost Plus slides (Menzel, Braunschweig, Germany). For blocking, sections were incubated in PBS^{-/-} containing Tween-20 (0.1%) / BSA (3%) solution (1 h; RT). After washing (PBS^{-/-}; 2 x 5 min), sections were incubated with FITC-conjugated monoclonal anti-actin, α-smooth muscle antibody (1:500 in 3% BSA; 1 h; RT). Excess antibodies were removed by washing (2 x 5 min PBS^{-/-}). For nuclear counterstaining, sections were then incubated in PBS^{-/-} containing DRAQ5 (1:500; 5 min; RT; Thermo Fisher Scientific). Fluorescent images were taken using an upright fixed stage scanning confocal microscope (Leica Microsystems, TCS SP4) equipped with a 20 x 1.0 NA water immersion objective. To control non-specific staining, experiments in which the primary antibody was omitted were performed parallel with each procedure. Digital images were uniformly adjusted for brightness and contrast using Adobe Photoshop CS6 [15].

2.21 Immunoblotting

2.21.1 Western Blot analysis of TRPV4 expression in human spermatozoa, testicular tissue, and transfected HEK cells

The highly motile sperm fraction was separated from other somatic cells by density gradient consisting of 90% and 50% isotonic ISolate solution diluted in S3 solution with the addition of protease inhibitors (Roche). Protease inhibitors were used throughout the whole procedure. After centrifugation at 300 g for 30 min at 24°C, the sperm pellet at the bottom of the 90% layer was collected, diluted ten times, and washed in S3 by centrifugation at 2000 g for 20 min. Cells were examined for motility and counted before centrifugation. Contamination of the pure sperm fraction by other cell types was minimal, with less than 0.2% of somatic cells, which was below the protein detection threshold for immunoblotting applications. Next, the pellet was subjected to osmotic shock by a 5 min incubation in 0.5x S3 solution, the addition

2 Materials and methods

of 10 mM EDTA and 10 mM DTT for 10 min, and sonication in a water bath at 25°C for 5 min. The addition of 10x PBS adjusted osmolarity. Laemmli sample buffer (5x) was added to a final 1x concentration, and the DTT concentration was adjusted to 20 mM. An additional 5 min sonication and boiling at 100°C for 5 min were performed. The total crude cell lysate was loaded onto a 4–20% gradient Tris-HCl Criterion SDS-PAGE (BioRad) with 500,000 sperm cells/well.

TRPV4- and empty vector-transfected HEK293 cells were lysed in 2x Laemmli sample buffer, boiled (95 °C, 5 min), and subjected to SDS-PAGE (10000 cells / well).

After transfer to polyvinylidene fluoride membranes, blots were blocked (0.1% PBS-Tween-20, 3% IgG-free BSA, 15 min) and incubated with α -TRPV4 antibody overnight at 4°C. Blots were probed with rabbit anti- β -tubulin antibodies as a positive control. After subsequent washing and incubation with secondary horseradish peroxidase-conjugated antibodies, membranes were developed with an ECL SuperSignal West Pico kit (Pierce).

2.21.2 Immunoblotting and Coomassie staining of recombinant darcin

Protein extracts of various steps of the darcin synthesis pipeline were mixed with 2x Laemmli sample buffer, boiled (5 min, 95 °C), and subjected to SDS-Page (BioRad, 15 min, 100 V; 60 min, 150 V). For unspecific staining of protein bands, the acrylamide gel was stained by brief boiling in the microwave covered with coomassie blue solution (40 % methanol, 10 % acidic acid, 1 g/l coomassie) and incubation for 30 min with agitation. Bands became obvious upon incubation with destain solution (20 % methanol, 7 % acidic acid) (ON, with agitation).

After transfer to a nitrocellulose membrane (semi-dry procedure, BioRad, 7 min, 2.5 A, 25 V), blots were blocked (5 % skim milk powder in 0.1% PBS-Tween20, 30 min) and probed with either anti-6xHis tag® or anti-MUP20 (table 2.3) primary antibodies (in blocking solution, 4 °C, ON). After subsequent washing with 0.1% PBS-Tween20, and incubation with secondary peroxidase-conjugated antibodies (2.5 % skim milk powder in 0.1% PBS-Tween20, 45 min, RT), blots were developed with an ECL SuperSignal West Pico kit (Pierce).

3 Results

Project A: ATP activation of peritubular cells drives testicular sperm transport

The aim of this subproject is to elucidate mechanisms of luminal sperm transport and investigate a potential involvement of extracellular ATP as an activation mechanism of contractile TPCs. The results presented in this chapter have been published in Fleck, Kenzler *et al.* [15]. The majority of the data have been acquired by myself. Complementing contributions by others are stated in chapter 7.

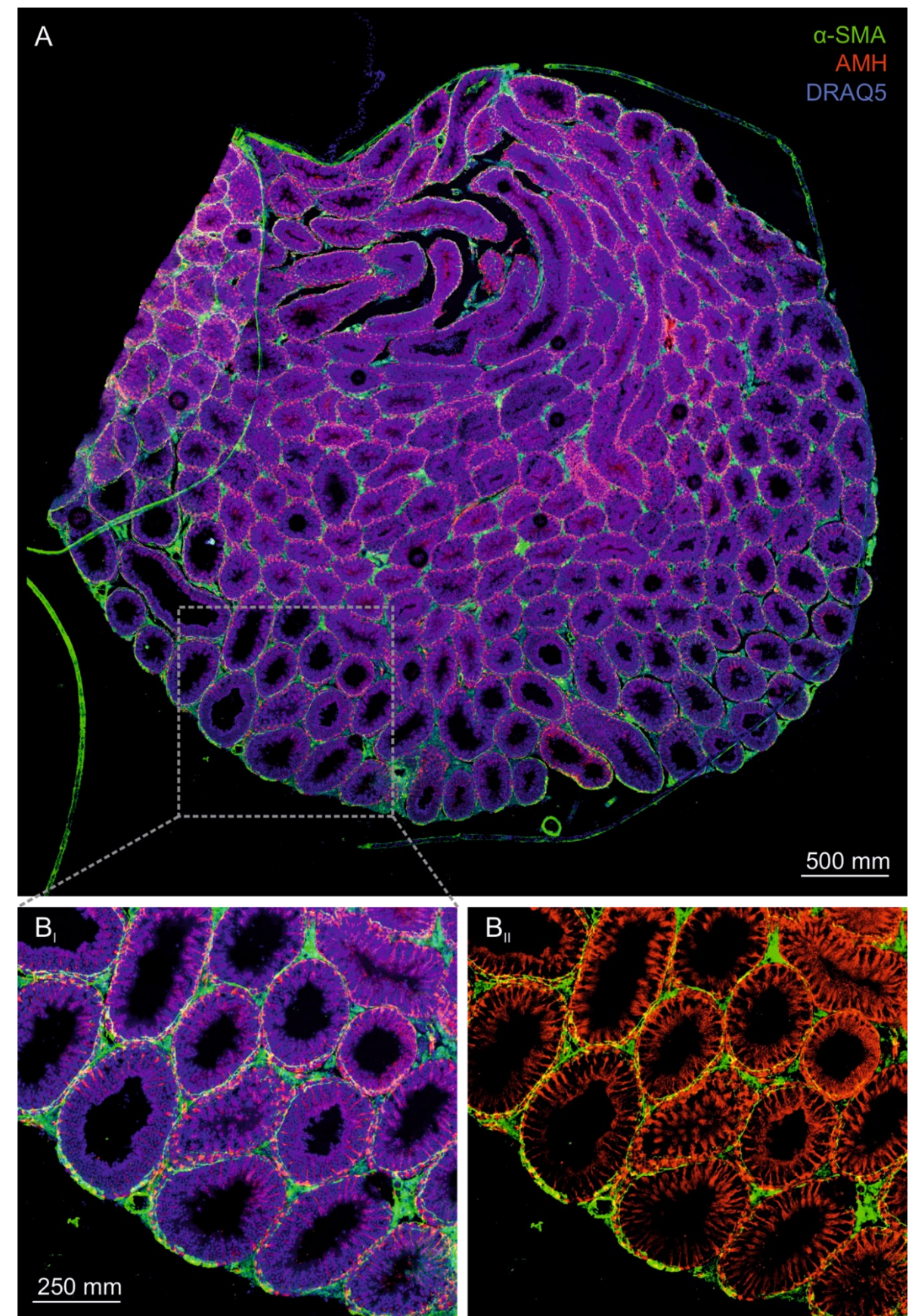
3.1 Extracellular ATP is a potent TPC stimulus

First, I asked if mouse TPCs are sensitive to extracellular ATP. To answer this question, I utilized a primary culture of mouse TPCs. The identity of TPCs was verified by an α -smooth muscle actin (α -SMA) antibody, a marker for smooth muscle cells [250] (Figure 3.1). Immunopositive cells are localized in the tubule walls of AMH-Cre x Ai14D mice and do not overlap with the Sertoli cell-specific expression of tdTomato. As expected, the α -SMA antibody also stains the tunica albuginea, a tissue capsule that surrounds the testis and contains smooth muscle cells. Primary TPC cultures retain high purity for ≥ 14 days *in vitro*, indicated by the vast majority of α -SMA positive cells in passages 1 and 2 (Figure 3.2 A). Cultured TPCs express transcripts for several ionotropic (P2X2, P2X4, P2X7) and metabotropic (P2Y2, P2Y6) purinoceptors (Figure 3.2 B) and functional expression of ionotropic P2X2 and/or P2X4, but not P2X7, is strongly suggested by the specific biophysical and pharmacological profile of ATP-dependent transmembrane currents (Figure 3.2 C). In accordance with the reported ATP sensitivity for P2X2 and P2X4 [251], TPC currents saturate at ≤ 100 μ M ATP (Figure 3.2 D), while P2X7 displays strongly reduced ATP sensitivity in this concentration range [252]. Furthermore, the ATP-induced current showed modest but persistent desensitization (Figure 3.2 E), a feature that is attributed to recombinant P2X2 and P2X4, but not P2X7 [253]. The pharmacological profile of ATP-dependent currents in TPCs is heterogeneous, with a subpopulation of TPCs being

3 Results

potentiated by the selective P2X4 agonist ivermectin [254] (n=7/12, Figure 3.2 F-G). Suramin, a drug antagonizing P2X2, but not P2X4 [255], inhibited a TPC subset (n=10/18, Figure 3.2 F-G). Together, these data suggest that mouse TPCs express both ionotropic and metabotropic purinoceptors and that both P2X2 and P2X4 carry out the ionotropic ATP-response.

3 Results



3 Results

Figure 3.1: α -SMA antibody stains TPCs located in the tubular wall. (A) In testis cryosections from adult AMH-Cre x Ai14D mice, Cre-driven and Sertoli cell-specific tdTomato signals do not colocalize with smooth muscle-specific α -SMA immunostaining. Green immunofluorescence of the α -SMA antibody localizes exclusively to tubular margins, the tunica albuginea, and vasculature. Nuclei are stained with DRAQ5 (blue). (B) Higher magnification view of the indicated inset in (A). Arrow points at immunopositive TPCs; the asterisk indicates endothelial vasculature.

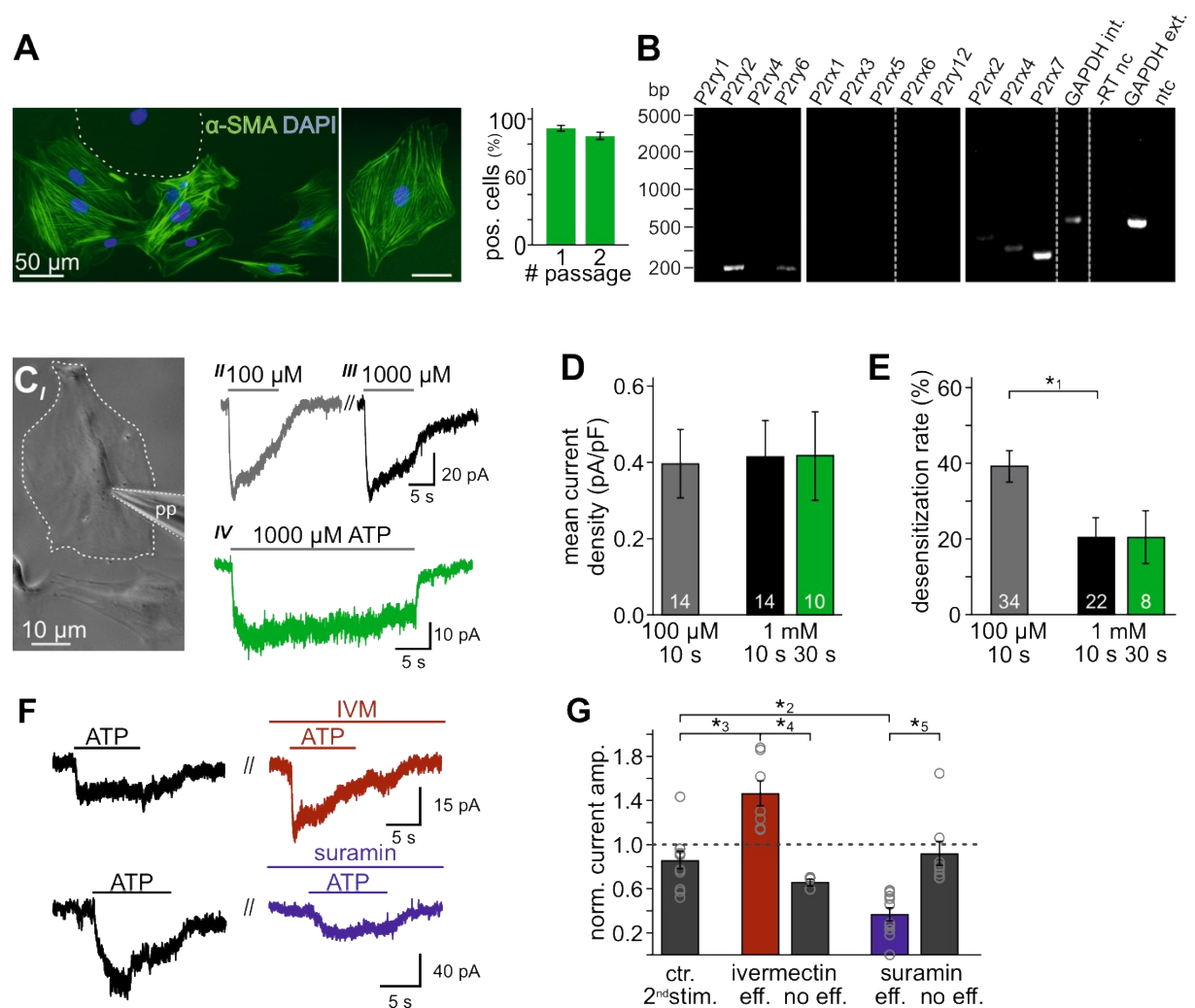


Figure 3.2: Extracellular ATP is a potent TPC stimulus. (A) Immunostaining against α -SMA (green) marks TPCs in vitro. Cell count is determined by nuclear staining with DAPI (blue). Primary cultures maintain high TPC purity for at least two passages ($92 \pm 2\%$, $n = 1102$ (#1); $86 \pm 3\%$, $n = 542$ (#2)). The dashed line delimits one of the few α -SMA-negative cells. (B) RT-PCR screening for purinoreceptor isoform transcripts detects $P2rx2$, $P2rx4$, $P2rx7$, $P2ry2$, and $P2ry6$. Dashed gray vertical lines indicate cuts in a given gel. GAPDH int. served as a positive control for mRNA extraction, GAPDH ext. controls for successful reverse transcription into cDNA, and both -RT (without reverse transcriptase) and ntc (no template control) experiments exclude

3 Results

(genomic) contamination. **(C-G)** Whole-cell patch-clamp recordings of cultured TPCs reveal that ATP exposure triggers transmembrane currents. **(C_I)** Phase-contrast micrograph depicting a TPC (dashed line) targeted by a patch pipette (pp). **(C_{II}-C_{IV})** Original whole-cell recordings illustrate representative currents in response to extracellular ATP stimulation (100 μ M **(C_{II})** vs. 1000 μ M **(C_{III})** and 10 s **(C_{III})** vs. 30 s **(C_{IV})**, respectively). $V_{hold} = -80$ mV. **(D, E)** Quantification (bar charts; mean \pm SEM; n as indicated) reveals saturation of peak current density at \leq 100 μ M ATP **(D)** and modest desensitization at a concentration-dependent rate **(E)**. **(F)** Whole-cell voltage-clamp recordings show ATP-induced currents (100 μ M; 10 s) that are potentiated by ivermectin (3 μ M) and partially inhibited by suramin (100 μ M), respectively (\geq 60 s preincubation). $V_{hold} = -80$ mV. **(G)** Quantification (bar charts; mean \pm SEM; data normalized to initial control response) shows heterogeneity in drug sensitivity. Treatment was categorized as effective (eff) if current amplitudes deviate by \pm SD from average control recordings ($0.85 \pm 24\%$, 2nd ATP stimulation). Note that each drug proved ineffective (no eff) in some cells. Gray circles depict data from individual cells. $^{*1}p=0.001$; $^{*2}p=0.002$; $^{*3}p=5.5e^{-5}$; $^{*4}p=0.0006$; $^{*5}p=0.02$; Student t-test **(E)**, ANOVA **(G)**. (Adapted from: Fleck, Kenzler et al. (2021) [15])

3.2 ATP triggers seminiferous tubule contractions and drives directional luminal transport

Next, I asked if TPCs also exhibit ATP sensitivity in their physiological setting and whether TPC activation could lead to tubule contractions. To test this, I utilized a custom-built whole-mount macroscopic imaging platform that allowed both widefield and fluorescence time-lapse imaging of intact seminiferous tubules (Figure 3.3 A). In addition, this setup enables visual categorization of the spermatogenic cycle into three distinct stage groups following published protocols [8] and allows precisely timed focal perfusion (region of interest 0 (ROI0), methods). First, I asked if brief focal purinergic stimulation elicits tubule contractions and, consequently, luminal content movement. Flow field change analysis indicates minimal basal luminal motion independent of mechanical stimulation (Figure 3.3 B). However, ATP exposure triggered a substantial increase in luminal flow that outlasted the presence of ATP for several tens of seconds (Figure 3.3 B).

3 Results

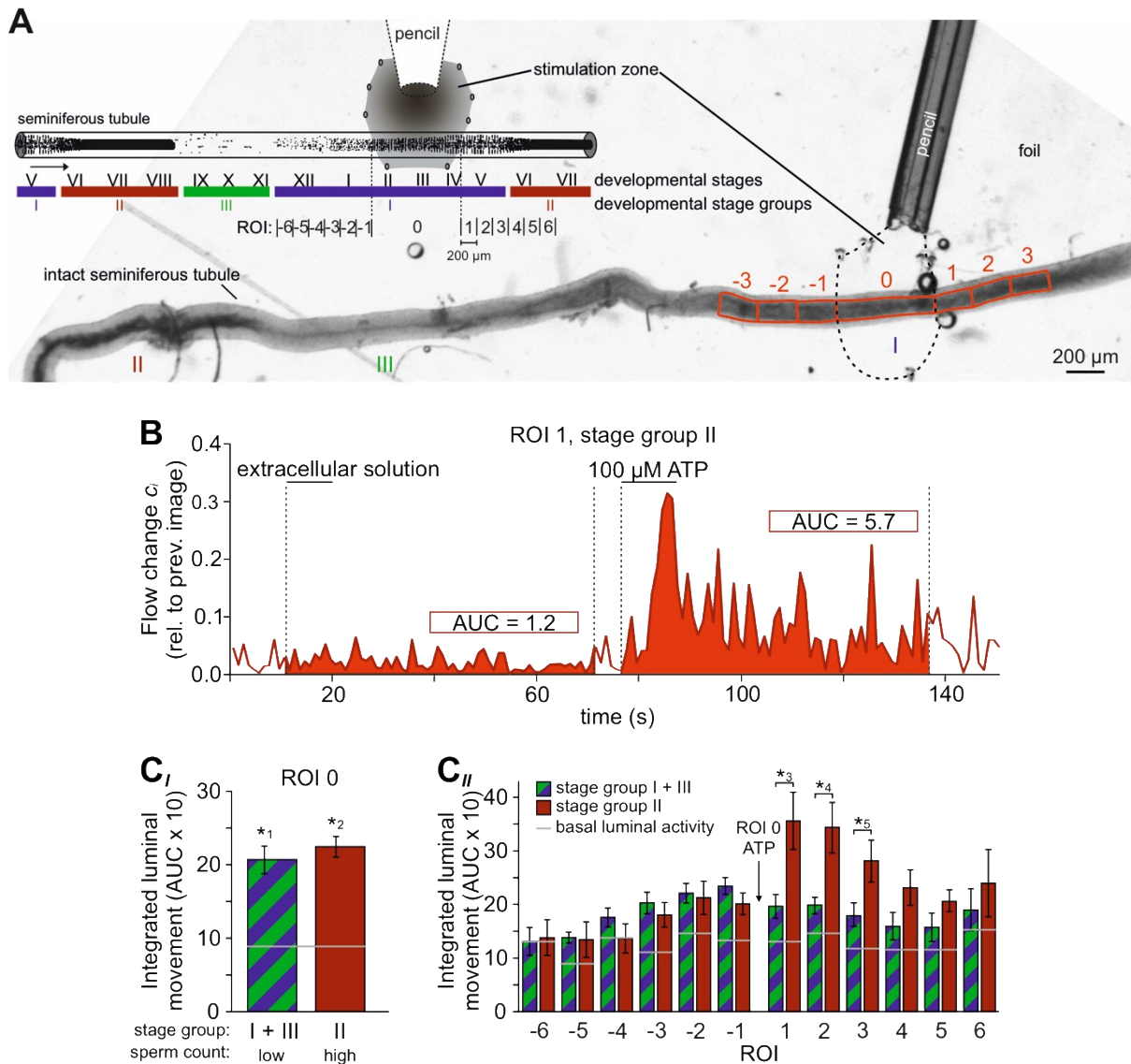


Figure 3.3: ATP drives directional luminal transport. (A) Schematic illustration (top) and original low-magnification image (bottom) of the experimental setup. Intact seminiferous tubules are transferred on a transparent membrane in a custom-built macroscopic imaging chamber. The tubule is kept stationary by gentle suction through tiny holes punched in the foil and vacuum underneath. As previously suggested [8], tubules are coarsely categorized into three stage groups (I–III; color code) according to luminal sperm content. Precise mapping of stimulated regions is feasible by positioning both tubule and perfusion pencil within an area delimited by several holes that outline a stimulation zone (methods). The tubule region directly exposed to ATP is designated as ROI 0, with adjacent equidistant 200 μ m sections numbered consecutively (up to ROI \pm 6; schematic). In the original tubule image shown, only ROIs \pm 3 are outlined for clarity. **(B)** Analysis of luminal content movement by calculation of flow change c_i relative to each previous image (methods) within a representative luminal ROI 1. Movement is quantified by measuring the area under curve (AUC; solid red) within 60 s after stimulation onset. Note that mechanical control stimulation (S1 solution) does not affect basal luminal motion. **(C)** Bar charts depicting luminal movement (means \pm SEM) upon ATP stimulation (100 μ M; 10 s) in either directly exposed regions (**C_I**; $n = 17$) or adjacent areas (**C_{II}**; $n = 3–17$).

3 Results

*Green/blue (groups I and III) and red (group II) bars include stages with a low vs. a high luminal sperm count, respectively. Horizontal gray lines indicate the average basal motion prior to stimulation as calculated for the mechanical control stimulus. ATP stimulation induces significantly increased content movement in directly exposed areas (ROI 0) independent of luminal sperm count/stage group (C_I). Note that in adjacent regions (C_{II}) unidirectional movement occurs exclusively in tubule sections with high luminal sperm density (stage group II). Asterisks denote statistically significant differences (*1p=8.7e-5; *2p=6.7e-7; *3p=0.005; *4p=0.002; *5p=0.03; unpaired two-tailed t-test) (adapted from: Fleck, Kenzler et al. (2021)[15]).*

Second, I analyzed if luminal movement is dependent on the tubule's cycle stage and, thus, luminal sperm count. I analyzed ATP-induced movement in directly stimulated luminal regions (designated as region-of-interest (ROI) 0) and compared stage groups with a high (stage group II) vs. a relatively low (stage groups I and III) amount of luminal sperm. Interestingly, I observed no difference in stimulation-dependent motion (Figure 3.3 C_I). Thus, direct ATP exposure triggers tubular contractions independent of cycle stage and luminal sperm count. Third, I investigated if luminal movement is restricted to the area of direct stimulation (ROI 0) or, by contrast, if fluid flow propagates beyond the directly stimulated tubule section (ROIs ≥ 1 and ROIs ≤ -1). When I analyzed luminal motion in equidistant tubule sections adjacent to the directly stimulated area ROI 0 (Figure 3.3 C_{II}), I observed a significant, though relatively small bidirectional wave of propagating movement in stage groups I and III, which exhibit a low luminal sperm count. Strikingly, I observed strong unidirectional luminal movement upon ATP stimulation of stage group II tubule sections which show high luminal sperm density associated with spermiation (Figure 3.3 C_{II}). In this stage group, luminal content is predominantly propelled toward areas of ascending spermatogenic cycle stages. These findings demonstrate the directionality of sperm transport upon focal purinergic TPC stimulation in isolated seminiferous tubules [15].

A rise in cytosolic Ca^{2+} precedes muscle contractions. Since ATP can trigger TPC contractions, I hypothesized that ATP would trigger Ca^{2+} transients in TPCs that could mediate the contractile motion of the seminiferous tubule. I also speculated that a unidirectional wave-like progression of Ca^{2+} signals along the longitudinal axis of the tubule could be the mechanism for directional sperm transport observed before. To visualize Ca^{2+} dynamics within

3 Results

the intact seminiferous tubule, I utilized conditional gene targeting via the Cre/Lox system [256]. This system allows TPC-specific expression of the single-wavelength Ca^{2+} indicator GCaMP6f. First, I confirmed the inducible TPC-targeted testicular expression of fluorescent reporter proteins in SMMHC-CreERT2 x Ai14D mice (Figure 3.4 A). Tamoxifen-induced transgenic expression of CreERT2 under control of the mouse smooth muscle myosin, heavy polypeptide 11 (a.k.a. SMMHC) promoter drives Cre-mediated recombination of loxP-flanked reporters (here tdTomato) in TPCs [257]. As expected, in testicular cryosections from adult SMMHC-CreERT2 x Ai14D mice, Cre-driven tdTomato signals and α -SMA immunostaining colocalize at tubular margins, confirming conditional TPC gene targeting. Next, I investigated seminiferous tubules of SMMHC-CreERT2 x Ai95D (GCaMP6f) mice in the previously described whole-mount imaging platform (Fig. 3.4 B-C). As expected, ATP-induced tubule contractions also manifest as Ca^{2+} signals in TPCs. However, these Ca^{2+} elevations are limited to those areas directly exposed to ATP (ROI 0). I observed no such signals in adjacent tubule sections independent of the stimulated stage group or an ascending or descending stage direction (Figure 3.4 D). This finding suggests that, in the isolated seminiferous tubule, ATP acts as a local paracrine messenger that, by itself, is insufficient to trigger a signal that propagates in a regenerative wave-like fashion along a tubule's longitudinal axis. However, local contractions generate sufficient force to move luminal content beyond the directly stimulated area and, in

3 Results

turn, the directionality of flow along short-to-medium distances ($\leq 600 \mu\text{m}$; Figure 3.3 C_{II}) is not critically dependent on peristaltic contractility [15].

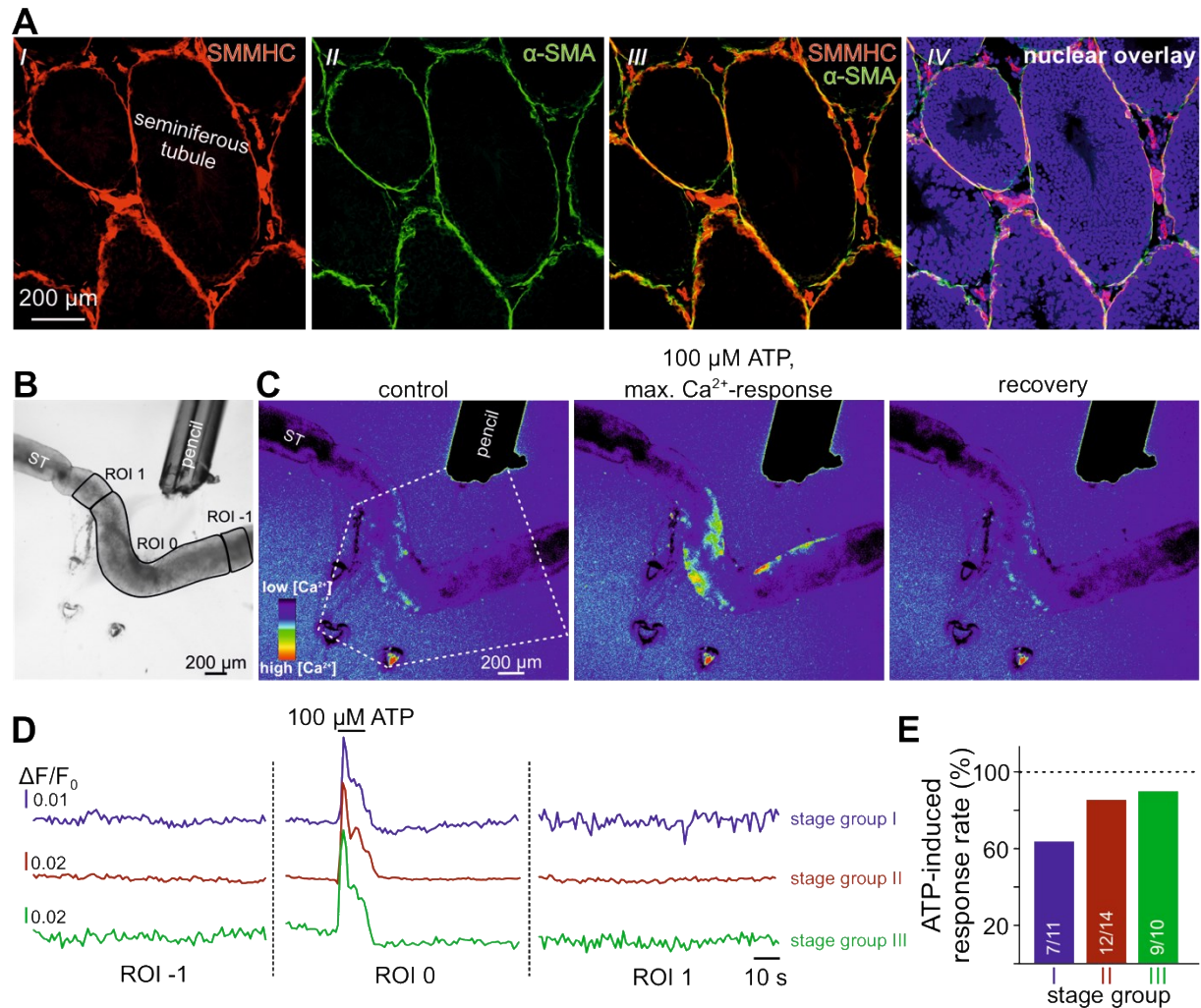


Figure 3.4: ATP causes Ca^{2+} elevations within a restricted paracrine radius. (A) SMMHC-CreERT2-expressing cells in the tubule wall are TPCs. In testis cryosections from adult SMMHC-CreERT2 x Ai14D mice, Cre-driven tdTomato signals (A_I) and α -SMA immunostaining (A_{II}) colocalize at tubular margins (A_{III}). Nuclei are stained with DRAQ5 (blue (A_{IV})). (B) Low-magnification brightfield image of an intact seminiferous tubule segment dissected from SMMHC-CreERT2 x Ai95D mice positioned directly in front of a 250 μm diameter perfusion pencil. ROIs (black lines) are defined to encompass the directly stimulated area (ROI 0) as well as adjacent regions (ROIs 1 and -1), respectively. The suction produced by negative pressure (applied through holes in the elastic foil pad beneath the tubule) limits the area of perfusion. (C) Pseudocolor GCaMP6f fluorescence intensity images of the tubule shown in (B) reveals ATP-induced Ca^{2+} transients in TPCs. Depicted representative images (rainbow 256 color map) correspond to time points before, during, and after focal ATP exposure (100 μM ; 10 s). The white dotted lines denote the area directly challenged with ATP. For clarity, the autofluorescence of the perfusion pencil was removed. Note that Ca^{2+} elevations are restricted to ROI 0. (D) Representative original recordings of changes in GCaMP6f intensity ($\Delta F/F$) over time in tubule segments of the three different stage groups (I–III). Traces exemplify Ca^{2+} signals (or the lack

3 Results

thereof) in ROIs 0, -1, and 1, respectively. Independent of the epithelial cycle stage investigated, ATP-induced Ca^{2+} elevations are restricted to directly exposed tubule segments. (E) Quantification of ATP sensitivity among tubule segments of different cycle stages. Bar charts demonstrate that purinergic stimulation causes Ca^{2+} signals independent of stage and, thus, luminal sperm count. Numbers of experiments as indicated in bars, statistical insignificance confirmed by χ^2 test (adapted from: Fleck, Kenzler et al. (2021)[15]).

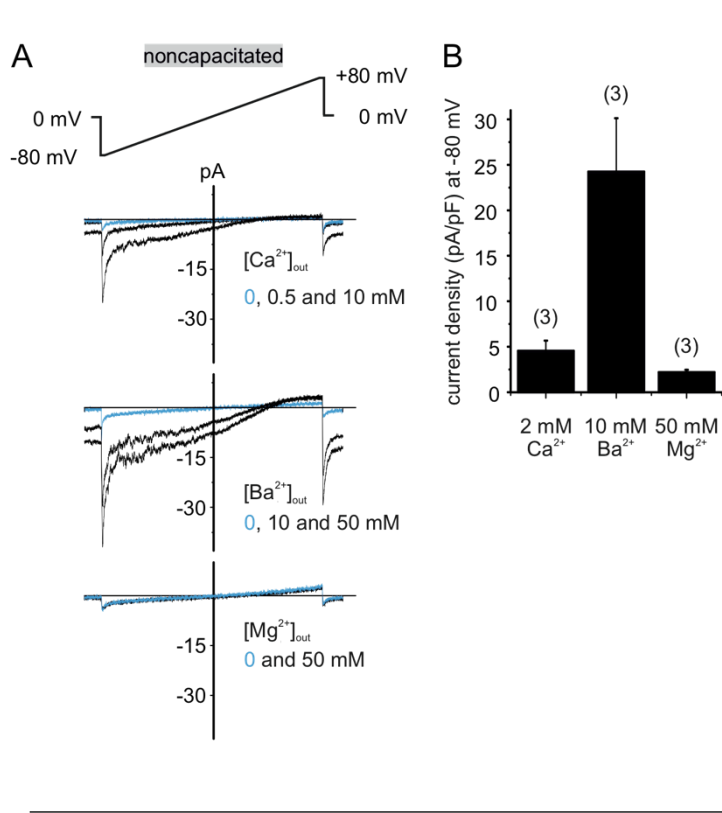
Project B: Electrophysiological characterization of "DSper"

The aim of this subproject is to record and characterize hDSper, the "depolarizing ion channel of human sperm" [102], by means of electrophysiology. Ultimately, my goal is to resolve the molecular identity of human DSper. Most of the results presented in this chapter have been published in Mundt *et al.* [103]. The majority of the data have been acquired by myself. Complementing contributions by others are stated in chapter 7.

3.3 A novel non-CatSper conductance of human spermatozoa

In the absence of divalent ions from the extracellular space (divalent-free conditions, DVF), CatSper conducts monovalent cations and represents the most prevailing cation conductance in human spermatozoa [84], [89]. CatSper is also permeable to Ca^{2+} and Ba^{2+} , but it cannot conduct Mg^{2+} , as indicated in Figure 3.5. When the major permeable extracellular cation is Ca^{2+} or Ba^{2+} , negative membrane potentials induce concentration-dependent inward currents. In the presence of extracellular Mg^{2+} , however, CatSper currents are not elicited. Under this condition, extracellular Mg^{2+} blocks the CatSper pore, resulting in the inhibition of monovalent CatSper currents (I_{CatSper}).

3 Results



Quantification of current densities (pA/pF) for either Ca^{2+} , Ba^{2+} , or Mg^{2+} inward currents through CatSper (From: Mundt et al. (2018), [103], data provided by Polina Lishko).

In whole-cell voltage-clamp recordings from human ejaculated spermatozoa, inward and outward currents could be elicited by voltage ramps that resembled the classical CatSper kinetic ($I_{CatSper}$) [89]. However, when $I_{CatSper}$ was blocked with 1 mM extracellular Mg^{2+} , residual currents were consistently observed (Fig. 3.6 A, B). Cs^+ inward and outward currents elicited under DVF condition (black traces and bars) were more prominent than currents recorded in the presence of Mg^{2+} (red traces and bars) (Fig. 3.6 A-C). This observation was made in both noncapacitated and capacitated spermatozoa. Notably, capacitated cells consistently showed increased current densities under both conditions. Potassium and proton conductances were inhibited by intracellular Cs^+ and in absence of a pH gradient required for $Hv1$ activity. Hence, the data suggests that the remaining conductance is a novel non-CatSper conductance via the yet-to-be-identified DSper ion channel. DSper currents were potentiated during capacitation (Fig. 3.6 B) and exhibited outward rectification, though DSper currents recorded from capacitated cells were notably less rectifying. The remaining DSper component is unlikely a

Figure 3.5: Human CatSper conducts Ca^{2+} and Ba^{2+} but not Mg^{2+} . (A) Original current traces from whole-cell voltage-clamp recordings of noncapacitated human spermatozoa. Inward- and outward currents were elicited with voltage ramps as depicted. Pipette solution was: 140 mM NMDG, 100 mM HEPES, 5 mM EGTA, 5 mM EDTA, 330 mOsmol, pH 7.3, composition of bath solution was: 500 nM P4, 100 mM HEPES, 130 mM NMDG, plus X mM Ca^{2+} , Ba^{2+} or Mg^{2+} as depicted, 317 mOsmol, pH 7.4. When the major permeable extracellular cation was Ca^{2+} or Ba^{2+} , negative membrane potentials induced concentration-dependent inward currents. In the presence of Mg^{2+} , CatSper currents remained unchanged (0 mM), indicating that human CatSper is impermeable for Mg^{2+} . (B)

3 Results

remnant of an increased leak current since the cells returned to their initial ‘baseline’ current after returning to the S3 bath solution. The physiologically relevant entity to be analyzed is cation influx as it represents channel activity under physiologically relevant conditions and ensures membrane depolarization. Therefore, DSper inward currents elicited by the change of membrane potential from 0 mV to -80 mV were preferentially analyzed. To rule out ‘contamination’ of putative I_{DSper} with remaining $I_{CatSper}$, I next tested whether 1 mM Mg^{2+} is sufficient to completely block $I_{CatSper}$ and selectively isolate DSper currents. The CatSper inhibitor NNC 55–0396 (NNC) [89], [258] did not elicit any additional inhibitory effect on inward I_{DSper} (Fig. 3.6 D-F), confirming efficient CatSper pore block by Mg^{2+} .

3 Results

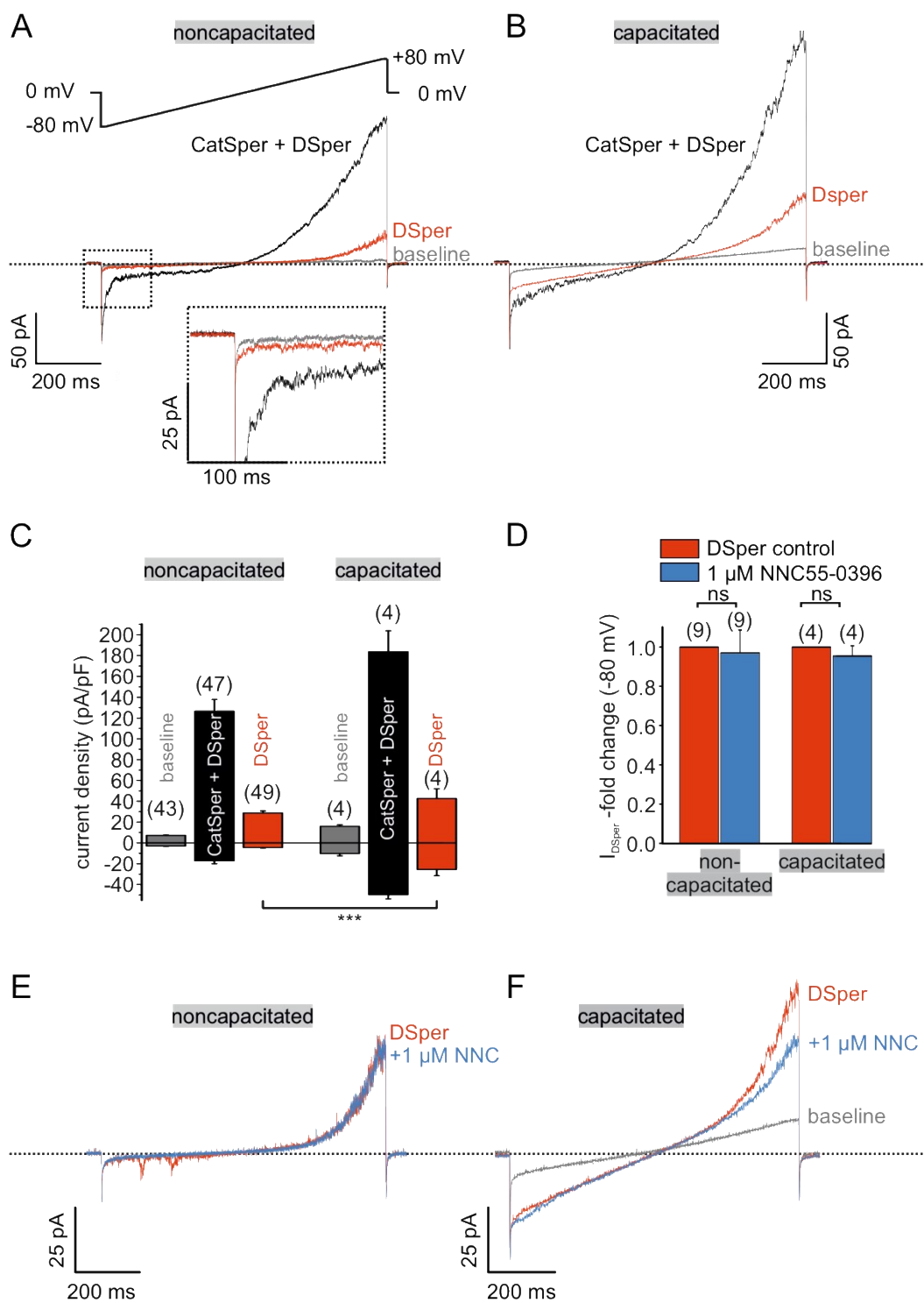


Figure 3.6: Electrophysiological recordings reveal a novel non-CatSper conductance. (A-B) Original current traces of representative whole-cell patch-clamp recordings from noncapacitated (A) and capacitated (B) human spermatozoa. Inward- and outward currents were elicited with voltage ramps as depicted in (A). Under divalent free conditions (black traces), typical CatSper monovalent cesium currents can be recorded. In the presence of 1 mM extracellular Mg^{2+} (red traces), an outward rectifying "DSper" current component remains.

3 Results

Hence, the black traces represent a mixture of both CatSper and DSper currents, while the red traces show pure Cs^+ and Mg^{2+} currents through DSper. Inset in (A) shows magnified current traces indicated by the dashed box. (C) Quantification of current densities for all three conditions in (A-B). DSper currents are increased upon capacitation (noncapacitated cells: $-4.50 \pm 0.41 \text{ pA/pF}$, capacitated cells: $-25.58 \pm 5.88 \text{ pA/pF}$ for inward currents recorded at -80 mV ; noncapacitated cells: $28.80 \pm 1.93 \text{ pA/pF}$, capacitated cells: $42.67 \pm 9.27 \text{ pA/pF}$ for outward currents recorded at $+80 \text{ mV}$). Quantification of normalized DSper inward currents (D) and original current traces (E-F) in the presence and absence of the CatSper inhibitor NNC 55-0396 demonstrate the absence of inhibition. Data are mean \pm S.E.M., with (n) representing the number of individual sperm cells tested. Statistical significance (unpaired t-test) was indicated by $***p \leq 0.0005$. Data were collected from 3 human donors, no variations between human donors were noticed (adapted from: Mundt *et al.* (2018) [103]).

These findings corroborate my hypothesis that a novel CatSper-independent cation conductance could provide additional depolarization under physiological conditions. To isolate I_{DSper} , all following experiments were performed in presence of both Mg^{2+} and NNC 55-0396.

3.4 DSper current exhibits temperature sensitivity

Next, I aimed to investigate the mechanism(s) of DSper activation. Previous work has focused on various DSper candidates, one being ATP-activated P2X channels. Navarro *et al.* showed functional expression of P2X2 in mouse spermatozoa [27]. However, human spermatozoa appear to be insensitive to extracellular ATP [87]. De Toni *et al.* suggested that human sperm thermotaxis is mediated by a member of the thermosensitive transient receptor potential vanilloid channel family, TRPV1 [259], and support their claim by immunocytochemistry and Ca^{2+} imaging. By contrast, Kumar *et al.* detected TRPV4 expression in human spermatozoa using immunocytochemistry and Ca^{2+} imaging [260]. To date, several temperature-sensitive ion channels and specific transporters have been reported in mammalian sperm. However, functional characterization of a temperature-activated cation conductance via direct methods, such as electrophysiology, has not yet been performed in human sperm. Given that the functional expression of a thermosensitive TRP ion channel in human spermatozoa is still under debate, and their cation permeability renders many of them DSper candidates, the impact of temperature on DSper activity was investigated. As shown in Figure 3.7, elevating the bath temperature potentiated both inward and outward currents in noncapacitated as

3 Results

well as capacitated human spermatozoa (Fig. 3.7 A, B). A temperature ramp from 23°C to 37°C increased I_{DSper} inward currents by factors of 2.7 ± 0.5 for noncapacitated cells and 2.0 ± 0.2 for capacitated cells, respectively ($Q_{10,noncapacitated}=1.76$, $Q_{10,capacitated}=1.65$ for Cs^+ inward currents). Half-maximal activation was achieved at $T_{1/2} = 34^\circ C$ (noncapacitated) and $T_{1/2} = 31^\circ C$ (capacitated) (Fig. 3.7 C, D). Moreover, the temperature-induced potentiation was a reversible effect for both noncapacitated and capacitated cells (Fig. 3.7 E). I thus conclude that the observed phenomenon is not a temperature-induced loss of the seal or compromised membrane stability, but that DSper is indeed temperature-activated.

3 Results

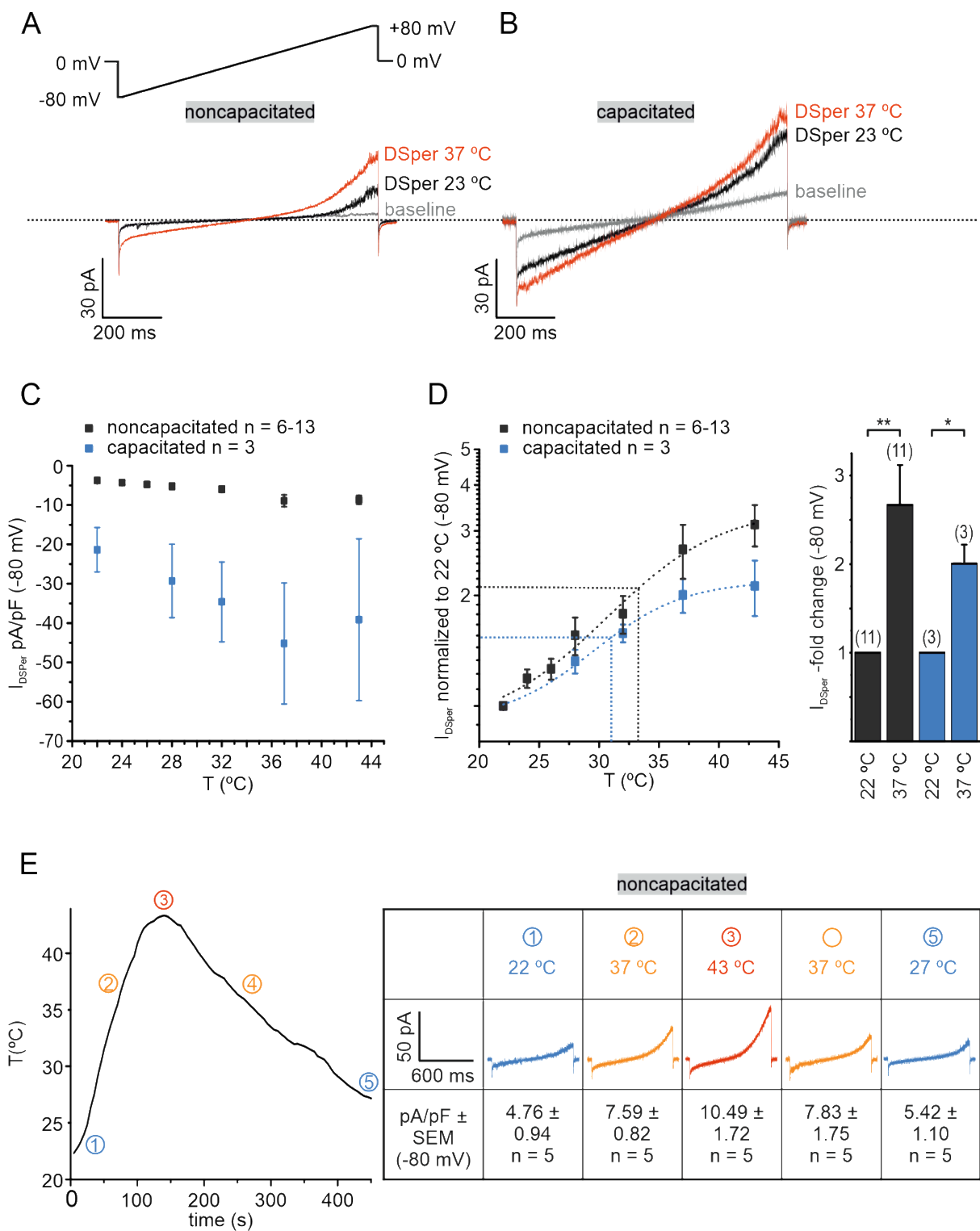


Figure 3.7: Warm temperatures activate DSper. (A–B) Representative current traces of whole-cell patch-clamp recordings from noncapacitated (A) and capacitated (B) human spermatozoa challenged with a rise in temperature from 23°C to 37°C. Both DSper inward- and outward currents are increased at warmer temperatures. (C) Quantified DSper inward current densities as a function of bath temperature (in °C). Noncapacitated (grey squares) and capacitated cells

3 Results

(blue squares) exhibit increased current densities when stimulated with elevated bath temperatures. (D) Data of (C) normalized to room temperature (22°C). Half maximal activation at $T_{1/2} = 34^\circ\text{C}$ (noncapacitated) and $T_{1/2} = 31^\circ\text{C}$ (capacitated) indicated by the dotted lines. The data were fitted with the Boltzmann equation to estimate the temperature at which DSper currents have half-maximal activation. Right panel: statistical significance (unpaired t-test) was indicated by * $p \leq 0.05$, ** $p \leq 0.005$ for capacitated (blue bars) and noncapacitated (black bars) human sperm. (E) The bath temperatures as a function of time and corresponding DSper currents. Inset shows representative traces indicating that the temperature-induced potentiation effect was reversible. Data are mean \pm S.E.M., with (n) representing the number of individual sperm cells tested obtained from three human donors (adapted from: Mundt et al. (2018) [103]).

3.5 DSper conducts sodium ions

Since Na^+ is the major extracellular ion in the female reproductive tract ($[\text{Na}^+] = 140\text{--}150 \text{ mM}$ [261]), Na^+ is a likely source for sperm membrane depolarization. I, therefore, investigated whether DSper is permeable for Na^+ . As indicated in Figure 3.8, similar outward rectifying DSper currents were recorded when extracellular Cs^+ was replaced with equimolar concentrations of Na^+ . DSper inward Na^+ currents were CatSper-independent since NNC 55–0396 had no significant inhibitory effect (Fig. 3.8 B, C). In the presence of both 1 mM Mg^{2+} and 1 μM NNC 55–0396, I_{DSper} was still reversibly activated by warm temperatures with a 4.1 ± 0.5 -fold increase for inward Na^+ currents from 22°C to 37°C, which is notably larger than the temperature-induced potentiation observed for cesium currents (Fig. 3.8 D–F). Half-maximum activation was at $T_{1/2} = 34^\circ\text{C}$, comparable to previously analyzed values for the temperature-activated Cs^+ currents. However, Na^+ conductance via DSper produced a larger $Q_{10,\text{noncapacitated}} = 2.30$. Together, these electrophysiological data indicate that DSper is an unselective cation channel and shares characteristic hallmarks with thermosensitive TRP channels [262]. I thus proceeded to define which TRP channel(s) is involved.

3 Results

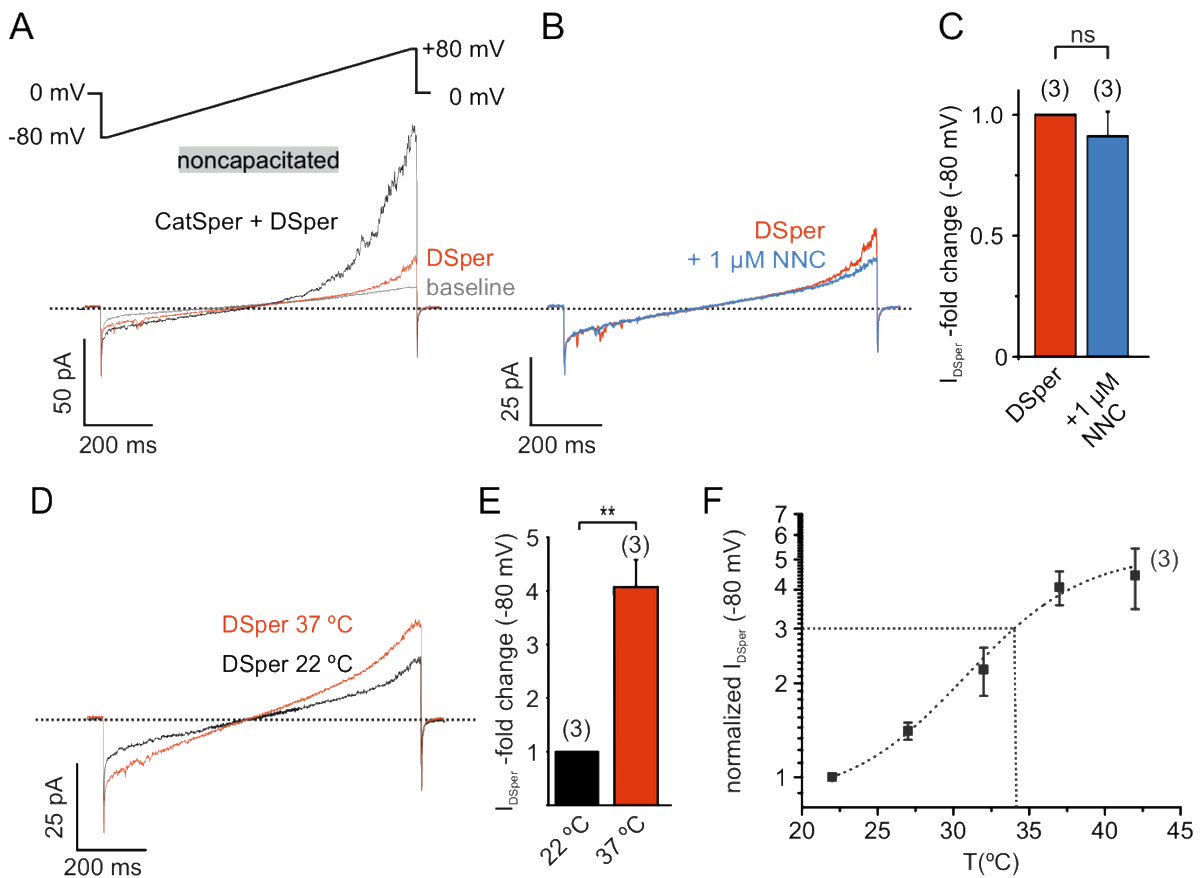


Figure 3.8: DSper conducts sodium ions. (A) Representative current traces from whole-cell patch-clamp recordings of noncapacitated human spermatozoa. Inward and outward currents were elicited with voltage ramps as depicted. To record DSper currents, extracellular Cs^+ was substituted with the same concentration of Na^+ . Representative current traces (B) and quantification of normalized DSper inward currents (C) before and after stimulation with 1 μM NNC suggest that CatSper does not contribute to the recorded sodium inward conductance. (D) Representative current traces of spermatozoa challenged with a rise in temperature from 22°C to 37°C. Both DSper inward- and outward currents are increased at warmer temperatures. Statistical significance in (E) (unpaired t-test) was indicated by ** $p \leq 0.005$. (F) Quantification of inward currents normalized to 22°C at increasing bath temperatures. A similar temperature-induced potentiation effect of DSper Na^+ inward currents was observed for Cs^+ currents. All recordings were performed in the presence of the CatSper inhibitor NNC to exclude any CatSper contribution. Half maximal activation was achieved at $T_{1/2\text{ sodium}} = 34^\circ\text{C}$ (dotted line). The data were fitted with the Boltzmann equation. Statistical significance (unpaired t-test) is indicated by ** $p \leq 0.005$. Data are mean \pm S.E.M., with (n) representing the number of individual sperm cells tested (adapted from: Mundt et al. (2018) [103]).

3 Results

3.6 The cation channel TRPV4 represents DSper

Considering the temperature spectrum I observed for I_{DSper} activation (Fig. 3.7 and 3.8), candidate channels could be TRPV3, TRPM3, or TRPV4 [262]–[266]. TRPV2 contribution was ruled out since TRPV2 has an unusually high activation threshold of 53°C [267]. In addition, TRPV1 was previously proposed as a mediator of human sperm thermotaxis [259]. To discriminate between candidates, potential effects of isoform-selective agonists were tested – carvacrol for TRPV3 [268], RN1747 for TRPV4 [269], capsaicin for TRPV1 [270], and pregnenolone sulfate for TRPM3 [271]. No effects were observed by 1 μ M or 10 μ M capsaicin ($EC_{50} = 711.9$ nM [270]) (Fig. 3.9 A, B). In order to confirm the functional absence of TRPV1, the capsaicin experiment was repeated with 30 μ M intracellular phosphatidylinositol-4,5-bisphosphate (PIP₂), as depletion of PIP₂ in whole-cell configuration might impair TRPV1 sensitivity to capsaicin [272], [273]. However, no changes in DSper inward and outward currents were observed. Using Ca^{2+} imaging of fluo-4/AM-loaded sperm, I next recorded fluorescence changes in the flagellar principle piece while stimulating human sperm with either 10 μ M capsaicin or 500 μ M carvacrol (Fig. 3.9 C). Neither the TRPV1 nor the TRPV3 agonist elicited any rise in cytosolic calcium levels. Thus, human spermatozoa do not express functional TRPV1 or TRPV3 channels. TRPM3 channels also exhibit temperature sensitivity between ambient warm to hot, which resembles the temperature range I observed for DSper [274]. Therefore, a possible contribution of TRPM3 in I_{DSper} generation was investigated by application of the TRPM3 agonist pregnenolone sulfate (PS) [271] (Fig. 3.9 A, B). 10 μ M PS did not result in any change of the basal DSper current, confirming the absence of functional TRPM3 in human spermatozoa.

3 Results

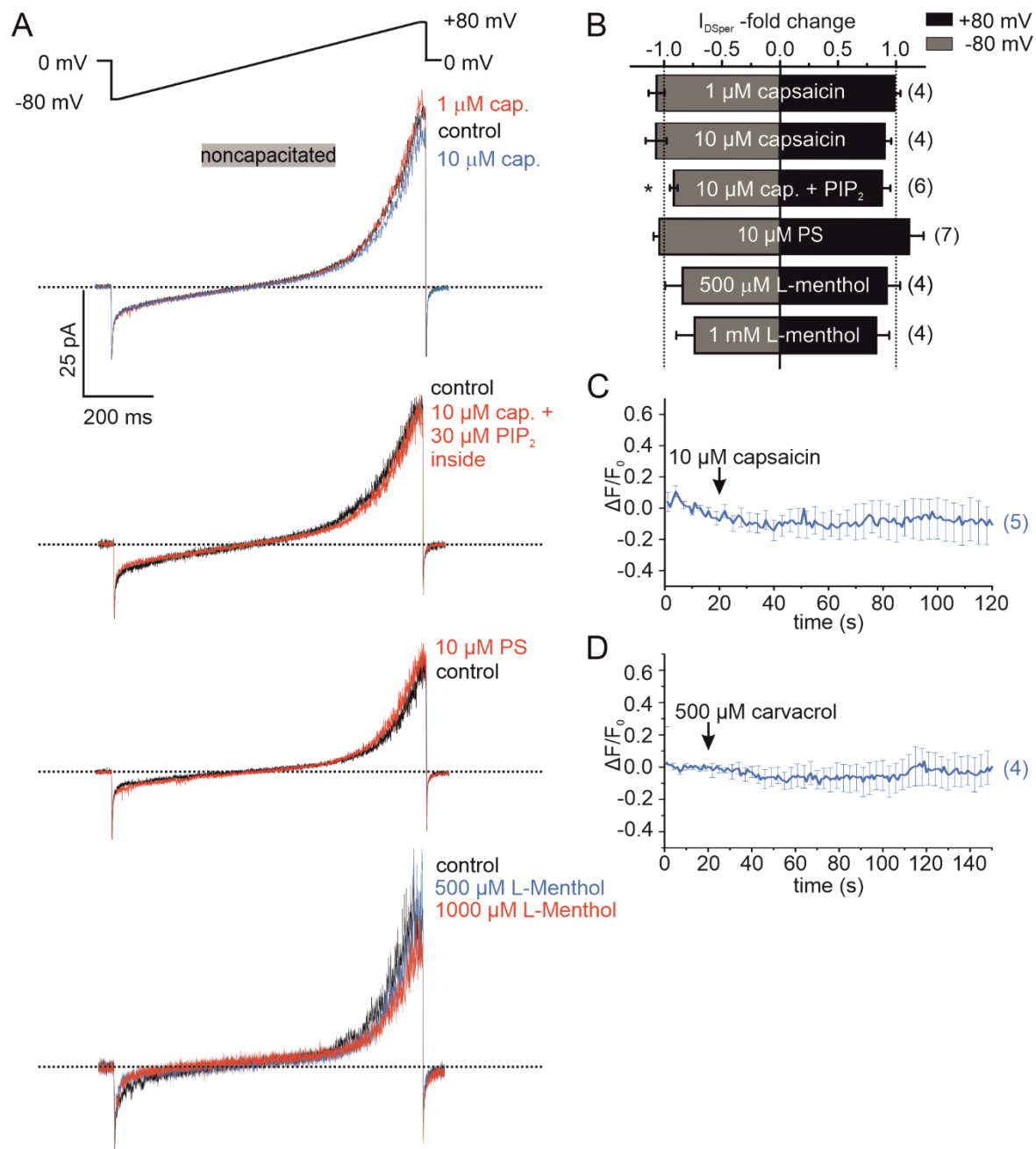


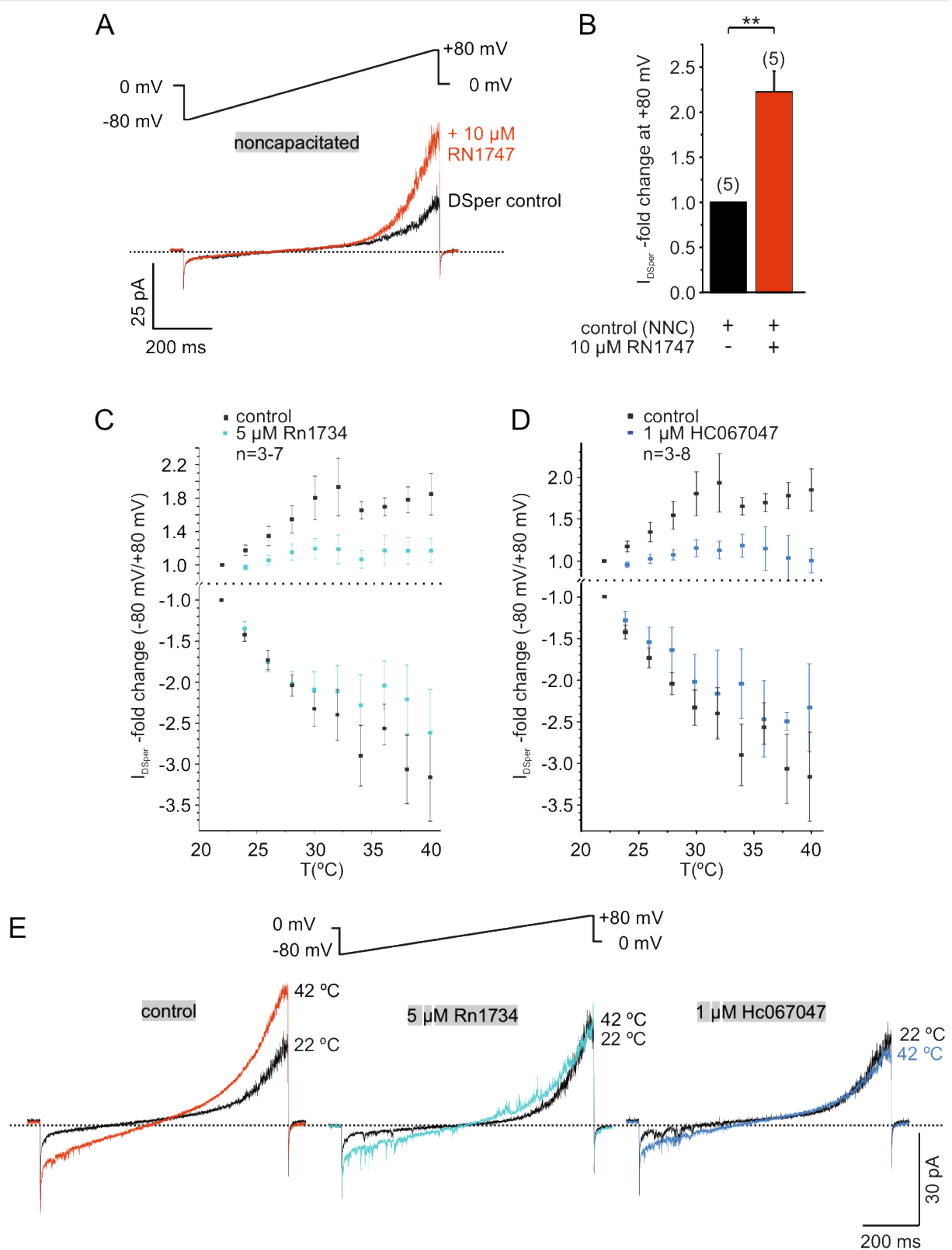
Figure 3.9: TRPV1, TRPV3, TRPM3, and TRPM8 are not functionally expressed in human spermatozoa. (A) Original current traces from representative whole-cell patch-clamp recordings of noncapacitated human spermatozoa. Inward- and outward currents were elicited with voltage ramps as depicted. Black traces indicate DSper currents under control conditions, red/blue traces show absent potentiation by various TRP-agonists tested. These are Capsaicin (Cap., TRPV1), pregnenolone sulfate (PS, TRPM3), L-menthol (TRPM8). Quantification of

3 Results

normalized DSper currents for all conditions is depicted (B). (C) Single-cell Ca^{2+} imaging confirmed the absence of functional TRPV1 in human spermatozoa. Application of 10 μM capsaicin did not affect cytosolic Ca^{2+} levels. (D) The single-cell Ca^{2+} imaging approach did not reveal any notable effect of the TRPV3 specific agonist carvacrol (500 μM). Data are mean \pm S.E.M., with (n) representing the number of individual sperm cells tested obtained from 4 donors. Statistical significance (Student's t-test) is indicated by * $p\leq 0.05$ (adapted from: Mundt et al. (2018) [103]).

In electrophysiological recordings, only the TRPV4 agonist RN1747 elicited a significant effect. In detail, application of 10 μM RN1747 ($\text{EC}_{50} = 0.77 \mu\text{M}$ [269]) significantly potentiated DSper outward currents (Fig. 3.10 A, B) in noncapacitated human spermatozoa. Interestingly, additional pharmacological investigation of DSper revealed that both TRPV4-specific antagonists, HC067047 and RN1734 [269], [275], prevented temperature activation of DSper, confirming that DSper pharmacology matches TRPV4 (Fig. 3.10 C, E). Interestingly, we found biphasic inhibition of DSper, that does not result in a complete current block, particularly in the temperate range between 24 °C and 32°C. Since both inhibitors are dissolved in ethanol, a vehicle control was performed to exclude any inhibitory effect of ethanol on temperature sensitivity. Indeed, the same vehicle concentration (0.1% ethanol) failed to inhibit DSper temperature activation and yielded comparable results to control conditions (Fig. 3.11). All pharmacological experiments were recorded in the presence of Mg^{2+} and NNC to exclude off-target effects on CatSper by the respective compound.

3 Results



3 Results

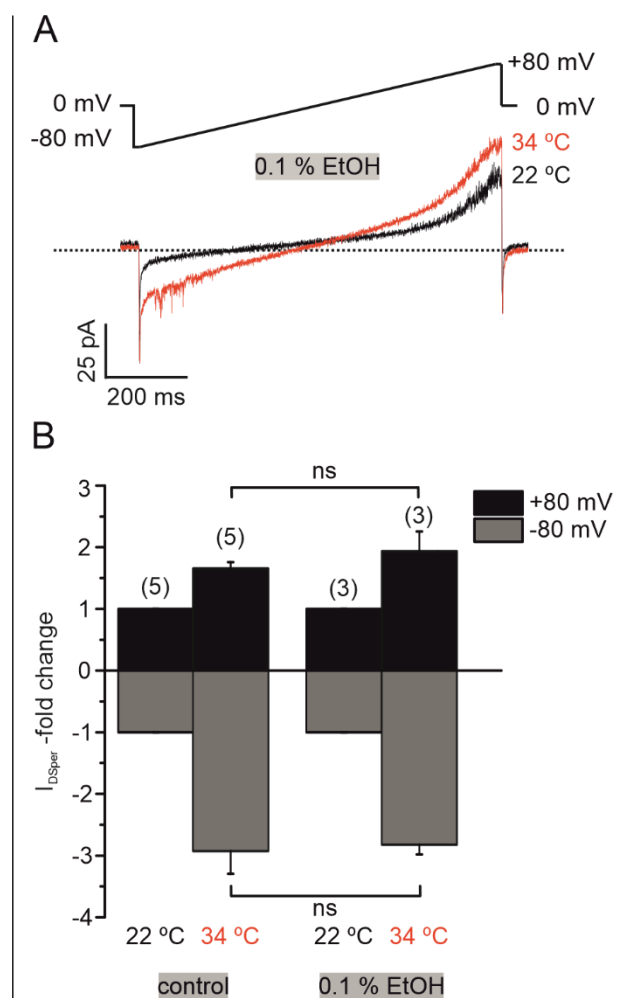
Figure 3.10: DSper pharmacology resembles TRPV4. (A) Representative whole-cell patch-clamp recordings of noncapacitated human spermatozoa. Inward- and outward currents were elicited with voltage ramps. DSper monovalent caesium currents (black trace) are increased after stimulation with 10 μ M RN1747, a TRPV4 agonist (red trace). Both recordings were performed in the presence of 1 μ M NNC. (B) Quantification of normalized DSper outward currents under control conditions and after stimulation with RN1747. A significant increase upon stimulation with the TRPV4 agonist (factor 2.22 ± 0.23 , ** $p=0.0007$, unpaired t-test, $n = 6$) is observable. No variation between human donors was noticed. (C-E) TRPV4 inhibitors RN1734 and HC067047 antagonize human DSper activity. Quantification of normalized DSper inward ($V_{hold} = -80$ mV) and outward ($V_{hold} = +80$ mV) currents as a function of bath temperature (in $^{\circ}$ C). Grey squares show control conditions, turquoise (C)/blue (D) squares indicate the presence of the respective TRPV4 antagonist. Representative current traces of whole-cell voltage clamp recordings from noncapacitated spermatozoa for all three conditions are depicted in (E). Representative current traces indicate that a rise in temperature from 22 $^{\circ}$ C to 42 $^{\circ}$ C considerably potentiates DSper inward and outward currents under control conditions but not in the presence of the TRPV4 antagonists HC067047 or RN1734. Data are depicted as Mean \pm SEM, the number of cells as indicated (adapted from: Mundt et al. (2018) [103]).

The biphasic inhibition of DSper with TRPV4-selective antagonists suggests an additional non-TRPV4 conductance that is active at temperatures $<32^{\circ}$ C. I thus sought to investigate a potential contribution of the cold-receptor TRPM8 and tested methanol as a selective TRPM8 activator [276]. In electrophysiological recordings, stimulation with either 500 μ M or 1 mM L-Menthol did not potentiate I_{DSper} but instead resulted in slight inhibition, largely ruling out functional expression of TRPM8 in human spermatozoa (Fig. 3.9 A, B).

Another potential candidate for initial temperature activation is TRPP3 with a reported temperature sensitivity between 20 $^{\circ}$ C and 32 $^{\circ}$ C [266]. Phenamil is a selective TRPP3 antagonist and preliminary results suggest effective inhibition of I_{DSper} temperature activation when phenamil is applied during electrophysiological recordings (Fig. 3.12). Inhibition is most prominent between 22 $^{\circ}$ C and 32 $^{\circ}$ C (Fig. 3.12 B), which covers the subeffective range of the previously tested TRPV4 inhibitors.

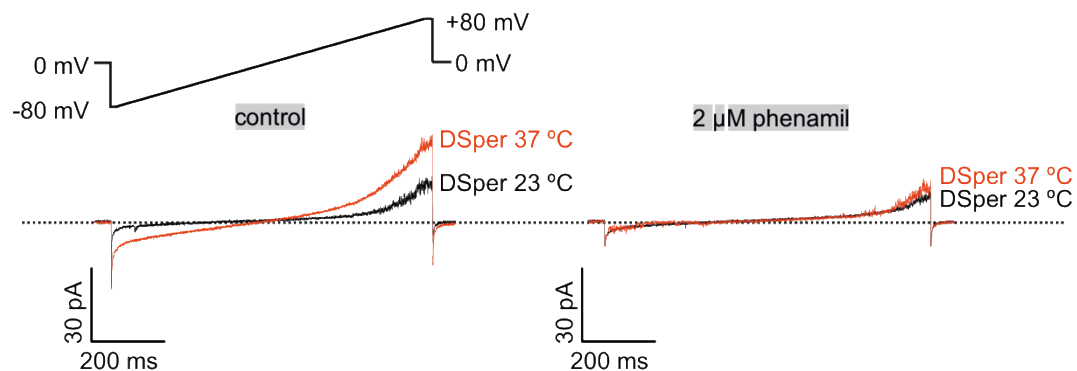
3 Results

Figure 3.11: Ethanol does not affect DSper temperature activation. (A) Original current traces from representative whole-cell patch-clamp recordings of non-capacitated human spermatozoa exposed to 22 and 34°C and an extracellular ethanol (EtOH) concentration of 0.1% as vehicle control. A temperature rise potentiated DSper inward- and outward currents similar to control conditions, indicating no effect by 0.1% EtOH as the solvent. (B) indicates the absence of inhibition by 0.1% extracellular EtOH as quantified normalized DSper inward and outward currents at 22 and 34°C, respectively (adapted from: Mundt et al. (2018) [103]).



3 Results

A



B

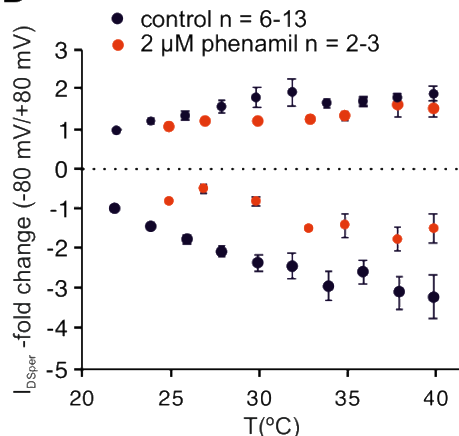


Figure 3.12: Putative TRPP3 contribution to I_{DSper} .
(A) Representative current traces of whole-cell patch-clamp recordings from non-capacitated human spermatozoa challenged with a rise in temperature from 23°C to 37°C. $DSper$ inward- and outward currents are increased at warmer temperatures under control conditions (left), but not in the presence of 2 μ M phenamil, a TRPP3 antagonist (right). **(B)** Quantification of normalized $DSper$ inward ($V_{hold} = -80$ mV) and outward ($V_{hold} = +80$ mV) currents as a function of bath temperature (in °C). Black points show control conditions, red points indicate the presence of 2 μ M phenamil. The TRPP3 inhibitor antagonizes human $DSper$ temperature activation. Data is depicted as Mean \pm SEM, number of cells as indicated.

In summary, my results indicate that the temperature-activated cation channel TRPV4 is functionally expressed and provides membrane depolarization at physiological temperatures in human sperm. An additional non-TRPV4 conductance might carry out low-temperature sensitivity, potentially mediated by TRPP3.

3.7 TRPV4 is detectable on mRNA and protein level

Supporting my functional data, TRPV4 was detected in human sperm on both mRNA and protein levels. Reverse transcriptase PCR performed with mRNA isolated from "swim-up"

3 Results

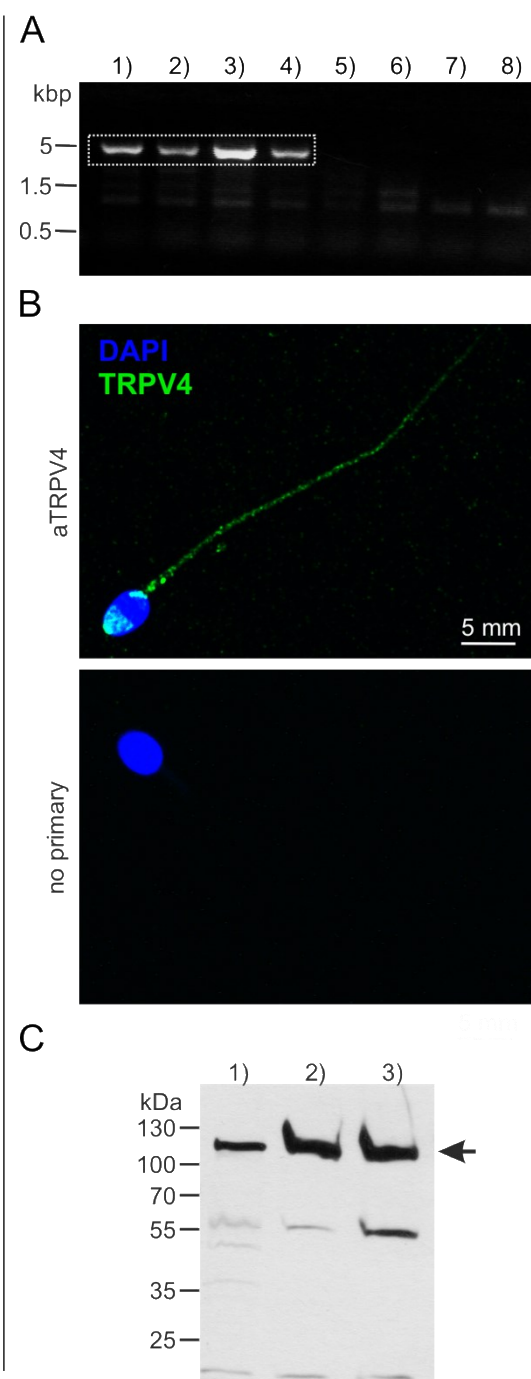
purified spermatozoa, followed by amplification of full-length TRPV4 (Fig. 3.13 A), produced a band of the expected size. The band was absent in negative controls, to which no reverse transcriptase or no cDNA template were added. Sequencing of the isolated PCR product of that particular band (dotted square) yielded the full-length sequence of TRPV4 isoform A (2620 bp, 98 kDa, Q9ERZ8). Immunostaining with anti-TRPV4 specific antibodies (Fig. 3.13 B) yielded an immunopositive signal in the acosome and flagellum. Moreover, the presence of TRPV4 protein was confirmed by western blotting (Fig. 3.13 C). In extracts from human testicular tissue (1), capacitated (2), and noncapacitated (3) spermatozoa I detected immunoreactive bands at ~115 kDa.

3.8 Sperm TRPV4 assembles into a functional channel

Finally, when TRPV4 was cloned from human sperm mRNA extracts and recombinantly expressed in HEK293 cells (Fig. 3.14 A, B), I detected a band of similar molecular weight by western blotting. A faint band of equal size is also visible in non-transfected and empty-vector transfected cells, indicating endogenous expression of TRPV4 in HEK293 cells. This observation is supported by relatively small current densities in nontransfected cells at room temperature, as compared to cells that overexpress sperm TRPV4 (Fig. 3.14 C). Moreover, the cloned TRPV4 recapitulates DSper temperature sensitivity (Fig. 3.14 D, E), as well as activation by the selective TRPV4 agonist RN1747 (Fig. 3.14 F, G), indicating that TRPV4 cloned from human sperm cells indeed assembles into a functional channel.

3 Results

Figure 3.13: TRPV4 can be detected on protein and mRNA levels. (A) RT-PCR using a full-length TRPV4 primer pair. cDNA was obtained from swim-up purified noncapacitated human spermatozoa and PCR conditions were as follows: 1)–4) varying annealing temperatures (52–60°C), 5)–6) negative control in the absence of the reverse transcriptase enzyme ($T_a = 50, 56^\circ\text{C}$), 7)–8) no template control ($T_a = 56^\circ\text{C}$ & 60°C). The dotted square marks bands that were selected for gene product sequencing. (B) Confocal fluorescence image of anti-TRPV4 (green) immunoreaction in isolated human spermatozoa. Nuclear counterstaining was performed with DAPI (blue). Immunopositive fluorescent signals were detected in the sperm flagellum and the acrosome region (top). The secondary antibody's specificity was confirmed by immunostaining in the absence of the primary antibody (negative control, bottom). (C) Western blotting confirms the presence of TRPV4 protein in (1) human testicular tissue, (2) capacitated, and (3) noncapacitated human spermatozoa. Immunopositive bands are detected in all samples at approximately 115 kDa (adapted from: Mundt et al. (2018) [103]).



3 Results

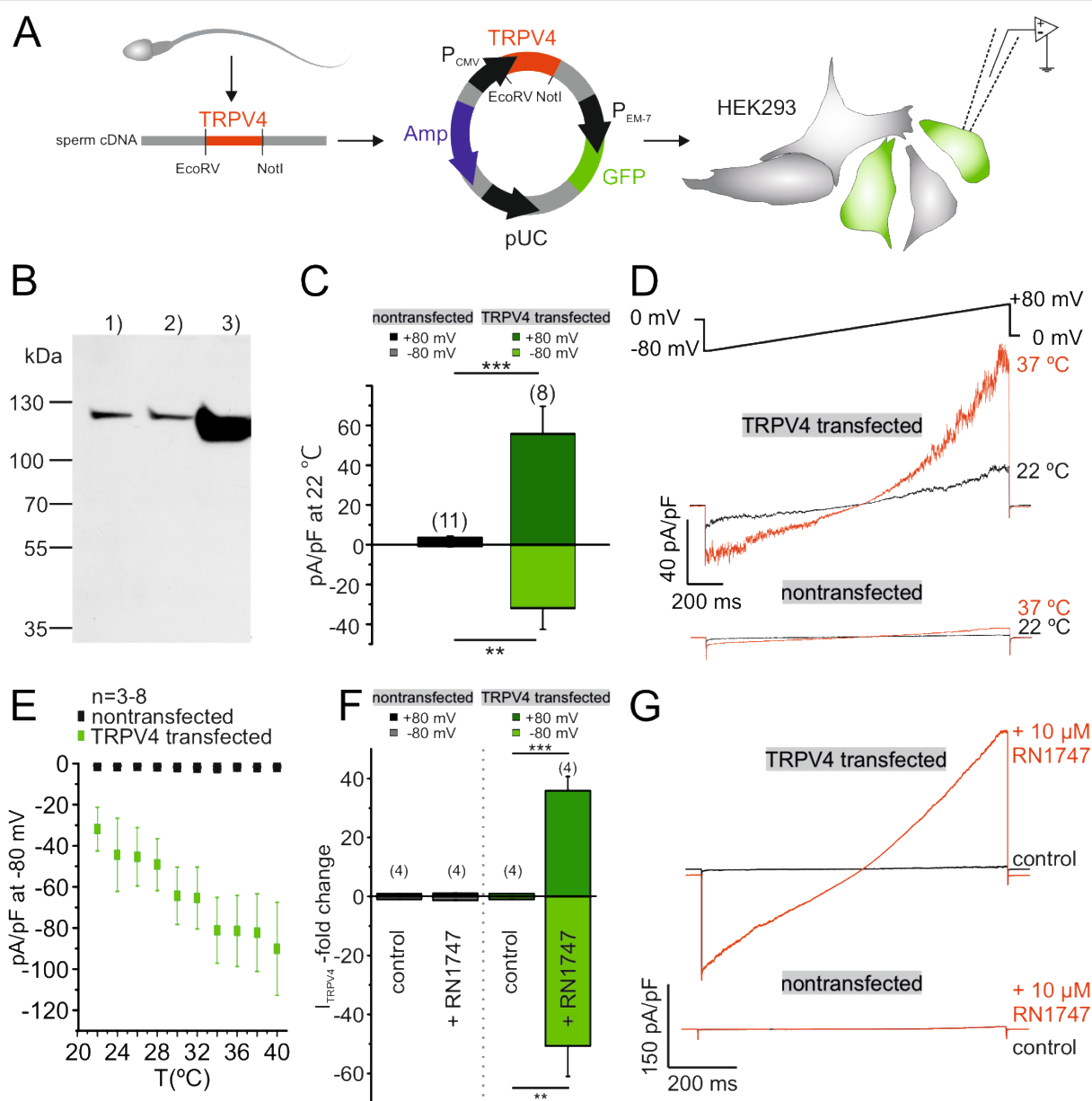


Figure 3.14: Recombinantly expressed sperm TRPV4 assembles into a functional channel in HEK293 cells. (A) Schematic representation of the experimental approach: Full-length TRPV4 (isoform A) was cloned from human sperm mRNA extracts and recombinantly expressed in HEK293 cells, utilizing a pTracer CMV vector (Fig. 2.1). The GFP containing bicistronic vector allowed the identification of green fluorescent transfected cells. (B) Western blot results are depicted for (1) nontransfected HEK293 cells, (2) cells transfected with the empty vector, and (3) HEK293 cells transfected with the TRPV4-containing vector. An intense immunopositive band can be detected in line 3) at approx. 115 kDa. Weak bands in 1) and 2) suggest endogenous expression of TRPV4 in HEK293 cells. (C) Electrophysiological characterization reveals a significant increase in the basic activity of TRPV4 transfected cells (at room temperature, 22°C). Inward and outward current densities were recorded as described before (ramp recordings -80 to +80 mV). Statistical significance (unpaired t-test) is indicated by: ** $p\leq 0.005$, *** $p\leq 0.0005$. (D) Representative current recordings show inward and outward currents of nontransfected vs.

3 Results

*TRPV4 transfected cells affected by an increasing bath temperature (22°C & 37°C). (E) Quantification of (D) suggests temperature-induced potentiation of inward and outward currents in TRPV4 transfected cells as observed for I_{Dper} in human spermatozoa. (F) Normalization of both inward and outward currents to control conditions for transfected and nontransfected HEK cells upon stimulation with RN1747. Potentiation is statistically significant for transfected cells (** $p\leq 0.005$, *** $p\leq 0.0005$). (G) Whole-cell voltage clamp recordings reveal a strong potentiation of inward and outward currents upon stimulation with the TRPV4 agonist RN1747 in TRPV4- transfected but not in nontransfected HEK293 cells. Inward and outward currents were elicited via voltage ramps as depicted above. Data are presented as Mean \pm SEM, the number of recorded cells as indicated (adapted from: Mundt et al. (2018) [103]).*

Project C: Establishing an optogenetic stimulation paradigm in the murine olfactory bulb

The aim of this subproject is to establish a tool that mimics peripheral sensory input into the olfactory bulb harnessing the spatiotemporal definition of optogenetics. This could be a powerful approach to understand information processing at different processing levels of the MOB and, in particular, the AOB. This study will focus primarily on establishment of a suitable stimulation protocol in the AOB, while comparative MOB data will supplement the results where necessary.

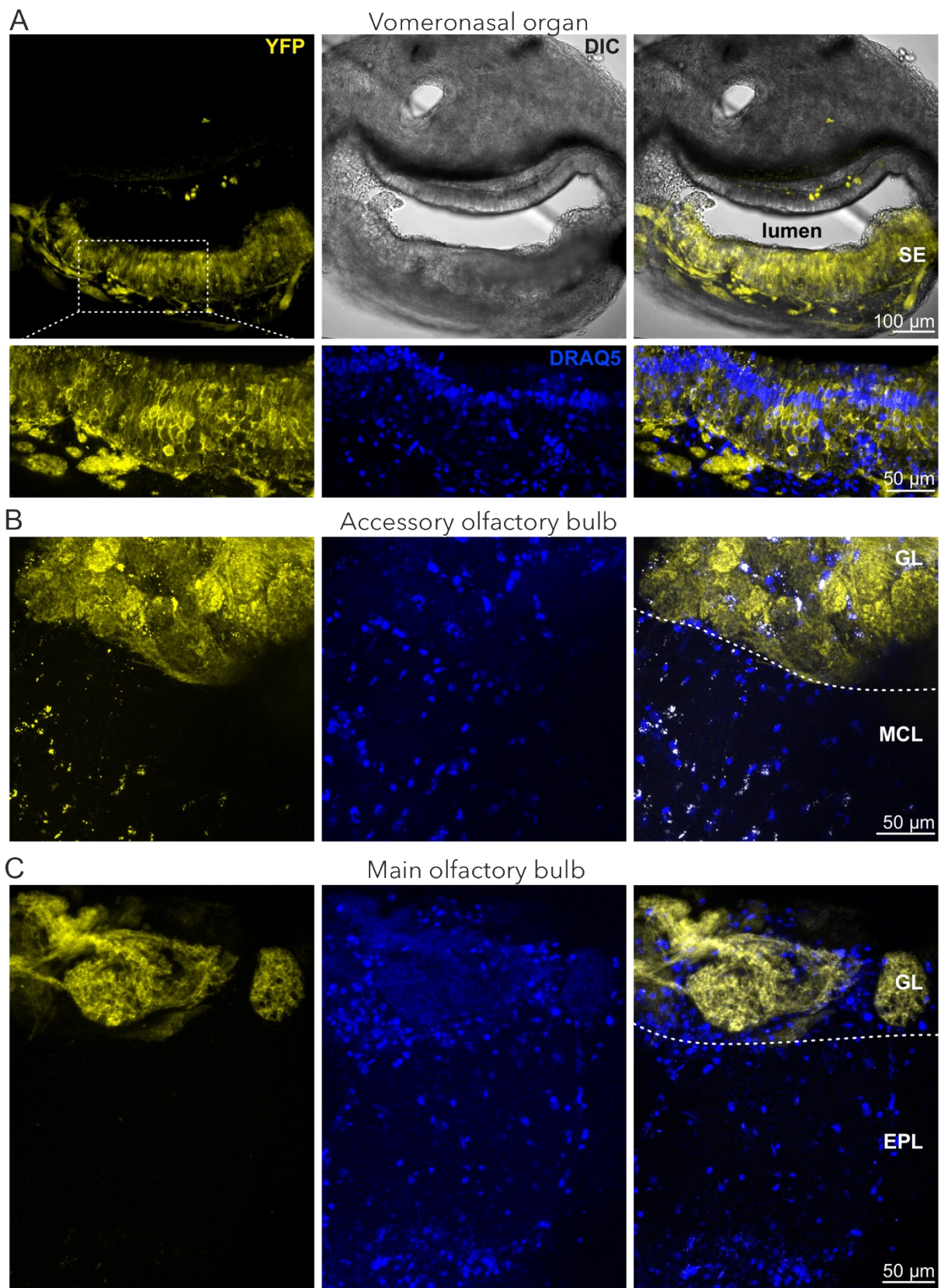
3.9 OMP-ChR2-YFP mouse line expresses light-activatable channelrhodopsin in peripheral OSNs and VSNs

Peripheral VSNs form synaptic connections with AMCs in the glomerular layer of the AOB. To activate the presynaptic fraction of a single glomerulus, we used the OMP-ChR2-YFP (JAX #014173) mouse line, which has been generated by the Bozza laboratory (Northwestern University) and deployed in several publications [277]–[279]. These mice express a ChR2(H134R)-EYFP fusion gene from the olfactory marker protein locus (*Omp*). The knock-in is expressed in all mature OSNs and VSNs, rendering them light-sensitive. Histological investigation of our particular mice verified expression of ChR2-YFP fusion protein in the VNO sensory epithelium and the glomerular layers of AOB and MOB (Fig. 3.15).

3 Results

We aim to understand the functional implications of AMC oscillations and improve our general understanding of pheromone identity processing within the AOB by mimicking sensory input and simultaneously recording AMC responses. To do so, we will perform electrophysiological recordings of single mitral cells and trace dendritic targets within the glomerular layer. Target regions will then be stimulated with a spatiotemporally defined 473 nm laser pulse. We hypothesize that laser stimulation will trigger axonal depolarization via ChR2, the generation of presynaptic action potential(s) (APs), and eventually presynaptic glutamate release from VSN axon terminals within the stimulated glomerulus. Excitatory input should then be detectable as excitatory postsynaptic currents / potentials in the connected AMC (Fig. 3.16).

3 Results



3 Results

Figure 3.15: ChR2-YFP expression in mature chemosensory neurons of the olfactory system. (A) Acute VNO slice from an adult OMP-ChR2-YFP mouse indicates ChR2-YFP (yellow) expression in VSNs located in the sensory epithelium (SE). The bottom inset represents a higher magnification view of the sensory epithelium, nuclear counterstaining with DRAQ5 (blue). Note that YFP fluorescence is absent in sustentacular cells and other non-sensory tissues of the VNO. (B-C) ChR2-YFP expression is localized to VSN and OSN axon terminals residing within the glomerular layer (GL) of acute AOB (B) and MOB slices (C), respectively. MCL: Mitral cell layer, EPL: External plexiform layer

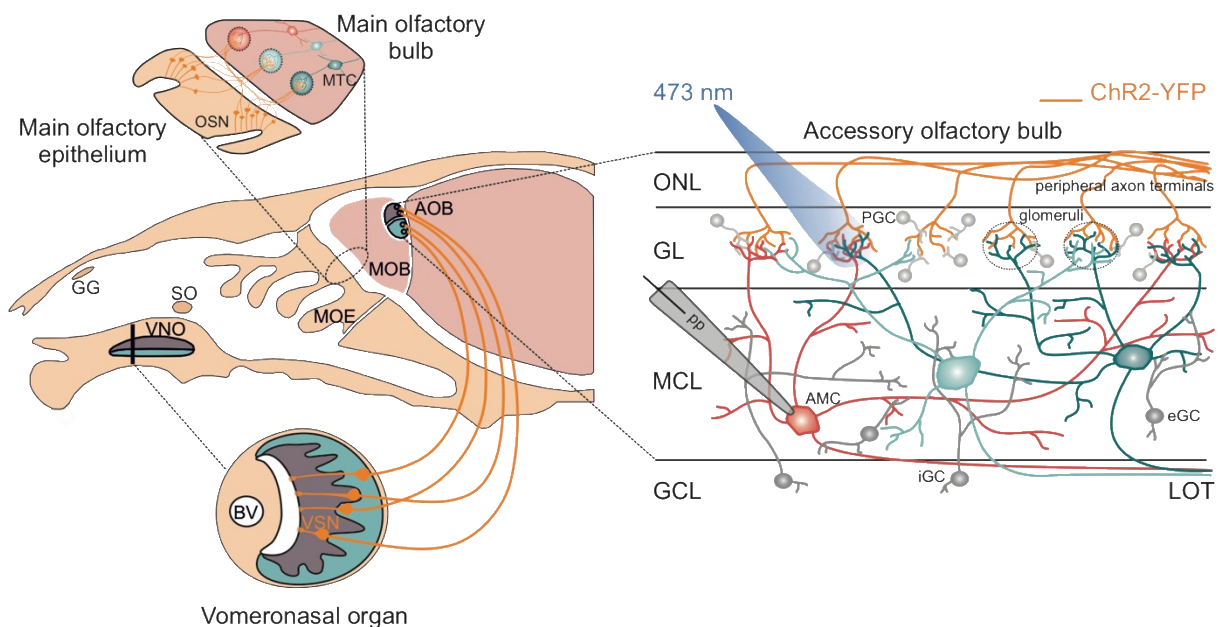


Figure 3.16: Experimental approach. Left: Simplified schematic illustration of the rodent nose indicating ChR2-YFP expression in mature VSNs as well as OSNs (orange). **Right:** Schematic organization of the mouse AOB with incoming ChR2-YFP positive VSN axon terminals in the olfactory nerve layer (ONL). Vomeronasal input is transmitted via synaptic connections to AMCs formed within the glomerular layer (GL). Spatiotemporally defined laser pulses of 473 nm can locally activate ChR2 and potentially trigger presynaptic glutamate release. MCL: Mitral cell layer, pp: Patch pipette, GCL: Granule cell layer, iGC/eGC: internal/external granule cell, PGG: Periglomerular cell, LOT: Lateral olfactory tract. (Adapted and modified from Spehr et al., (2006) and Mohrhardt et al., (2018))

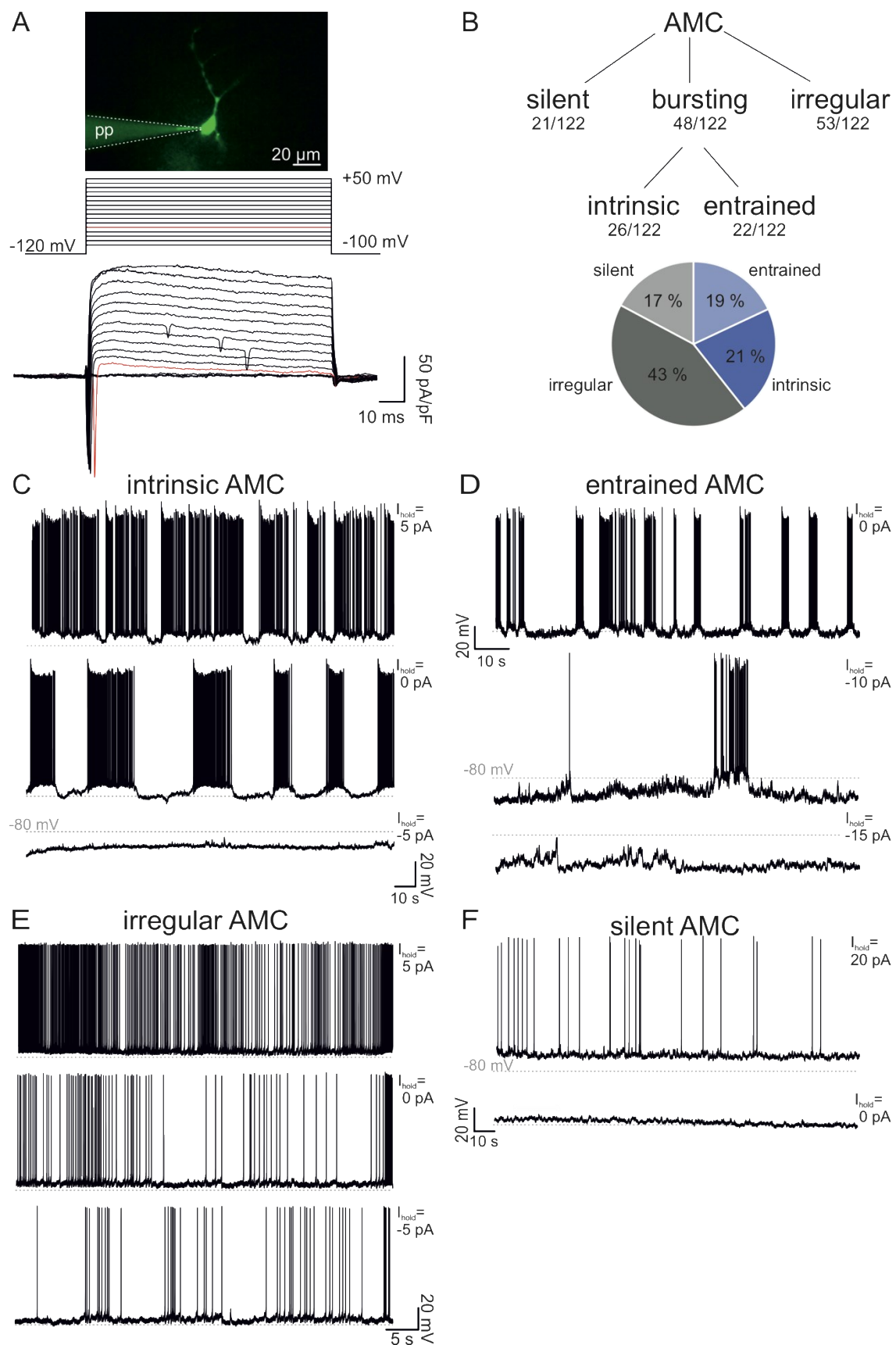
3 Results

3.10 AMC electrophysiology

To investigate sensory input processing in AMCs, it is crucial to understand and distinguish the spontaneous activity profile of this cell population. AMC spontaneous activity is heterogeneous and can either be irregular, nonexistent (silent), or organized in rhythmic infra-slow oscillatory burst activity [213]–[215].

First, I asked whether I can reproduce previous work of our laboratory and others [213]–[215] by performing AMC whole-cell current clamp recordings. I recorded spontaneous activity from individual AMCs in acute parasagittal sections of the mouse olfactory bulb (Fig. 3.17) and found neurons to either fire rhythmically with alternating periods of activity and silence (40 %, Fig. 3.17 B–D), or fire APs irregularly with no apparent periodicity (43 %, Fig. 3.17 B, E). Some cells remained essentially silent at resting potential (V_{rest}) but were able to generate APs upon depolarizing current injection (17 %, Fig. 3.17 B, F). A subpopulation of bursting cells was driven by network input, as hyperpolarizing current injections did not abolish subthreshold baseline oscillations (entrained AMCs, Fig. 3.17 D). By contrast, some bursting cells were silenced upon hyperpolarizing current injection, indicating an intrinsic capability of burst generation and independence from network input (intrinsic AMCs, Fig. 3.17 C). I thus conclude that my AMC population recordings reproduce previous findings by displaying the described AMC spontaneous activity profile. I will next proceed to investigate the effect of presynaptic input.

3 Results



3 Results

Figure 3.17: Spontaneous activity of AOB mitral cells in vitro. (A) top: Widefield fluorescent image of a patched AMC in whole-cell configuration. After the patch pipette (pp) targets an individual cell, the membrane patch is ruptured for electrical access, allowing cytosolic perfusion with a fluorescent dye. Middle: For initial assessment of recording quality, voltage-clamp step protocols (V_{hold} : -120 mV, steps -100 mV to +50 mV, 10 mV increments) are performed. Bottom: Representative current traces of transient voltage-gated Na^+ inward currents followed by voltage-gated K^+ outward currents activated by the described step protocol. (B) Classification of recorded AMCs according to their spontaneous activity profile. Neurons were classified at resting potential (V_{rest} , $I_{pip}=0$ pA) and the effects of hyperpolarizing and depolarizing current injections were analyzed. AMCs were either silent ($n=21/122$) at V_{rest} or they fired action potentials in an irregular, nonperiodic fashion ($n=53/122$), or with alternating periods of active and silent (bursting, $n=48/122$). Based on their dependence on network input, bursting AMCs were further subdivided into intrinsically oscillating ($n=26/122$) and entrained ($n=22/122$) AMCs. (C-D) Example whole-cell current clamp recordings of an intrinsically bursting (C) and entrained (D) AMC. At V_{rest} both neurons show activity bursts with oscillating baseline potential that results in alternating phases of active and silent. Intrinsic cells become silent upon hyperpolarizing current injection, while entrained cells display subthreshold oscillations, driven by an unknown network source. Note that the inter-burst-interval of intrinsic AMCs decreases with depolarizing current injection. (E) Representative voltage trace of an irregularly firing AMC. The AP frequency is dependent on membrane potential and thus the injected current I_{pip} . (F) Example of a silent AMC that is inactive at V_{rest} but capable of generating APs when stimulated with depolarizing current.

3.11: Optogenetic activation of OSN, but not VSN, axon terminals triggers mitral cell excitation

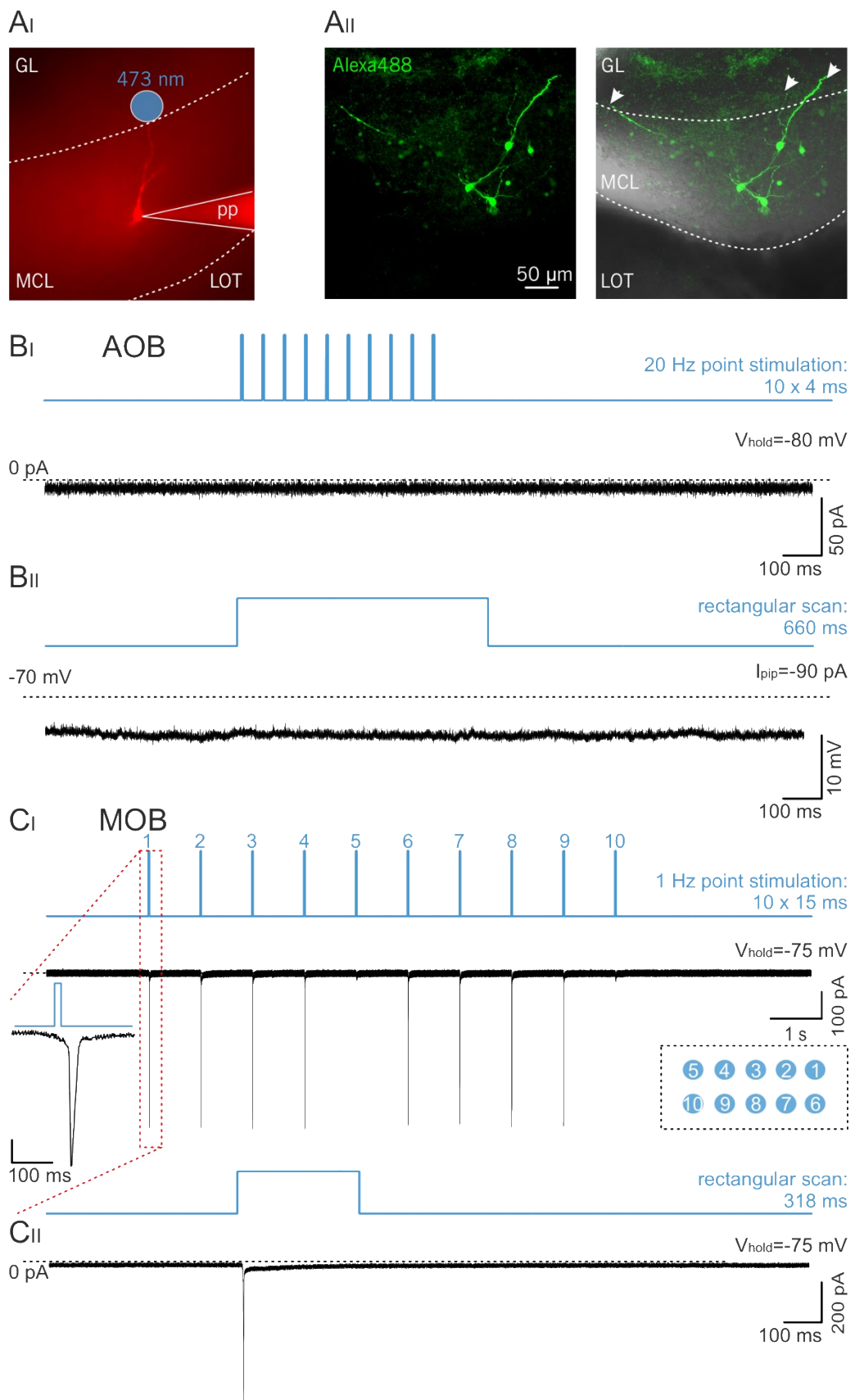
After initial AMC characterization and simultaneous cytosolic diffusion of a fluorescent dye, dendritic branches were traced and glomerular targets were identified. Since widefield fluorescence imaging has only a limited signal-to-noise ratio, *post-hoc* morphological biocytin-streptavidin reconstructions with a confocal laser-scanning microscope were performed to confirm the presence of dendritic projections into the GL (Fig. 3.18 A). Next, presynaptic VSN axon terminals within the dendritic target region were illuminated within defined stimulation areas. Here two different stimulation modes were applied (methods). During spherical illumination, the laser beam was scattered to cover a spherical area of varying size and positions ("point stimulation"). In rectangular scanning mode, the laser scanned the entire GL to stimulate the maximum amount of VSN axon terminals. For both stimulation modes, none of the recorded AMCs received any light-induced excitatory input (Fig. 3.18 B). This negative

3 Results

result remained unaltered irrespective of exposure time, laser strength or scanning speed / inter-stimulus interval.

In contrast, I could activate MOB mitral cells by both stimulation paradigms (Fig. 3.18 C). When OSN axon terminals were stimulated with a 1 Hz point stimulation of 15 ms each, the recorded mitral cell responded with a 15 ms delayed transient inward current, indicative of the voltage-gated Na^+ current during an AP. The 15 ms delay is expected and indicative of synaptic transmission. Interestingly, this response was dependent on the position of point stimulation, as stimulation areas distant from the dendritic target region did not elicit the described response (Fig. 3.18 C_I). When the rectangular scanning mode was deployed, an AP was generated during the start of the scanning process, aligning with the point stimulation positions 1 & 6 that elicited a response (Fig. 3.18 C_{II}, scanning direction right to left). I thus conclude, that the optogenetic stimulation paradigm is functional in the MOB, but physiological differences between VSNs and OSNs render this method unsuitable for the AOB.

3 Results



3 Results

Figure 3.18: Optogenetic stimulation paradigm in the murine olfactory bulb. (A_I) Widefield fluorescent image of a patched and ATTO633 diffused AMC with dendritic projections to the GL of the AOB. The blue circle indicates spherical point stimulation of the dendritic ending with a 473 nm diode laser. pp=patch pipette (A_{II}) Biocytin-streptavidin-Alexa488 reconstruction of 3 patched AMCs in a confocal z-stack. Arrowheads indicate dendritic targets within the GL of the AOB. GL=glomerular layer, MCL = mitral cell layer, LOT = lateral olfactory tract (B) Representative recordings of AMCs patched in voltage-clamp (B_I) or current-clamp mode (B_{II}). Optogenetic stimulation of VSN axon terminals via point stimulation (B_I) or rectangular scanning across the GL (B_{II}) did not elicit postsynaptic responses in the connected AMCs. Cells were slightly hyperpolarized to avoid spontaneous firing during the stimulation period. (B_I) is an average of 4 trials, (B_{II}) is the averaged trace of 6 trials. (C) Representative voltage-clamp recordings of a MOB mitral cell during optogenetic targeting of presynaptic OSN axon terminals. (C_I) 1 Hz point stimulation at varying positions elicits a transient inward current in the connected mitral cell (1,2,3,4,6,7,8,9). Stimulation areas distant from the dendritic target region (5 & 10) fail to trigger mitral cell excitation. Red inset shows the transient inward current at higher magnification and suggests the generation of an action potential with approx. 15 ms delay. (C_{II}) Rectangular scan of the entire GL while recording the same MOB mitral cell as shown in (C_I). The scanning direction is from right to left and, thus, the start of the scanning process aligns with positions 1 & 6 of (C_I). A comparable transient inward current is elicited at the beginning of the scan.

One possible cause for the absent AMC excitation could be a low ChR2-YFP protein density in VSNs, resulting in insufficient depolarization for the initiation of a presynaptic AP. To test this hypothesis, I bypassed channelrhodopsin activation by positioning a bipolar stimulation electrode in the GL of the AOB (Fig. 3.19 A). This stimulation method elicits broad glomerular depolarization. Strong stimulation resulted in direct AMC depolarization and, thus, the instantaneous initiation of an AP in the recorded AMC. To confine electrical stimulation to the GL, I determined the stimulation threshold for each recording that was just below AMC AP initiation. Again, none of the recorded AMCs received any stimulation-induced input besides the stimulation artifact (Fig. 3.19 B). I therefore conclude, that VSN axon terminals in this preparation are incapable of generating APs that eventually lead to glutamate release from the presynapse.

3 Results

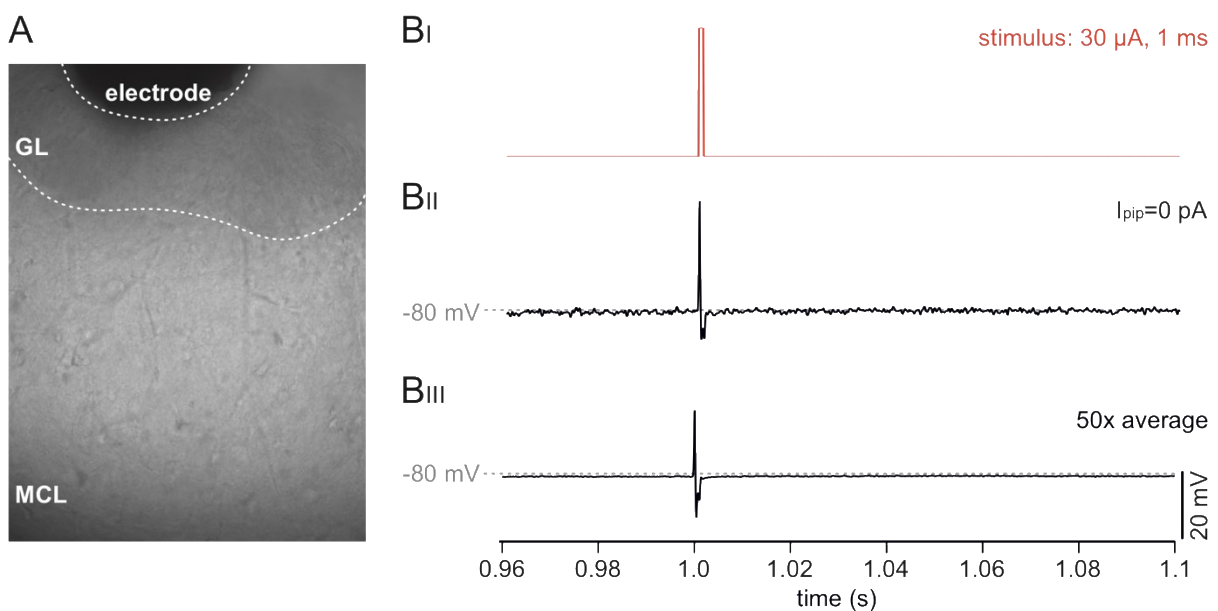


Figure 3.19: Electrical stimulation of the AOB glomerular layer is not sufficient to excite AMCs. (A) DIC image of a bipolar stimulation electrode, positioned in the glomerular layer (GL) of an acute AOB slice. MCL: Mitral cell layer (B) Electrical pulses of 30 μ A for 1 ms do not trigger excitatory postsynaptic potentials or APs in the recorded AMC. (B_I) Stimulus trace of the stimulation electrode: 30 μ A, 1 ms (B_{II}) Current-clamp recording of a representative AMC during electrical stimulation of the GL. Besides the stimulation artifact, no stimulus-induced response is observable. (B_{III}) 50 current-clamp recordings as in (B_{II}) were averaged to verify the absence of a response.

Project D: Decoding of receptor-ligand interactions in the VNO

Our current understanding of AOS information processing is still rudimentary, partially due to the lack of known ligand-receptor pairs in the VNO. Since receptor activation is the first step in the chemosensory processing cascade, this missing information creates a major bottleneck for AOS research. This project aims to deorphanize the darcin receptor and establish an experimental pipeline for future decoding of receptor-ligand interactions in the VNO.

Given that approximately 300 VRs are expressed in vomeronasal neurons in a monogenic pattern, a trial-and-error approach is hardly applicable to identify a specific receptor-ligand pair. In a collaborative effort, we applied an *in silico* protein coevolution algorithm developed

3 Results

in Prof. Paolo Carloni's group (Research Center Jülich). *In silico* predictions for the darcin receptor narrowed the pool of potential candidates down to just one, V2R27. Hence, the following work aims to experimentally verify (or falsify) a function of V2R27 as the darcin receptor.

3.12 Darcin can be recombinantly expressed in *Escherichia coli* and purified

To investigate darcin detection by VSNs, the first step was darcin synthesis via recombinant expression in *E.coli* (methods). Bacteria were transformed with a plasmid that encoded darcin with an N-terminal HIS-tag (Fig. 3.20) [155], [280]. The isolated soluble protein fraction contained a large portion of approx. 20 kDa peptide represented by a prominent band in the coomassie stained gel (Fig. 3.20 A, line 1). 20 kDa was the expected molecular weight for HIS-tagged darcin, which matches the observed band. Next, the soluble protein fraction was purified by immobilized metal affinity chromatography (IMAC), resulting in one isolated protein band, putative darcin (Fig. 3.20 A lines 4-6). The identity of darcin was confirmed by immunoblotting with two different antibodies directed either against the HIS-tag (α -HIS, Fig. 3.20 B_I) or against darcin (α -Mup20, Fig. 3.20 B_{II}), respectively. I, therefore, conclude that the recombinant darcin expression was successful and that purified darcin can now be used to study the darcin-dependent response profile of VSNs.

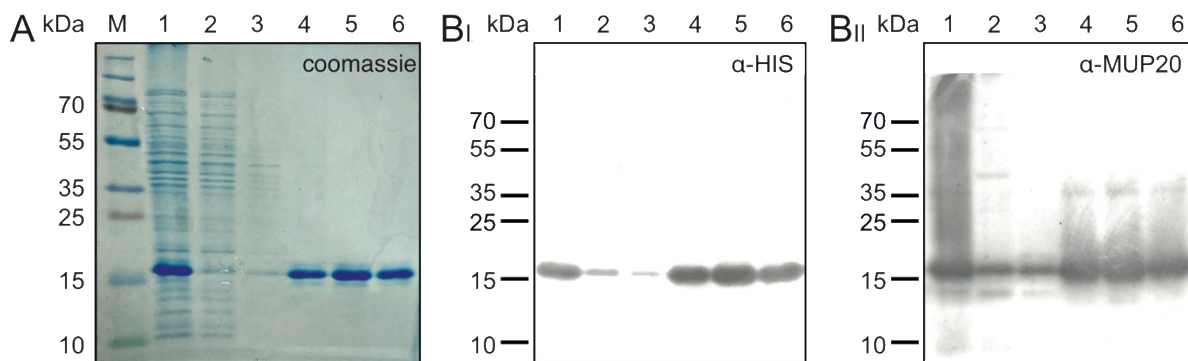


Figure 3.20: Recombinant expression of darcin in *E. coli*. (A) SDS-PAGE gel stained with coomassie shows successful overexpression of a 20 kDa protein and purification by HIS-tag directed affinity chromatography (IMAC). Lines are: M) marker 1) soluble protein fraction of transformed *E. coli* 2) protein fraction that did not bind to the IMAC column 3) 3 pooled wash steps of the IMAC column 4-6) elution of HIS-tagged darcin with an imidazole gradient of 250 mM.

3 Results

mM, 500 mM, and 1M. (B_I) Immunoblotting confirms darcin identity. (B_{II}) Western blot stained with an α -HIS primary antibody, lines as in (A). Specific immunoreaction with HIS-darcin is visible at 20 kDa. (B_{III}) Western blot stained with an α -MUP20 (darcin) primary antibody, lines as in (A). The antibody shows strong unspecific binding, but putative darcin bands at 20 kDa are immunopositive.

3.13 AAV-driven gene transfer is a suitable method for ectopic VR expression in VSNs

Next, I asked how V2R27-expressing VSNs could be identified in the sensory epithelium of the VNO. VRs are expressed in a monoallelic fashion, resulting in one distinct receptor type per neuron. Since V1R and V2R family members show a high degree of homology, specific antibodies for individual subtypes are yet to be generated. I, thus, decided to ectopically express V2R27 in individual VSNs by AAV-driven gene transfer, reasoning that a VSN expresses the endogenous protein machinery that would allow functional expression of a VR gene [246]. Bicistronic expression of a reporter fluorophore should serve to identify infected cells. I delivered rAAV8-smCBA-V2R27-P2A-mCherry via the temporal vein of newborn mice (Fig. 3.21 A), resulting in a systemic distribution of viral particles. The systemic distribution became apparent by injection with a blue dye (Evans blue, Fig. 3.21 B). A control group was injected with AAV8-smCBA-mCherry, a construct missing the VR. After 2-3 weeks of *in vivo* expression, intact mCherry-expressing fluorescent VSNs were observable in both the V2R27-mCherry and the mCherry control group (Fig. 3.21 C, D). However, the V2R27-mCherry AAV exhibited subpar efficiency with a significantly lower number of infected cells, presumably due to cytotoxicity of GPCR overexpression.

3.14 VSNs respond to darcin as well as various pheromone blends in vitro

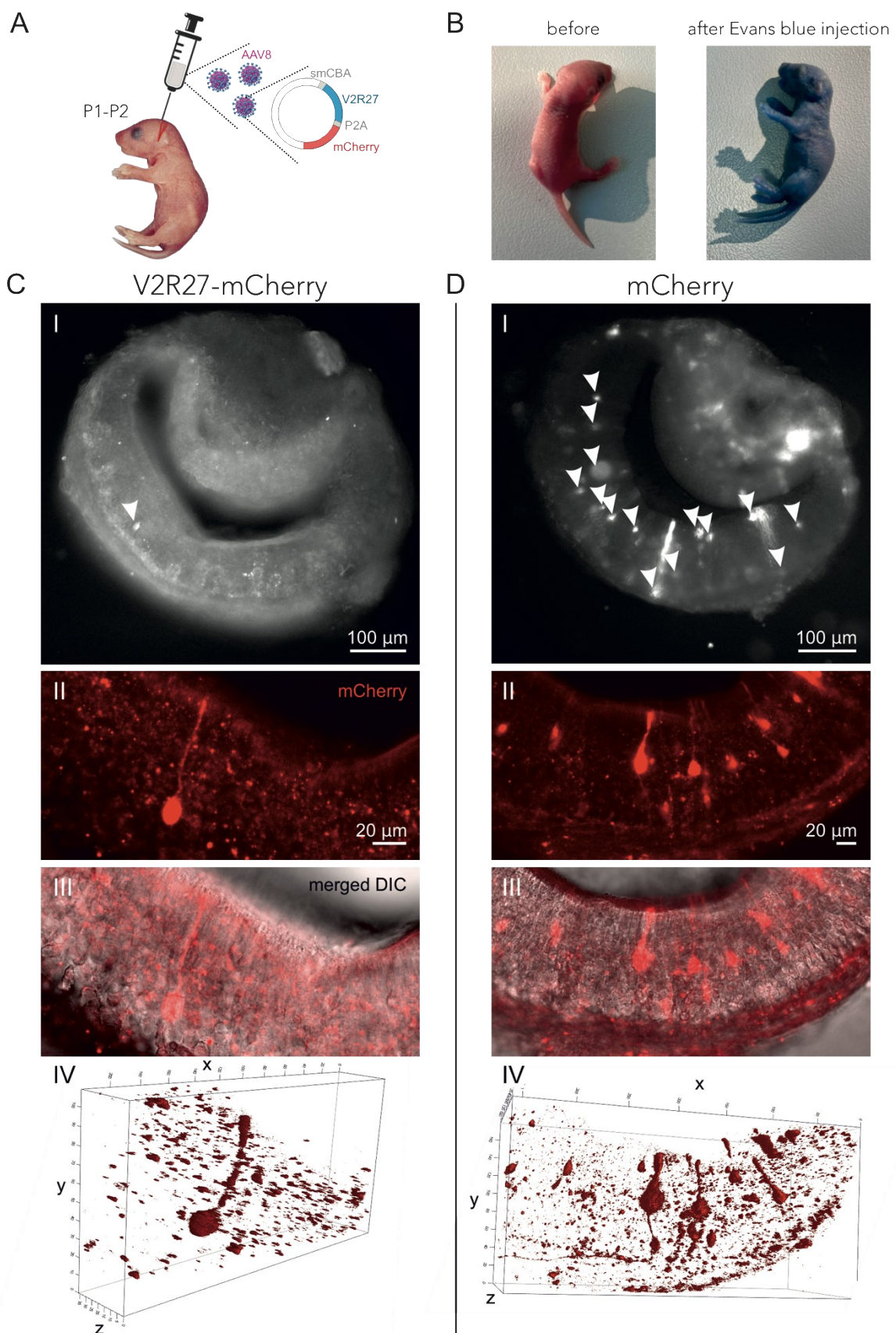
Next, I investigated the response profile of individual VSNs in their physiological environment. Acute coronal VNO slices were bulk loaded with the membrane-permeable Ca^{2+} dye Cal520/AM (Fig. 3.22 A). We utilized Ca^{2+} as a proxy for neuronal activity since this indirect method enables the recording of VSN activity on a large scale.

The fluorescence intensity of individual somata in response to several pheromones and elevated extracellular K^+ was plotted against time (Fig. 3.22 B). Responsive VSNs were either

3 Results

selective for one of the applied stimuli (male urine, female urine, lacrimal gland extract, estrus vaginal smear, darcin) or responded to more than one stimulus class (generalists). Response rates were calculated by normalization to the total number of viable cells, as determined by responses to depolarization (high extracellular K^+) (Fig. 3.22 C). This proof-of-principle dataset suggests that 1) VSNs in this *in vitro* preparation are intact, 2) capable of chemosensation, and 3) that the darcin response rate for C57Bl/6 noninjected mice is approximately 1 %.

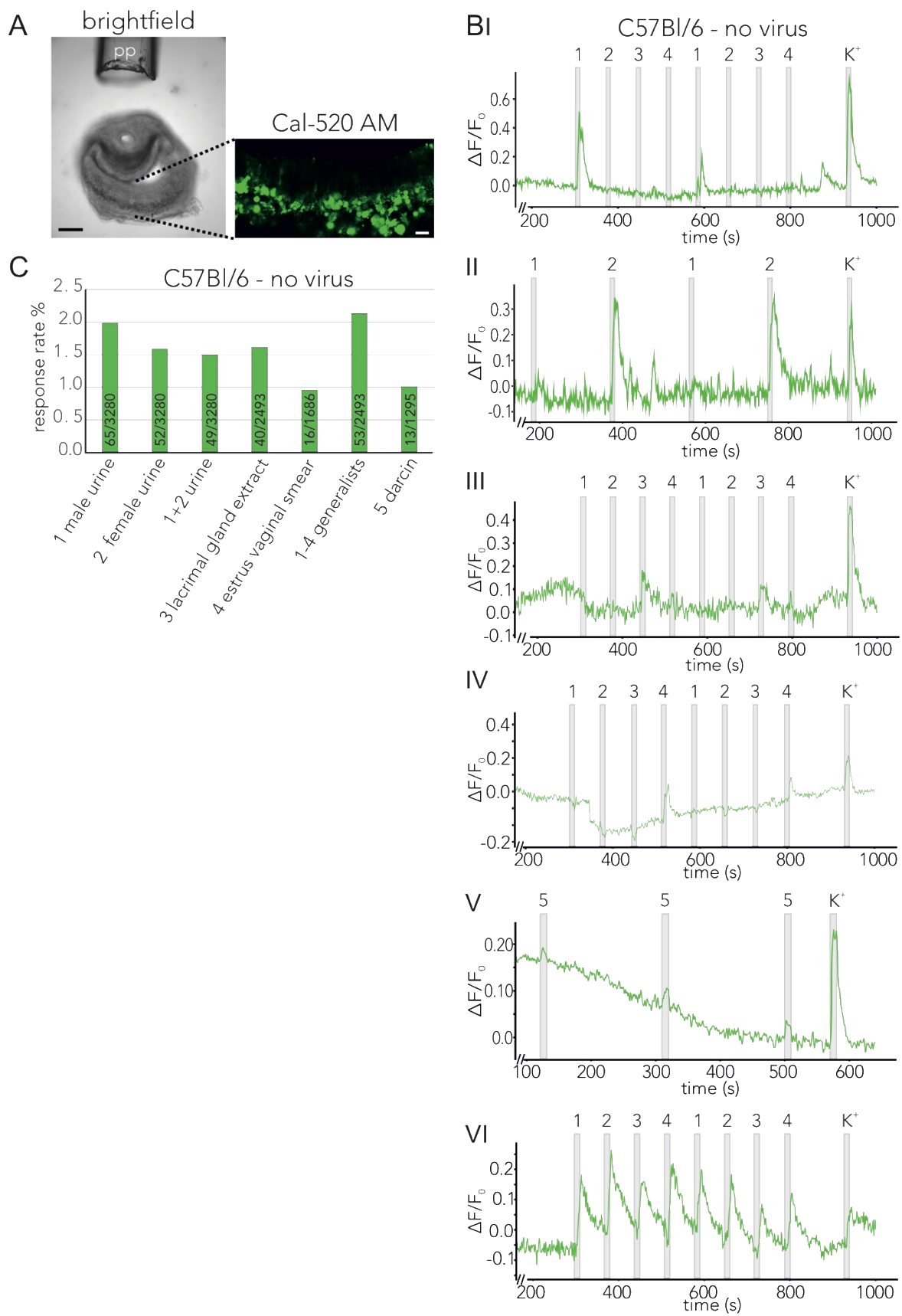
3 Results



3 Results

Figure 3.21: AAV-driven gene transfer for ectopic expression of V2R27 in VSNs. **(A)** Schematic illustration of the procedure. rAAV8-smCBA-V2R27-P2A-mCherry is injected into the temporal vein of neonates. A control group is injected with rAAV8-smCBA-mCherry; P1-P2 = postnatal day 1 to 2, smCBA=small chicken β -actin promotor, P2A=self-cleaving peptide, the construct is depicted in Figure 2.3. **(B)** Example images of a neonate before and after injection with Evans blue into the temporal vein show systemic distribution. **(C-D)** After 2-3 weeks of in vivo expression, mCherry-expressing VSNs are found in acute coronal VNO slices of both experimental groups. **(C_I, D_I)** Widefield fluorescence image of acute coronal VNO slices and mCherry-positive cells as indicated (arrowhead). Note that the mCherry control AAV has a significantly higher infection rate. Maximum projection of confocal z-stacks **(C_{II}, D_{II})**, merged with the corresponding DIC images **(C_{III}, D_{III})**, show mCherry-expression of individual VSNs. The fluorophore locates in all cellular structures - knob, dendrite, soma, and axon. **(C_{IV}, D_{IV})** 3D-reconstruction of the above z-stacks.

3 Results



3 Results

Figure 3.22: Chemosensory activity of VSNs in vitro. (A) Left: Brightfield image of an acute coronal VNO slice and a perfusion pencil (pp) positioned to stimulate the sensory epithelium. Right: Confocal higher magnification view of the sensory epithelium, bulk loaded with the non-ratiometric Ca^{2+} indicator Cal520. (B) Response profile of individual VSNs stimulated with 1) male urine, 2) female urine, 3) lacrimal gland extract, 4) estrus vaginal smear, 5) darcin, or high extracellular K^+ (50 mM). The integrated relative fluorescence intensities ($\Delta F/F$) in user-defined regions of interest are displayed in arbitrary units and plotted as a function of time. Stimulation periods (10 s) are indicated by grey bars. Cells are either selectively responsive to one stimulus class ($\mathbf{B}_1\text{-}\mathbf{B}_v$) or respond to more than one stimulus class and are, thus, termed 'generalists' (\mathbf{B}_{vi}). (C) Average response rates for the different stimulus classes are calculated by normalization to the total number of viable cells, as indicated by responses to high extracellular K^+ . The number of responses is given for each bar (pooled data from ≥ 3 animals of both sexes).

3.15 V2R27 expressing VSNs respond to darcin

Next, I asked whether V2R27-expressing neurons respond with a statistically higher chance to darcin than C57Bl/6 noninjected mice. If true, the absence of such effect in the mCherry control group would establish a causal relationship between V2R27 expression and darcin response. I proceeded with Ca^{2+} imaging experiments in V2R27-mCherry and mCherry control injected mice. Both experimental groups were stimulated and analyzed as described above. When infected V2R27-mCherry (V2R27-mCherry red) cells were stimulated with darcin, 2 out of 3 analyzed cells responded, corresponding to a $\sim 67\%$ response rate (Fig. 3.23 A, C). This probability varies significantly from the response rate of 1 % in C57Bl/6 noninjected mice (Fisher's exact test: $p=0.0004$). In contrast, non-infected VSNs of the same group (V2R27-mCherry green) responded with a probability of 1.1 %, which is essentially identical to the response rate of C57Bl/6 noninjected mice (Fisher's exact test). The observed increase in response probability was absent in the mCherry control group with no responses ($n=0/28$) in infected VSNs (mCherry control red) and a 1.2 % response rate in non-infected cells (mCherry control green) (Fig. 3.23 B, C). Importantly, while none of the infected mCherry control (red) cells responded to darcin, they were capable of chemosensation and responded to other pheromone blends, e. g. male and female urine (Fig. 3.23 B_{II}). In summary, these preliminary results suggest that V2R27 is activated by darcin.

3 Results

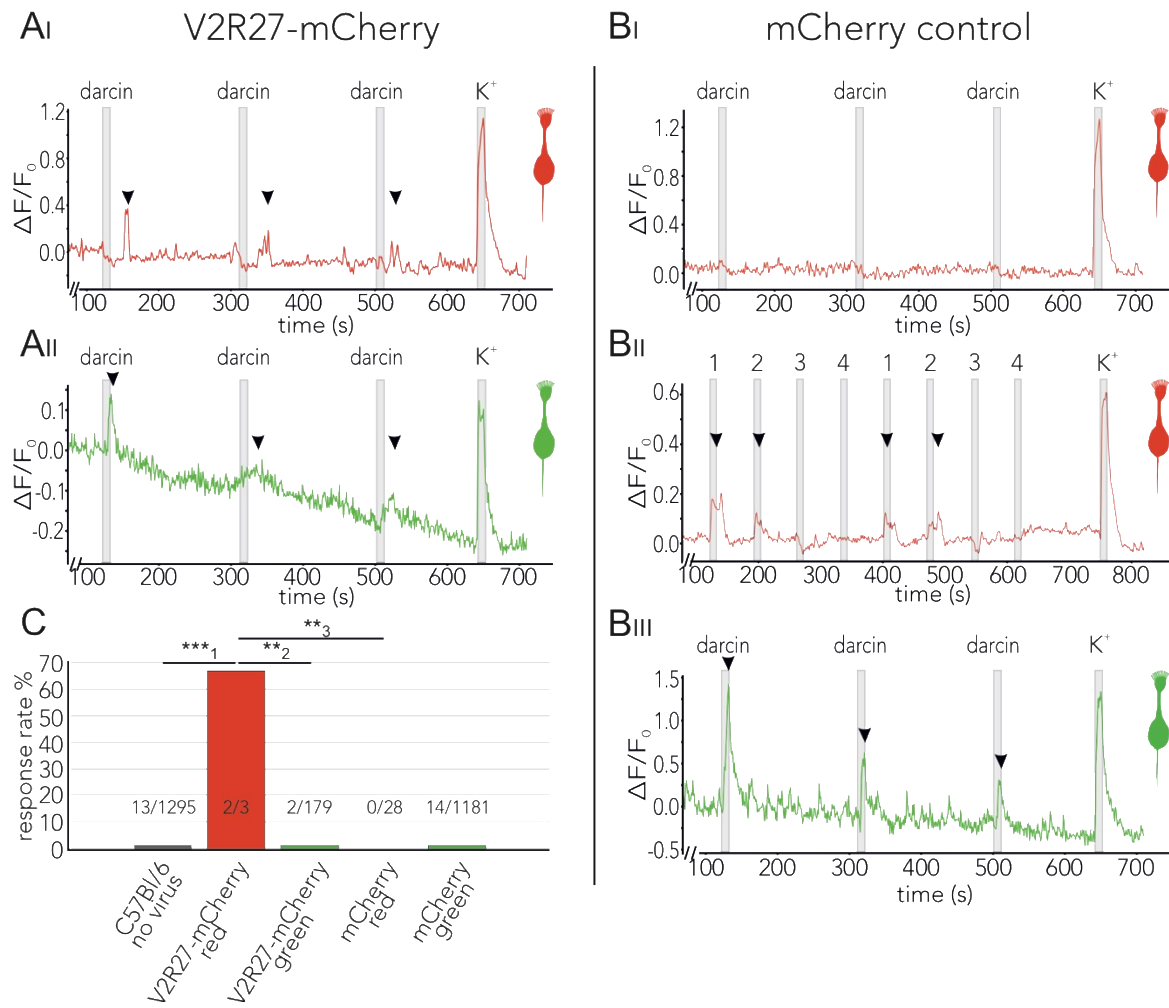


Figure 3.23: V2R27 expression increases the probability for darcin activation in VSNs. (A) Representative recordings of cytosolic Ca^{2+} levels in V2R27-mCherry infected (A_I, red) and non-infected (A_{II}, green) VSNs. Both cell populations have darcin-responsive cells, as indicated by an increase in fluorescence intensity upon darcin stimulation (arrowhead). **(B)** Representative recordings of mCherry control infected (B_I-B_{II}, red) and non-infected (B_{III}, green) VSNs during stimulation (grey bars) with darcin (B_I, B_{II}) or various pheromone blends (B_{II}). Infected mCherry control cells (red) do not respond to darcin but to other pheromone blends like 1) male urine or 2) female urine (3) lacrimal gland extract, 4) estrus vaginal smear). Non-infected mCherry control (green) cells do show darcin responses (arrowhead). **(C)** Average darcin response rates for each experimental group are calculated by normalization to the total number of viable cells, as indicated by responses to high extracellular K^+ . The number of responses is given for each bar (pooled data from ≥ 3 animals of both sexes). The response probability of infected V2R27-mCherry (red) cells is 66 %, significantly higher than the response rates of C57Bl/6 no virus cells (Fisher's exact test, $^{***}p_1=0.0004$), of non-infected V2R27-mCherry (green) cells (Fisher's exact test, $^{**}p_2=0.0011$), and infected mCherry control (red) cells (Fisher's exact test, $^{*}p_3=0.0065$).

3 Results

4 Discussion

Project A: ATP activation of peritubular cells drives testicular sperm transport

Spermatozoa are still immotile, once released into the seminiferous tubule lumen. Motile cilia lining the efferent ducts aid the passage of spermatozoa from the rete testis to the epididymis [281], but seminiferous tubules lack such motile cilia. Hence, there have to be mechanisms that ensure luminal transport of immotile spermatozoa towards the rete testis. Tubule-surrounding smooth muscle cells, TPCs, are attractive candidates as mediators for tubule contractions and, consequently, sperm propagation. A contractile function of TPCs under paracrine control has long been suggested [282], [283], but direct experimental evidence has been missing [284].

Several paracrine mediators, including vasopressin [285], oxytocin [285], prostaglandins [286], and endothelin [40], have been proposed as TPC activators. However, extracellular ATP has explicitly been excluded early on [287]. By contrast, this work reveals that extracellular ATP can indeed function as a potent TPC activator, which triggers cytosolic Ca^{2+} elevations via P2 receptors, coordinated tubule contractions, and eventually directed luminal sperm transport.

In a collaborative effort with other members of my group, my colleague Lina Kenzler demonstrated that besides P2X activation, P2Y receptor-mediated Ca^{2+} release from internal stores is equally involved in TPC contractions. Our data, published in Fleck, Kenzler *et al.* (2021), suggests a Ca^{2+} -induced Ca^{2+} release mechanism that combines internal and external Ca^{2+} sources and is evoked by extracellular ATP [15]. Furthermore, data generated by Dr. David Fleck and available in the same publication, demonstrates that ATP-controlled TPC contractions are reproducible *in vivo*.

Revealing the origin of extracellular ATP as well as the mechanism that triggers ATP release is critical, given its vast implications in male fertility [15], [16], [23], [26], [288]. Until today, this question is not entirely resolved. ATP can be secreted by astrocytes and at neuronal synapses [289], [290], but the absence of efferent nerve endings in the seminiferous tubules and

4 Discussion

interstitial tissue excludes this mechanism [42]. Gelain *et al.* reported regulated ATP release for both Sertoli and germ cells [34], [35]. Moreover, we found P2Y6 transcripts in TPCs (Fig. 3.2 B), which was reported as a mediator for ATP release upon activation [291]. Thus, TPCs could themselves participate in regenerative ATP secretion. Besides that, mechanosensitive ATP release induced by shear stress, stretch, or osmotic swelling of several cell types, adds another putative origin for paracrine ATP signaling within the testis [292].

Whole-mount imaging of isolated seminiferous tubules reveals ATP-induced luminal movement that extends beyond the directly stimulated area (Fig. 3.3). Furthermore, this movement displays stage-dependent directionality (stage group II to III). While *in vivo* contractions were accompanied by propagating wave-like Ca^{2+} signals along the longitudinal axis of the tubules [15], focal ATP stimulation appears insufficient to trigger such regenerative Ca^{2+} waves in isolated tubules. I, therefore, hypothesize that other, likely anatomical/structural, features of the intratubular compartment result in directional transport from stage group II to III. This could be a slanted orientation of Sertoli cell protrusions, creating a favorable movement direction via a natural valve-like structure. In fact, histological observations of the AMH-Cre x Ai14D mouse line lead us to propose such a hypothesis. Alternatively, a locally increased tubule diameter with reduced luminal resistance could explain the observed phenomenon.

What is the role of TPC contractility in male (in)fertility?

Expression of TPC contractility proteins begins during puberty under androgen control and a selective androgen receptor knock-out in TPCs renders mice infertile [293]. So far, seminiferous tubule contractions had not been reported *in vivo*, and most *in vitro* studies lacked direct and quantitative evidence. Hence, a complete translation of TPC contractions from the mouse model to human fertility awaits further physiological investigation. Hitherto, we know that human TPCs show ATP-induced contractions and Ca^{2+} signals *in vitro* [15], [26]. A partial loss of TPC contractility proteins is an accompanying symptom in infertile men [294].

4 Discussion

It is thus tempting to propose that seminiferous tubule contractility in general, and purinergic TPC control in particular, represent novel targets for male infertility treatment and/or better options for male contraception [15].

Project B: Electrophysiological identification of "DSper"

Sperm transition to hyperactivated motility is a crucial requirement for fertilization. Hyperactivation provides the propulsion force required to penetrate through viscous luminal fluids of the female reproductive tract and the protective vestments of the egg. A key player in the transition to hyperactivated motility is the CatSper ion channel [295]. Proper CatSper function requires three concurrent activation mechanisms: (1) membrane depolarization [49], [89], (2) intracellular alkalinization [49], [89], and for primate CatSper specifically (3) abundance of the steroid P4 [86], [89], [241], [242]. While the two latter mechanisms have been described in detail, the source of membrane depolarization remained unknown. Interestingly, depolarization of sperm membrane potential is a common feature of men with subfertility and is associated with a low IVF rate [296], underscoring the importance of sperm membrane potential regulation.

For human spermatozoa, K^+ , Ca^{2+} , Cl^- , and H^+ conductances have been functionally described [85], [86], [89], [99], [241], [297]–[301]. However, the molecular nature of the sperm Na^+ conductance remained puzzling. Upon ejaculation, mammalian spermatozoa are exposed to increased extracellular $[Na^+]$ (~ 15 – 30 mM in the cauda epididymis [302] versus 100 – 150 mM in the seminal plasma). In the female reproductive tract, Na^+ levels are similar to those in serum (140 – 150 mM) [261]. Hence, Na^+ is ideally suited to provide a depolarizing charge upon sperm deposit into the female reproductive tract.

Here, I recorded a novel CatSper-independent cation conductance that exhibits outward rectification as well as potentiation upon capacitation. I propose that this novel conductance is carried by the hypothesized "Depolarizing Channel of human Sperm", DSper, and provides the necessary cation influx that ensures membrane depolarization. I_{DSper} is activated by warm

4 Discussion

temperatures between 22 and 37°C, which makes the protein thermoresponsive within a physiologically relevant temperature range (34.4°C in the epididymis [303], 37°C body core temperature at the site of fertilization). Previous studies showed that capacitated rabbit and human spermatozoa have an inherent temperature sensing ability [304], which could be an additional driving force to guide male gametes from the reservoir in the fallopian tubes towards the warmer fertilization site. Thus, it is likely that human spermatozoa also express a temperature-activated ion channel, which operates in the described temperature range and enables thermotaxis.

In addition, a potential role for this channel is to serve as a sensor for initiation of human sperm capacitation in the female reproductive tract. Human spermatozoa are exposed to elevated temperature during capacitation, especially before and during ovulation, correlated with an increase in basal body temperature by ~1°C [305]. For capacitation to occur, spermatozoa must be exposed to bicarbonate, albumin, and elevated temperature. While sperm capacitation can be achieved *in vitro*, a temperature of 37°C is an absolute requirement. Therefore, the presence of a temperature-sensitive sperm ion channel could serve as a sensor for the onset of capacitation and might ensure the sperm's final maturation in the female reproductive tract.

The pharmacological fingerprint of I_{DSper} indicates functional expression of the temperature-activated ion channel TRPV4, and TRPV4 is detected on the transcript and protein level. I was able to clone TRPV4 from human sperm, and heterologous expression in HEK293 cells led to functional channel assembly with comparable characteristics as recorded in human spermatozoa (Fig. 3.14).

As spermatozoa are able to survive in the female reproductive tract for several days by binding to ciliated epithelia of the fallopian tubes, they must eventually undergo hyperactivation to detach [70]. Accordingly, CatSper-deficient spermatozoa that cannot hyperactivate are not able to ascend the fallopian tubes [306], again underscoring the importance of hyperactivated motility. P4 was shown to inhibit the K⁺ channel of human sperm KSper ($IC_{50} = 7.5 \pm 1.3 \mu M$ [99], [298]), which renders KSper inhibition one of the potential origins for membrane depolarization. However, efficient KSper inhibition requires P4 concentrations in the

4 Discussion

micromolar range, which only occur in close vicinity of the egg. Sperm hyperactivation, however, has to take place in the fallopian tubes, where P4 concentrations are not sufficient to block KSper [101]. Hence, KSper inhibition can only serve as an additional depolarization boost once sperm has reached the egg's sphere.

According to our model (Fig. 4.1), human spermatozoa are exposed to increased temperature and $[Na^+]$ upon deposit to the female reproductive tract. TRPV4-mediated Na^+ influx induces membrane depolarization, which in turn activates both Hv1 and CatSper. H^+ efflux through Hv1 promotes intracellular alkalization and thus facilitates CatSper activation. Ascending the fallopian tubes, spermatozoa are exposed to P4 that constitutes a chemical gradient for chemotaxis towards the egg [307]. In addition to P4, spermatozoa are exposed to the endocannabinoid anandamide (AEA), both secreted by cumulus cells surrounding the egg [308], [309]. P4 binding to ABHD2 releases CatSper inhibition [88], while AEA activates Hv1 [85]. The resulting CatSper opening generates Ca^{2+} influx along the flagellum and serves as the trigger for hyperactivation. P4 not only potentiates CatSper, but it also inhibits KSper-mediated hyperpolarization, which gives the CatSper activation cascade an additional impulse [99], [298].

The observed TRPV4 inward current is rather small in the presence of Ca^{2+} , such as in S3 solution (Fig. 3.6). This results from competition for the channel pore between the divalent and monovalent ions, and it has been reported that extracellular Ca^{2+} inhibits TRPV4 monovalent conductance [310].

The temperature coefficient Q_{10} is a measure of the rate of membrane current as a consequence of increasing the temperature by $10^\circ C$. For TRPV4, the Q_{10} was given between 9 and 19 for recombinantly expressed TRPV4 [263], [264]. However, endogenously expressed TRPV4 channels recorded from aorta endothelial cells [264] exhibit less steep temperature dependence, which is in the range of the Q_{10} of sperm TRPV4 ($Q_{10, \text{ sodium}}=2.30$ for noncapacitated sperm). Different lipid environments or additional channel modifications may be responsible for such differences.

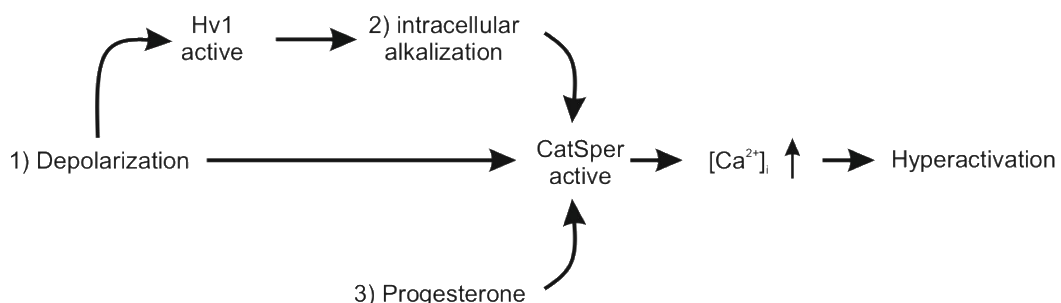
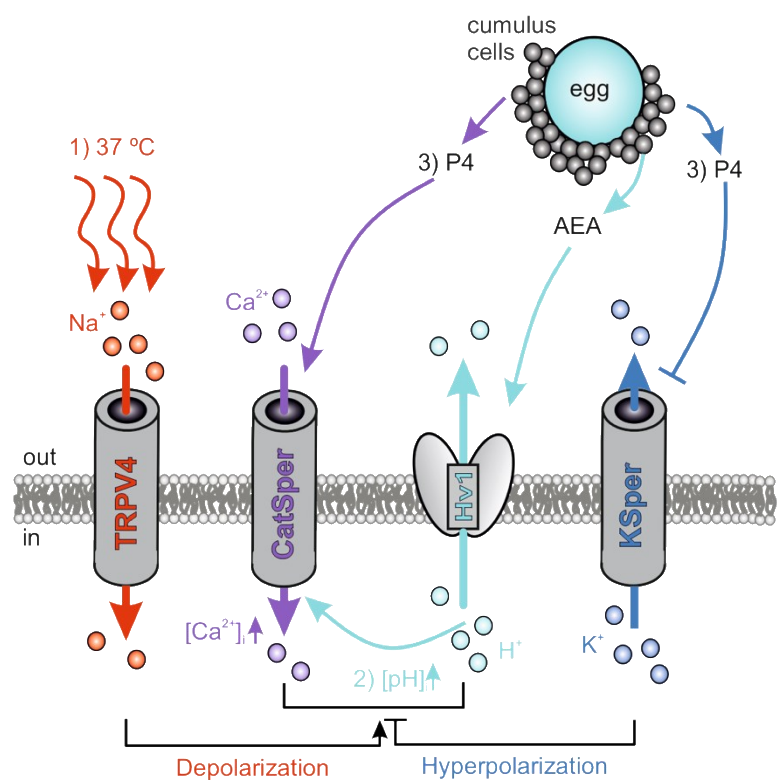


Figure 4.1: Interdependency of ion channel complexes in the human sperm flagellum. Hyperactivation is triggered by a CatSper-mediated rise in cytosolic Ca^{2+} levels. CatSper opening requires three concurrent activation mechanisms: (1) membrane depolarization, (2) intracellular alkalization via Hv1-mediated proton extrusion, and (3) abundance of P4. In our proposed model, the sperm's Na^+ channel TRPV4 is activated by warm temperatures (37°C at the site of fertilization). Na^+ influx through TRPV4 induces (1) membrane depolarization, which then activates both Hv1 and CatSper. Hv1 extrudes protons out of the sperm, thereby leading to (2) intracellular alkalization and additional activation of CatSper. Cumulus cells located around the egg secrete (3) P4 and AEA. P4 releases CatSper inhibition and high P4 concentrations inhibit Ksper-mediated hyperpolarization. AEA was shown to potentiate Hv1 activity. The resulting opening of CatSper generates a Ca^{2+} influx that serves as the trigger for hyperactivation (adapted from: Mundt et al. (2018) [103]).

In previous work with a CatSper2-deficient infertile patient, no remaining cation current was recordable when both Hv1 and Ksper were blocked [241]. However, these recordings were

4 Discussion

performed in a condition where ATP was absent from the pipette solution. According to Phelps *et al.* (2010), intracellular ATP binding to the N-terminal ankyrin repeat domain of TRPV4 has a profound potentiating effect [311], which is a feature shared between TRPV1 and TRPV4 [312]. Indeed, the addition of 4 mM ATP to the pipette solution allowed me to consistently record TRPV4 activity from fertile human spermatozoa.

Our data suggests that TRPV4 activity is increased upon capacitation. Since capacitation encompasses changes in the phosphorylation state of many proteins [313], and TRPV4 requires tyrosine phosphorylation to function correctly [314], TRPV4 phosphorylation likely explains the observed potentiation. It would also explain why only capacitated human spermatozoa appear to be thermotactically responsive [304]. Interestingly, I also observed different I_{DSper} kinetics (i.e., less outward rectification) after capacitation. This finding could also result from phosphorylation, modified lipid composition, or even formation of TRPV4/X heteromers upon capacitation. These aspects should be addressed in future studies.

It is also possible that sperm possess more than one type of temperature-regulated ion channel. The biphasic inhibition of DSper with TRPV4-selective antagonists (Fig. 3.10) does not result in complete current inhibition, particularly in the temperate range between 24 and 32°C. This may suggest an additional non-TRPV4 conductance. The molecular nature of such additional conductance(s) could be either temperature-dependent release of NNC inhibition on CatSper or perhaps the presence of other yet undiscovered temperature-sensitive ion channel(s). Interestingly, according to Hamano *et al.* (2016) [315], murine TRPV4 regulates sperm thermotaxis. However, TRPV4-deficient male mice are fertile, indicating either an additional temperature sensor or a compensatory mechanism. I obtained preliminary evidence for functional TRPP3 expression. The TRPP channel family is divided into PKD2, PKD2L1, and PKD2L2. These three members are classical ciliary ion channels implicated in the development of autosomal polycystic kidney disease (ADPKD) [316]–[320]. PKD2L2 is involved in spermatogenesis and is expressed in the mouse testis [321]. Moreover, men suffering from ADPKD also exhibit increased infertility and necrospermia rates [322], [323]. Additionally, immotile sperm that lack the two central axoneme microtubules (9+0) have been identified in infertile men with ADPKD [92], [324]. Higuchi *et al.* (2014) reported a

4 Discussion

temperature-response profile for TRPP3 between room temperature and 32 °C, followed by a drop in activity at ≥ 36 °C [266]. This observation is in perfect accordance with the most effective block of phenamil, the TRPP3 inhibitor experiments depicted in Figure 3.12. In contrast, the TRPV4 inhibitors HC067047 and RN1734 show less efficacy in the range of 22°C to 32°C (Fig. 3.10). Interestingly, when TRPV4 is investigated in endogenous systems, temperature activation starts at >32 °C for keratinocytes [325] and >33 °C for hippocampal pyramidal neurons [326] representing the second component of the biphasic sperm temperature response profile. I, therefore, hypothesize that human sperm express temperature-sensitive TRPV4, as well as TRPP3 and/or other TRPP members sensitive to phenamil. It is also possible that human sperm possess a TRPV4/TRPP heteromeric complex since HC067047, RN1734, and phenamil exhibit inhibition within the full temperature range with varying efficacy. Notably, heteromer formation has been reported in numerous publications for both channels [316], [327]–[331]. Since my data allows only for preliminary interpretation, future endeavors should focus on the functional implications of TRPP channels in sperm temperature sensitivity and a potential expression of TRPV4/TRPP heteromers.

Selective anti-hTRPV4 antibodies detected TRPV4 in the sperm flagellum (Fig. 3.13), which coincides with the reported locations for ABHD2, CatSper and Hv1 [61], [76], [85]. An open question is whether TRPV4 is also arranged within nanodomains along the longitudinal axis of the sperm flagellum [61] and, if so, how those domains are distributed to be part of the ABHD2, CatSper, and Hv1 interplay. Future high-resolution microscopic approaches should answer this question.

TRPV4 might underlie the aversive effects of increased scrotal temperatures on sperm production and epididymal preservation. As proposed by Bedford *et al.* (1991), increased scrotal temperatures in clothed men contribute substantially to an inferior quality of human ejaculate [332]. By contrast, TRPV4 might also represent an attractive target for male contraceptive drug development since TRPV4 is likely to lie upstream in the signaling cascade leading to sperm hyperactivation and can be heterologously expressed for high-throughput drug screening [103].

Project C: Establishing an optogenetic stimulation paradigm in the murine olfactory bulb

The organization of the AOB sensory map differs dramatically from that of the main olfactory system. VSNs expressing a specific receptor project to multiple glomeruli that reside within spatially restricted domains, and individual glomeruli in the AOB receive input from more than one type of sensory neuron [147]. These differences in VSN targeting have important implications for the logic of olfactory coding in the AOS, which is not entirely understood until today. The aim of this thesis was to establish an *in vitro* stimulation paradigm that mimics sensory input in the presynaptic fraction of the GL. I took an optogenetic approach, in which sensory input was elicited via spatiotemporally defined laser pulses directed at AOB glomeruli of the OMP-ChR2-YFP mouse line. I expected to initiate presynaptic glutamate release from VSNs that I could record in connected AMCs as EPSC/EPSP and/or indirect input from other neurons of the AOB network.

Unfortunately, I was not able to record any laser-induced responses in AMCs. The absence of a response was irrespective of exposure time, laser strength, or scanning speed / inter stimulus interval. The applied stimulation parameters were, in fact, in the same range or even exceeded the stimulation strength used in previous publications for analogous stimulation protocols in the MOB [277]–[279], [333]. I confirmed that recorded AMCs projected at least one dendrite to the GL by fluorophore diffusion loading and/or *post-hoc* morphological reconstruction (Fig. 3.18). I can also exclude that channelrhodopsin is not trafficked to the VSN axon terminals since the ChR2-YFP fusion protein is detectable in laser-scanning confocal images of the AOB GL (Fig. 3.15). Serving as a positive control, I repeated the approach in light-activatable OSNs of the MOB and connected MTCs. Here, I was able to record laser-induced inward currents, indicative of the transient voltage-gated Na^+ current followed by a delayed voltage-gated K^+ current during an AP. Moreover, this response was specific to the dendritic target region, as stimulation areas distant from the target did not elicit the described response. Any stimulation

4 Discussion

paradigm ineffective in the AOB did indeed trigger synaptic transmission in OSN axon terminals within an extensive range of tested exposure times, laser strengths, and scanning speeds. This finding excludes any equipment- or laser-related malfunction and suggests that physiological differences between VSNs and OSNs must be the cause.

One possibility is that the ChR2-YFP protein density is lower in VSN axon terminals, resulting in insufficient depolarization for the initiation of an AP. To test that hypothesis, I bypassed channelrhodopsin activation by positioning a bipolar stimulation electrode in the GL of the AOB for broad glomerular depolarization. Again, none of the recorded AMCs received stimulation-induced input besides the stimulation artifact (Fig. 3.19). Hence, VSN axon terminals seem to be incapable of generating APs that eventually lead to glutamate release at the presynapse. I suspect that VSNs are very susceptible to physiological stress during VNO dissection and slice preparation and might not be in a physiologically healthy condition once being investigated.

A workaround for future studies would be glutamate uncaging [334], [335] in defined dendritic target regions of AMCs. This method does not require functional presynapses and could tackle questions about AOS olfactory information coding that, so far, remain unanswered.

Project D: Decoding of receptor-ligand interactions in the VNO

Communication through pheromones elicits both innate and learned behavioral repertoires that enhance the reproductive success and survival of the species [110]. Male mice deposit scent marks that attract females and increase their chance for mating. In particular the non-volatile protein pheromone darcin (MUP20) elicits innate attraction in females and is recognized by receptors in the vomeronasal organ [155], [175]. Darcin is also a potent stimulus for place and odor conditioning [155] in females. As an example of sexually dimorphic pheromone responses, darcin triggers innate aggressive behavior when presented to males [176].

In their recent publication, Demir and colleagues identify components of the central circuitry that underlie female darcin responses [336]. Central processing extends from the AOB to the

4 Discussion

posterior medial amygdala, where a defined and topographically segregated neuron population integrates pheromonal information with the internal state to elicit an appropriate response [336]. Yet, the first stages of darcin chemosensation, e.g., the detection by peripheral VSNs, transmission to the AOB, and AOB processing, are still *terra incognita*.

Here, I provide preliminary results that identify V2R27 as a putative darcin receptor. We applied an *in silico*-based protein coevolution algorithm developed in Prof. Paolo Carloni's group (Research Center Jülich) to predict the molecular identity of the darcin receptor. Notably, the algorithm successfully predicts two verified / published ligand-receptor pairs ESP1-V2Rp5 [178] and ESP22-V2Rp4 [180], respectively. The pool of potential darcin receptor candidates was narrowed down to just one, V2R27.

Via Ca^{2+} imaging in acute VNO slices, I ascertained the darcin response rate of wildtype CD57Bl/6 VSNs, which was approximately 1%. This is consistent with previously published electrophysiological investigations of VSN darcin responses (1.1% [137], [337]).

AAV-driven gene transfer proved a successful method to express V2R27-P2A-mCherry or mCherry, respectively, in VSNs. However, the infection rate for the V2R27-P2A-mCherry construct was unexpectedly low compared to the mCherry control construct or results from Lee *et al.* (2019) [246], who first published this novel method. The overexpression of a large GPCR might negatively affect cellular translation or trafficking mechanisms. In their recent publication, Lee and colleagues ectopically expressed V1R receptors, which are approx. 2- to 3-times smaller than V2Rs and might have less severe side effects.

I found that the few V2R27-expressing VSNs responded to darcin with a statistically higher probability (67 %, n=2/3), while response rates remained at CD57Bl/6 levels in the mCherry control group and in uninfected VSNs. While these preliminary results are promising, the number of analyzed cells is too low and has to be increased to corroborate this finding. Besides that, the next steps of the project will include the CRISPR/Cas9 generation of a V2R27 reporter-line and a V2R27 knock-out line. With these mouse lines, we aim to verify (or falsify) V2R27 as a darcin receptor and trace V2R27 axonal projections in the GL of the AOB. In parallel, the K.O. mouse line will inform about V2R27 loss-of-function implications in behavior and whether additional VRs are responsive to darcin. Future investigations should also

4 Discussion

elucidate how sexually dimorphic darcin responses can be explained on levels of receptor signaling (e.g., response rates) or AOB wiring (e.g., glomerular targets and AMC sampling). As applied in this thesis, virus-driven gene transfer could also be a powerful tool for multi-synaptic anterograde tracing of complete V2R27 neuronal circuitries (or any other VR-specific circuitry), as described for the Cre-dependent herpes simplex virus by Lo and colleagues [338]. In summary, this work established a valuable toolkit for recombinant pheromone protein expression and ectopic VR expression by AAV-driven gene transfer in the VNO. The experimental pipeline applied in this thesis can now be adapted to deorphanize other VRs in the future. Finally, my data provides the first experimental basis for V2R27 as the darcin receptor.

5 Summary

The molecular and cellular mechanisms that govern testicular transport of immotile spermatozoa are controversial, if not elusive. Here, I reveal that extracellular ATP serves as an important paracrine messenger to activate smooth muscle TPCs that surround seminiferous tubules. ATP triggers cytosolic Ca^{2+} elevations via P2 receptors, coordinated TPC contractions, and eventually luminal sperm transport. My data suggests a stage-dependent directionality of sperm transport, while the underlying mechanism for said directionality remains to be identified. ATP-induced Ca^{2+} elevations are confined to directly stimulated areas in isolated whole-mount tubules. Thus, the observed directionality of luminal transport must rely on anatomical / morphological features of the intratubular compartment.

Once spermatozoa enter the fallopian tubes within the female reproductive tract, they must transition to hyperactivated motility to ascend through viscous fluids and eventually overcome the egg's protective vestments. A key component for hyperactivation is the sperm Ca^{2+} channel CatSper, but the origin of membrane depolarization that facilitates CatSper opening, was undescribed. My work identified "DSper" - the depolarizing ion channel of human sperm - as the temperature-activated cation channel TRPV4. Under physiological conditions, TRPV4 conducts a Na^+ inward current that provides the necessary positive net charge for membrane potential depolarization. TRPV4 activity was increased upon capacitation in a temperature-sensitive range between 22°C and 37°C. My work, thus, contributes to a better understanding of human sperm physiology and reveals the molecular basis for sperm membrane depolarization and temperature-sensitivity.

The sense of smell is a vital tool for many species to perceive and adapt to the outside world. Several highly complex olfactory subsystems have evolved to process the enormous magnitude of olfactory stimuli. Our current knowledge of the accessory olfactory system that is involved in social information processing, however, is rudimentary. Therefore, the overall aim of this work was to gain a more profound understanding of chemosensory signaling mechanisms in the accessory olfactory system. I established an optogenetic stimulation

6 Abbreviations

paradigm in the murine main olfactory bulb, that mimics peripheral sensory input and will facilitate future investigations of the first central olfactory processing stages *in vitro*. Surprisingly, I found that VSN sensory afferents were incapable of synaptic transmission in corresponding *in vitro* settings, which renders the optogenetic stimulation paradigm unsuitable for further AOB studies.

In addition, my work focused on peripheral chemosensation in the VNO. Darcin is a potent pheromone that elicits sexually dimorphic responses in recipients. I aimed to verify (or falsify) V2R27 as the darcin receptor, which was previously predicted by a protein coevolution algorithm. I established AAV-driven gene transfer in VSNs for ectopic V2R27 expression. Preliminary results suggest a significantly higher response rate for infected V2R27-expressing VSNs, as compared to noninfected control groups. This work, thus, provides an experimental basis for future receptor deorphanization studies and preliminary evidence for V2R27 as a darcin receptor.

In summary, this thesis addresses several questions about signaling mechanisms in both reproductive and neuronal tissues. My work, thus, provides substantial advances in our knowledge about these two essential physiological systems.

6 Abbreviations

ABHD2	Abhydrolase domain-containing protein 2
AMC	AOB mitral cell
AOB	Accessory olfactory bulb
AOS	Accessory olfactory system
AP	Action potential
ATP	Adenosine-triphosphate
AUC	Area under curve
BTB	Blood testis barrier
BV	Blood vessel

6 Abbreviations

CaM	Calmodulin
Ca _v	Voltage-gated calcium channel
CD	Cytoplasmid droplet
C _{mem}	Membrane capacitance
EPSC	Excitatory postsynaptic current
EPSP	Excitatory postsynaptic potential
FPR-rs	Formyl peptide receptor-related proteins
GC	Granule cell
GFP	Green fluorescent protein
GG	Grüneberg ganglion
GL	Glomerular layer
GPCR	G-protein coupled receptor
I _{catSper}	CatSper current
I _{Dsper}	Dsper current
I _{pip}	Holding current
LOT	Lateral olfactory tract
MOB	Main olfactory bulb
MOE	Main olfactory epithelium
MOS	Main olfactory system
ms	Milisecond
MTC	mitral- and tufted cell
MUP	Major urinary protein
mV	Millivolt
MWCO	Molecular weight cut off
OSN	Olfactory sensory neuron
P2	Purinoceptor 2 family
pA	Picoampere
PGC	Periglomerular cell
PIP ₂	Phosphatidylinositol-4,5-bisphosphate

pp	Patch pipette
ROI	Region of interest
SO	Septal organ of Masera
SSC	Spermatogonial stem cell
TPC	Testicular peritubular cell
TRP	Transient receptor potential family
V1R	Vomeronasal type 1 receptor
V2R	Vomeronasal type 2 receptor
V_{hold}	Holding potential
V_{mem}	Membrane potential
VNO	Vomeronasal organ
VR	Vomeronasal receptor
V_{rest}	Resting potential
YFP	Yellow fluorescent protein

7 Contributions by others

Fig. 2.1 TRPV-GFP plasmid	Cloned by Prof. Polina Lishko
Fig. 2.2 His-darcin plasmid	Provided by Em. Prof. Rob Beynon
Fig. 2.3 AAV8-smCBA-V2R27-P2A-mCherry	Provided by Prof. Jeremy McIntyre
AAV8-smCBA-mCherry	Provided by Prof. Jeremy McIntyre
Fig. 3.2 A	TPCs cultured by Robert Moosmann
Fig. 3.2 C-G	Pooled electrophysiological data acquired by Robert Moosmann and myself
Fig. 3.5	Data recorded by Prof. Polina Lishko
Fig. 3.13 C	Western Blot by Prof. Polina Lishko
Fig. 3.14 B	Western Blot by Prof. Polina Lishko

8 Funding

I received financial support from the German Academic Exchange Service DAAD (Jahresstipendium) and the German Research Foundation DFG (RTG2416 MultiSenses-MultiScales).

9 References

- [1] U. Mina and P. Kumar, *Life Sciences Fundamentals and Practice Part -I*, 4th ed. Pathfinder Academy Private Limited, 2014.
- [2] E. Knobil and J. D. Neill, *Physiology of Reproduction*, 3rd ed. Elsevier, 2006.
- [3] F. J. Ebling, A. N. Brooks, A. S. Cronin, H. Ford, and J. B. Kerr, "Estrogenic induction of spermatogenesis in the hypogonadal mouse.", *Endocrinology*, vol. 141, no. 8, pp. 2861–9, Aug. 2000, doi: 10.1210/endo.141.8.7596.
- [4] J. E. Weber, L. D. Russell, V. Wong, and R. N. Peterson, "Three-dimensional reconstruction of a rat stage V Sertoli cell: II. Morphometry of Sertoli--Sertoli and Sertoli-germ-cell relationships.", *Am. J. Anat.*, vol. 167, no. 2, pp. 163–79, Jun. 1983, doi: 10.1002/aja.1001670203.
- [5] D. G. de Rooij and M. D. Griswold, "Questions about spermatogonia posed and answered since 2000.", *J. Androl.*, vol. 33, no. 6, pp. 1085–95, 2012, doi: 10.2164/jandrol.112.016832.
- [6] M. Komeya and T. Ogawa, "Spermatogonial stem cells: Progress and prospects," *Asian J. Androl.*, vol. 0, no. 0, p. 0, Sep. 2015, doi: 10.4103/1008-682X.154995.
- [7] H. Chiarini-Garcia and L. D. Russell, "High-resolution light microscopic characterization of mouse spermatogonia," *Biol. Reprod.*, vol. 65, no. 4, pp. 1170–1178, 2001, doi: 10.1095/biolreprod65.4.1170.
- [8] R. A. Hess and L. R. De Franca, "Spermatogenesis and cycle of the seminiferous epithelium," *Adv. Exp. Med. Biol.*, vol. 636, pp. 1–15, 2008, doi: 10.1007/978-0-387-09597-4_1.
- [9] L. Hermo, R.-M. Pelletier, D. G. Cyr, and C. E. Smith, "Surfing the wave, cycle, life history, and genes/proteins expressed by testicular germ cells. Part 2: changes in spermatid organelles associated with development of spermatozoa.", *Microsc. Res. Tech.*, vol. 73, no. 4, pp. 279–319, Apr. 2010, doi: 10.1002/jemt.20787.
- [10] A. Mayerhofer, M. B. Frungieri, S. Fritz, A. Bulling, B. Jessberger, and H. J. Vogt, "Evidence for catecholaminergic, neuronlike cells in the adult human testis: Changes associated with testicular pathologies," *J. Androl.*, vol. 20, no. 3, pp. 341–347, May 1999, doi: 10.1002/j.1939-4640.1999.tb02527.x.
- [11] M. Nistal, R. Paniagua, and M. A. Abaurrea, "Varicose axons bearing 'synaptic' vesicles on the basal lamina of the human seminiferous tubules," *Cell Tissue Res.*, vol. 226, no. 1, pp. 75–82, 1982, doi: 10.1007/BF00217083.
- [12] D. W. Carr and T. S. Acott, "Intracellular pH Regulates Bovine Sperm Motility and Protein Phosphorylation1," *Biol. Reprod.*, vol. 41, no. 5, pp. 907–920, Nov. 1989, doi: 10.1095/biolreprod41.5.907.
- [13] T. S. Acott and D. W. Carr, "Inhibition of bovine spermatozoa by caudal epididymal fluid: II. Interaction of pH and a quiescence factor," *Biol. Reprod.*, vol. 30, no. 4, pp. 926–935, 1984, doi: 10.1095/biolreprod30.4.926.

9 References

- [14] S. Hamamah and J. L. Gatti, "Role of the ionic environment and internal pH on sperm activity," in *Human Reproduction*, 1998, vol. 13, no. SUPPL. 4, pp. 20–30, doi: 10.1093/humrep/13.suppl_4.20.
- [15] D. Fleck, L. Kenzler, N. Mundt, M. Strauch, N. Uesaka, R. Moosmann, F. Bruentgens, A. Missel, A. Mayerhofer, D. Merhof, J. Spehr, and M. Spehr, "ATP activation of peritubular cells drives testicular sperm transport," *Elife*, vol. 10, Jan. 2021, doi: 10.7554/elife.62885.
- [16] D. Fleck, N. Mundt, F. Bruentgens, P. Geilenkirchen, P. A. Machado, T. Veitinger, S. Veitinger, S. M. Lipartowski, C. H. Engelhardt, M. Oldiges, J. Spehr, and M. Spehr, "Distinct purinergic signaling pathways in prepubescent mouse spermatogonia," *J. Gen. Physiol.*, vol. 148, no. 3, pp. 253–271, 2016, doi: 10.1085/jgp.201611636.
- [17] G. Burnstock, "Purinergic signalling," *Br. J. Pharmacol.*, vol. 147 Suppl, pp. S172-81, Jan. 2006, doi: 10.1038/sj.bjp.0706429.
- [18] D. Satchell, "The effects of ATP and related nucleotides on visceral smooth muscle," *Ann. N. Y. Acad. Sci.*, vol. 603, pp. 53–63, 1990.
- [19] R. A. Olsson and J. D. Pearson, "Cardiovascular purinoceptors," *Physiol. Rev.*, vol. 70, no. 3, pp. 761–845, Jul. 1990.
- [20] F. Di Virgilio, V. Bronte, D. Collavo, and P. Zanovello, "Responses of mouse lymphocytes to extracellular adenosine 5'-triphosphate (ATP). Lymphocytes with cytotoxic activity are resistant to the permeabilizing effects of ATP," *J. Immunol.*, vol. 143, no. 6, pp. 1955–60, Sep. 1989.
- [21] L. S. Antonio, R. R. Costa, M. D. Gomes, and W. A. Varanda, "Mouse Leydig cells express multiple P2X receptor subunits," *Purinergic Signal.*, vol. 5, no. 3, pp. 277–287, Nov. 2009, doi: 10.1007/s11302-008-9128-9.
- [22] C. Foresta, M. Rossato, A. Nogara, F. Gottardello, P. Bordon, and F. Di Virgilio, "Role of P2-purinergic receptors in rat Leydig cell steroidogenesis," *Biochem. J.*, pp. 499–504, Dec. 1996.
- [23] S. Veitinger, T. Veitinger, S. Cainarca, D. Fluegge, C. H. Engelhardt, S. Lohmer, H. Hatt, S. Corazza, J. Spehr, E. M. Neuhaus, and M. Spehr, "Purinergic signalling mobilizes mitochondrial Ca^{2+} in mouse Sertoli cells," *J. Physiol.*, vol. 589, no. 4, pp. 5033–55, Nov. 2011, doi: 10.1113/jphysiol.2011.216309.
- [24] R. Glass, M. Bardini, T. Robson, and G. Burnstock, "Expression of nucleotide P2X receptor subtypes during spermatogenesis in the adult rat testis," *Cells. Tissues. Organs*, vol. 169, no. 4, pp. 377–87, Jan. 2001.
- [25] N. Mundt, "Physiological analysis of purinergic signaling mechanisms in the mouse testis," *Master's thesis, RWTH Aachen Univ.*, no. September, 2016.
- [26] L. Walenta, D. Fleck, T. Fröhlich, H. Von Eysmondt, G. J. Arnold, J. Spehr, J. U. Schwarzer, F. M. Köhn, M. Spehr, and A. Mayerhofer, "ATP-mediated Events in Peritubular Cells Contribute to Sterile Testicular Inflammation," *Sci. Rep.*, vol. 8, no. 1, pp. 1–13, Dec. 2018, doi: 10.1038/s41598-018-19624-3.
- [27] B. Navarro, K. Miki, and D. E. Clapham, "ATP-activated P2X2 current in mouse spermatozoa," *Proc. Natl. Acad. Sci. U. S. A.*, vol. 108, no. 34, pp. 14342–7, Aug. 2011, doi: 10.1073/pnas.1111695108.

9 References

- [28] B. P. Bean and D. D. Friel, “ATP-activated channels in excitable cells.” *Ion channels*, vol. 2. Springer, Boston, MA, pp. 169–203, 1990, doi: 10.1007/978-1-4615-7305-0_5.
- [29] B. P. Bean, “Pharmacology and electrophysiology of ATP-activated ion channels,” *Trends Pharmacol. Sci.*, vol. 13, no. C, pp. 87–90, Jan. 1992, doi: 10.1016/0165-6147(92)90032-2.
- [30] M. P. Abbracchio and G. Burnstock, “Purinoceptors: are there families of P2X and P2Y purinoceptors?,” *Pharmacol. Ther.*, vol. 64, no. 3, pp. 445–75, Jan. 1994.
- [31] E. A. Barnard, G. Burnstock, and T. E. Webb, “G protein-coupled receptors for ATP and other nucleotides: a new receptor family,” *Trends Pharmacol. Sci.*, vol. 15, no. 3, pp. 67–70, Mar. 1994, doi: 10.1016/0165-6147(94)90280-1.
- [32] S. A. Thomas and R. I. Hume, “Permeation of both cations and anions through a single class of ATP-activated ion channels in developing chick skeletal muscle.,” *J. Gen. Physiol.*, vol. 95, no. 4, pp. 569–90, Apr. 1990.
- [33] B. S. Khakh and R. A. North, “P2X receptors as cell-surface ATP sensors in health and disease,” *Nature*, vol. 442, no. 7102, pp. 527–32, Aug. 2006, doi: 10.1038/nature04886.
- [34] D. P. Gelain, L. F. de Souza, and E. A. Bernard, “Extracellular purines from cells of seminiferous tubules,” *Mol. Cell. Biochem.*, vol. 245, no. 1–2, pp. 1–9, Mar. 2003.
- [35] D. P. Gelain, E. A. Casali, R. B. de Oliveira, L. F. de Souza, F. Barreto, F. Dal-Pizzol, and J. C. F. Moreira, “Effects of follicle-stimulating hormone and vitamin A upon purinergic secretion by rat Sertoli cells.,” *Mol. Cell. Biochem.*, vol. 278, no. 1–2, pp. 185–94, Oct. 2005, doi: 10.1007/s11010-005-7500-4.
- [36] N. Lalevée, C. Rogier, F. Becq, and M. Joffre, “Acute effects of adenosine triphosphates, cyclic 3',5'-adenosine monophosphates, and follicle-stimulating hormone on cytosolic calcium level in cultured immature rat Sertoli cells.,” *Biol. Reprod.*, vol. 61, no. 2, pp. 343–52, Aug. 1999.
- [37] Y. Clermont, “Contractile elements in the limiting membrane of the seminiferous tubules of the rat,” *Exp. Cell Res.*, vol. 15, no. 2, pp. 438–440, Oct. 1958, doi: 10.1016/0014-4827(58)90052-1.
- [38] M. H. Ross, “The fine structure and development of the peritubular contractile cell component in the seminiferous tubules of the mouse,” *Am. J. Anat.*, vol. 121, no. 3, pp. 523–557, Nov. 1967, doi: 10.1002/aja.1001210307.
- [39] M. Ailenberg, P. S. Tung, and I. B. Fritz, “Transforming Growth Factor- β Elicits Shape Changes and Increases Contractility of Testicular Peritubular Cells1,” *Biol. Reprod.*, vol. 42, no. 3, pp. 499–509, Mar. 1990, doi: 10.1095/biolreprod42.3.499.
- [40] A. Filippini, A. Tripiciano, F. Palombi, A. Teti, R. Paniccia, M. Stefanini, and E. Ziparo, “Rat testicular myoid cells respond to endothelin: characterization of binding and signal transduction pathway.,” *Endocrinology*, vol. 133, no. 4, pp. 1789–1796, Oct. 1993, doi: 10.1210/endo.133.4.8404621.
- [41] K. Miyake, M. Yamamoto, H. Narita, J. Hashimoto, and H. Mitsuya, “Evidence for contractility of the human seminiferous tubule confirmed by its response to noradrenaline and acetylcholine,” *Fertil. Steril.*, vol. 46, no. 4, pp. 734–737, Oct. 1986, doi: 10.1016/S0015-0282(16)49663-9.
- [42] A. Tripiciano, A. Filippini, Q. Giustiniani, and F. Palombi, “Direct Visualization of Rat

9 References

Peritubular Myoid Cell Contraction in Response to Endothelin1," *Biol. Reprod.*, vol. 55, no. 1, pp. 25–31, Jul. 1996, doi: 10.1095/biolreprod55.1.25.

[43] L. C. Ellis, L. E. Buhrliey, and J. L. Hargrove, "Species differences in contractility of seminiferous tubules and tunica albuginea as related to sperm transport through the testis," *Syst. Biol. Reprod. Med.*, vol. 1, no. 2, pp. 139–146, 1978, doi: 10.3109/01485017808988330.

[44] G. C. Harris and H. D. Nicholson, "Stage-related differences in rat seminiferous tubule contractility in vitro and their response to oxytocin," *J. Endocrinol.*, vol. 157, no. 2, pp. 251–257, May 1998, doi: 10.1677/joe.0.1570251.

[45] A. D. Losinno, A. Morales, D. Fernández, and L. A. Lopez, "Peritubular Myoid Cells from Rat Seminiferous Tubules Contain Actin and Myosin Filaments Distributed in Two Independent Layers1," *Biol. Reprod.*, vol. 86, no. 5, pp. 150–151, May 2012, doi: 10.1095/biolreprod.111.095158.

[46] R. T. S. Worley and J. A. Leendertz, "A videomicrographic low-frequency movement analyser (VLMA) and perfusion chamber for recording and analysis of the physical behaviour of seminiferous tubules and other contractile tissues in vitro," *J. Microsc.*, vol. 151, no. 1, pp. 61–69, Jul. 1988, doi: 10.1111/j.1365-2818.1988.tb04613.x.

[47] G. Burnstock, "Purinergic signalling: from discovery to current developments," *Exp. Physiol.*, vol. 99, no. 1, pp. 16–34, Jan. 2014, doi: 10.1113/expphysiol.2013.071951.

[48] P. V. Lishko, Y. Kirichok, D. Ren, B. Navarro, J.-J. Chung, and D. E. Clapham, "The Control of Male Fertility by Spermatozoan Ion Channels," *Annu. Rev. Physiol.*, vol. 74, no. 1, pp. 453–475, Mar. 2012, doi: 10.1146/annurev-physiol-020911-153258.

[49] Y. Kirichok, B. Navarro, and D. E. Clapham, "Whole-cell patch-clamp measurements of spermatozoa reveal an alkaline-activated Ca²⁺ channel," *Nature*, vol. 439, no. 7077, pp. 737–740, Feb. 2006, doi: 10.1038/nature04417.

[50] D. A. Leeuwenhoeck, "Letter of 1677 to the Royal Society: De natis è semine genital animalculis," *R. Soc. London*, 1678.

[51] E. R. Roldan, T. Murase, and Q. X. Shi, "Exocytosis in spermatozoa in response to progesterone and zona pellucida," *Science*, vol. 266, no. 5190, pp. 1578–81, Dec. 1994.

[52] M. Okabe, "The cell biology of mammalian fertilization," *Development*, vol. 140, no. 22, pp. 4471–4479, 2013, doi: 10.1242/dev.090613.

[53] D. E. C. Polina V. Lishko, Yuriy Kirichok, Dejian Ren, Betsy Navarro, Jean-Ju Chung, "The Control of Male Fertility by Spermatozoan Ion Channels," *Annu Rev Physiol.*, no. 74, pp. 453–475, 2012, doi: 10.1126/scisignal.2001449.Engineering.

[54] C. B. Lindemann, "Testing the Geometric Clutch hypothesis," *Biology of the Cell*, vol. 96, no. 9. Elsevier, pp. 681–690, 2004, doi: 10.1016/j.biolcel.2004.08.001.

[55] C. B. Lindemann, "Geometric clutch model version 3: The role of the inner and outer arm dyneins in the ciliary beat," *Cell Motil. Cytoskeleton*, vol. 52, no. 4, pp. 242–254, 2002, doi: 10.1002/cm.10049.

[56] C. J. Brokaw, "Calcium-induced asymmetrical beating of triton-demembranated sea urchin sperm flagella," *J. Cell Biol.*, vol. 82, no. 2, pp. 401–411, 1979, doi: 10.1083/jcb.82.2.401.

[57] H.-C. Ho, K. A. Granish, and S. S. Suarez, "Hyperactivated motility of bull sperm is

9 References

triggered at the axoneme by Ca²⁺ and not cAMP.,” *Dev. Biol.*, vol. 250, no. 1, pp. 208–17, Oct. 2002.

[58] S. Ishijima, H. Mohri, J. W. Overstreet, and A. I. Yudin, “Hyperactivation of monkey spermatozoa is triggered by Ca²⁺ and completed by cAMP,” *Mol. Reprod. Dev.*, vol. 73, no. 9, pp. 1129–1139, Sep. 2006, doi: 10.1002/mrd.20420.

[59] C. B. Lindemann, J. S. Goltz, and K. S. Kanous, “Regulation of activation state and flagellar wave form in epididymal rat sperm: Evidence for the involvement of both CA2+ and cAMP,” *Cell Motil. Cytoskeleton*, vol. 8, no. 4, pp. 324–332, Jan. 1987, doi: 10.1002/cm.970080405.

[60] S. S. Suarez, S. M. Varosi, and X. Dai, “Intracellular calcium increases with hyperactivation in intact, moving hamster sperm and oscillates with the flagellar beat cycle.,” *Proc. Natl. Acad. Sci. U. S. A.*, vol. 90, no. 10, pp. 4660–4, May 1993.

[61] M. R. Miller, S. J. Kenny, N. Mannowetz, S. A. Mansell, M. Wojcik, S. Mendoza, R. S. Zucker, K. Xu, and P. V. Lishko, “Asymmetrically Positioned Flagellar Control Units Regulate Human Sperm Rotation,” *Cell Rep.*, vol. 24, no. 10, pp. 2606–2613, Sep. 2018, doi: 10.1016/j.celrep.2018.08.016.

[62] K. Inaba, “Molecular architecture of the sperm flagella: molecules for motility and signaling.,” *Zoolog. Sci.*, vol. 20, no. 9, pp. 1043–1056, 2003, doi: 10.2108/zsj.20.1043.

[63] S. Kwitny, A. V Klaus, and G. R. Hunnicutt, “The annulus of the mouse sperm tail is required to establish a membrane diffusion barrier that is engaged during the late steps of spermiogenesis.,” *Biol. Reprod.*, vol. 82, no. 4, pp. 669–78, Apr. 2010, doi: 10.1095/biolreprod.109.079566.

[64] T. G. Cooper, “The epididymis, cytoplasmic droplets and male fertility.,” *Asian J. Androl.*, vol. 13, no. 1, pp. 130–8, Jan. 2011, doi: 10.1038/aja.2010.97.

[65] P. Lishko, D. E. Clapham, B. Navarro, and Y. Kirichok, “Sperm patch-clamp.,” *Methods Enzymol.*, vol. 525, pp. 59–83, 2013, doi: 10.1016/B978-0-12-397944-5.00004-3.

[66] Y. Kirichok and P. V Lishko, “Rediscovering sperm ion channels with the patch-clamp technique.,” *Mol. Hum. Reprod.*, vol. 17, no. 8, pp. 478–99, Aug. 2011, doi: 10.1093/molehr/gar044.

[67] A. Touré, “Importance of slc26 transmembrane anion exchangers in sperm post-testicular maturation and fertilization potential,” *Frontiers in Cell and Developmental Biology*, vol. 7, no. OCT. Frontiers Media S.A., pp. 1–22, 2019, doi: 10.3389/fcell.2019.00230.

[68] P. V. Lishko, Y. Kirichok, D. Ren, B. Navarro, J. J. Chung, and D. E. Clapham, “The control of male fertility by spermatozoan ion channels,” *Annu. Rev. Physiol.*, vol. 74, pp. 453–475, 2012, doi: 10.1146/annurev-physiol-020911-153258.

[69] D. E. Clapham, “Calcium signaling.,” *Cell*, vol. 131, no. 6, pp. 1047–58, Dec. 2007, doi: 10.1016/j.cell.2007.11.028.

[70] F. Ardon, R. D. Markello, L. Hu, Z. I. Deutsch, C.-K. Tung, M. Wu, and S. S. Suarez, “Dynamics of Bovine Sperm Interaction with Epithelium Differ Between Oviductal Isthmus and Ampulla.,” *Biol. Reprod.*, vol. 95, no. 4, p. 90, Oct. 2016, doi: 10.1095/biolreprod.116.140632.

[71] S. S. Suarez, “Control of hyperactivation in sperm.,” *Hum. Reprod. Update*, vol. 14, no. 6,

9 References

pp. 647–57, doi: 10.1093/humupd/dmn029.

[72] C. M. Santi, A. Darszon, and A. Hernández-Cruz, “A dihydropyridine-sensitive T-type Ca²⁺ current is the main Ca²⁺ current carrier in mouse primary spermatocytes.,” *Am. J. Physiol.*, vol. 271, no. 5 Pt 1, pp. C1583-93, Nov. 1996.

[73] C. T. Beuckmann, C. M. Sinton, N. Miyamoto, M. Ino, and M. Yanagisawa, “N-type calcium channel alpha1B subunit (Cav2.2) knock-out mice display hyperactivity and vigilance state differences.,” *J. Neurosci.*, vol. 23, no. 17, pp. 6793–7, Jul. 2003.

[74] H. Saegusa, T. Kurihara, S. Zong, O. Minowa, A. Kazuno, W. Han, Y. Matsuda, H. Yamanaka, M. Osanai, T. Noda, and T. Tanabe, “Altered pain responses in mice lacking alpha 1E subunit of the voltage-dependent Ca²⁺ channel.,” *Proc. Natl. Acad. Sci. U. S. A.*, vol. 97, no. 11, pp. 6132–7, May 2000, doi: 10.1073/pnas.100124197.

[75] D. Kim, I. Song, S. Keum, T. Lee, M. J. Jeong, S. S. Kim, M. W. McEnery, and H. S. Shin, “Lack of the burst firing of thalamocortical relay neurons and resistance to absence seizures in mice lacking alpha(1G) T-type Ca(2+) channels.,” *Neuron*, vol. 31, no. 1, pp. 35–45, Jul. 2001.

[76] D. Ren, B. Navarro, G. Perez, A. C. Jackson, S. Hsu, Q. Shi, J. L. Tilly, and D. E. Clapham, “A sperm ion channel required for sperm motility and male fertility.,” *Nature*, vol. 413, no. 6856, pp. 603–9, Oct. 2001, doi: 10.1038/35098027.

[77] A. Loble, V. Pierron, L. Reynolds, L. Allen, and D. Michalovich, “Identification of human and mouse CatSper3 and CatSper4 genes: characterisation of a common interaction domain and evidence for expression in testis.,” *Reprod. Biol. Endocrinol.*, vol. 1, p. 53, Aug. 2003, doi: 10.1186/1477-7827-1-53.

[78] T. A. Quill, S. A. Sugden, K. L. Rossi, L. K. Doolittle, R. E. Hammer, and D. L. Garbers, “Hyperactivated sperm motility driven by CatSper2 is required for fertilization.,” *Proc. Natl. Acad. Sci. U. S. A.*, vol. 100, no. 25, pp. 14869–74, Dec. 2003, doi: 10.1073/pnas.2136654100.

[79] H. Qi, M. M. Moran, B. Navarro, J. A. Chong, G. Krapivinsky, L. Krapivinsky, Y. Kirichok, I. S. Ramsey, T. A. Quill, and D. E. Clapham, “All four CatSper ion channel proteins are required for male fertility and sperm cell hyperactivated motility,” *Proc. Natl. Acad. Sci.*, vol. 104, no. 4, pp. 1219–1223, 2007, doi: 10.1073/pnas.0610286104.

[80] J.-J. Chung, B. Navarro, G. Krapivinsky, L. Krapivinsky, and D. E. Clapham, “A novel gene required for male fertility and functional CATSPER channel formation in spermatozoa.,” *Nat. Commun.*, vol. 2, p. 153, Jan. 2011, doi: 10.1038/ncomms1153.

[81] J. J. Chung, K. Miki, D. Kim, S. H. Shim, H. F. Shi, J. Y. Hwang, X. Cai, Y. Iseri, X. Zhuang, and D. E. Clapham, “Catsper ζ regulates the structural continuity of sperm ca²⁺ signaling domains and is required for normal fertility,” *eLife*, vol. 6, Feb. 2017, doi: 10.7554/eLife.23082.

[82] J. Y. Hwang, N. Mannowetz, Y. Zhang, R. A. Everley, S. P. Gygi, J. Bewersdorf, P. V. Lishko, and J. J. Chung, “Dual Sensing of Physiologic pH and Calcium by EFCAB9 Regulates Sperm Motility,” *Cell*, vol. 177, no. 6, pp. 1480-1494.e19, May 2019, doi: 10.1016/j.cell.2019.03.047.

[83] N. Avidan, H. Tamary, O. Dgany, D. Cattan, A. Pariente, M. Thulliez, N. Borot, L. Moati, A. Barthelme, L. Salmon, T. Krasnov, E. Ben-Asher, T. Olander, M. Khen, I. Yaniv, R. Zaizov,

9 References

H. Shalev, J. Delaunay, M. Fellous, *et al.*, “CATSPER2, a human autosomal nonsyndromic male infertility gene.,” *Eur. J. Hum. Genet.*, vol. 11, no. 7, pp. 497–502, Jul. 2003, doi: 10.1038/sj.ejhg.5200991.

[84] Y. Kirichok, B. Navarro, and D. E. Clapham, “Whole-cell patch-clamp measurements of spermatozoa reveal an alkaline-activated Ca²⁺ channel.,” *Nature*, vol. 439, no. 7077, pp. 737–40, Feb. 2006, doi: 10.1038/nature04417.

[85] P. V. Lishko, I. L. Botchkina, A. Fedorenko, and Y. Kirichok, “Acid Extrusion from Human Spermatozoa Is Mediated by Flagellar Voltage-Gated Proton Channel,” *Cell*, vol. 140, no. 3, pp. 327–337, Feb. 2010, doi: 10.1016/j.cell.2009.12.053.

[86] T. Strünker, N. Goodwin, C. Brenker, N. D. Kashikar, I. Weyand, R. Seifert, and U. B. Kaupp, “The CatSper channel mediates progesterone-induced Ca²⁺ influx in human sperm.,” *Nature*, vol. 471, no. 7338, pp. 382–6, Mar. 2011, doi: 10.1038/nature09769.

[87] C. Brenker, N. Goodwin, I. Weyand, N. D. Kashikar, M. Naruse, M. Krähling, A. Müller, U. B. Kaupp, and T. Strünker, “The CatSper channel: a polymodal chemosensor in human sperm,” *EMBO J.*, vol. 31, no. 7, pp. 1654–1665, Apr. 2012, doi: 10.1038/emboj.2012.30.

[88] M. R. Miller, N. Mannowetz, A. T. Iavarone, R. Safavi, E. O. Gracheva, J. F. Smith, R. Z. Hill, D. M. Bautista, Y. Kirichok, and P. V. Lishko, “Unconventional endocannabinoid signaling governs sperm activation via sex hormone progesterone.,” *Science*, vol. 352, no. 6285, pp. 555–559, 2016, doi: 10.1126/science.aad6887.

[89] P. V. Lishko, I. L. Botchkina, and Y. Kirichok, “Progesterone activates the principal Ca²⁺ channel of human sperm.,” *Nature*, vol. 471, no. 7338, pp. 387–91, Mar. 2011, doi: 10.1038/nature09767.

[90] P. F. Blackmore, S. J. Beebe, D. R. Danforth, and N. Alexander, “Progesterone and 17 alpha-hydroxyprogesterone. Novel stimulators of calcium influx in human sperm.,” *J. Biol. Chem.*, vol. 265, no. 3, pp. 1376–80, Jan. 1990.

[91] A. Reyes-Fuentes and M. E. Chavarría-Olarte, “[Biochemical regulation of the acrosomal reaction in the mammalian spermatozoid],,” *Gac. médica México*, vol. 123, no. 11–12, pp. 261–7.

[92] H. Wang, L. L. McGoldrick, and J. J. Chung, “Sperm ion channels and transporters in male fertility and infertility,” *Nat. Rev. Urol.*, vol. 18, no. 1, pp. 46–66, 2021, doi: 10.1038/s41585-020-00390-9.

[93] J.-J. Chung, S.-H. Shim, R. A. Everley, S. P. Gygi, X. Zhuang, and D. E. Clapham, “Structurally Distinct Ca²⁺ Signaling Domains of Sperm Flagella Orchestrate Tyrosine Phosphorylation and Motility,” *Cell*, vol. 157, no. 4, pp. 808–822, May 2014, doi: 10.1016/j.cell.2014.02.056.

[94] S.-Y. Lee, J. A. Letts, and R. Mackinnon, “Dimeric subunit stoichiometry of the human voltage-dependent proton channel Hv1.,” *Proc. Natl. Acad. Sci. U. S. A.*, vol. 105, no. 22, pp. 7692–5, Jun. 2008, doi: 10.1073/pnas.0803277105.

[95] I. S. Ramsey, M. M. Moran, J. A. Chong, and D. E. Clapham, “A voltage-gated proton-selective channel lacking the pore domain.,” *Nature*, vol. 440, no. 7088, pp. 1213–6, Apr. 2006, doi: 10.1038/nature04700.

[96] M. L. Wood, E. V. Schow, J. A. Freites, S. H. White, F. Tombola, and D. J. Tobias, “Water wires in atomistic models of the Hv1 proton channel,” *Biochim. Biophys. Acta* -

9 References

Biomembr., vol. 1818, no. 2, pp. 286–293, Feb. 2012, doi: 10.1016/j.bbamem.2011.07.045.

[97] T. K. Berger, D. M. Fußhöller, N. Goodwin, W. Bönigk, A. Müller, N. Dokani Khesroshahi, C. Brenker, D. Wachten, E. Krause, U. B. Kaupp, and T. Strünker, “Post-translational cleavage of Hv1 in human sperm tunes pH- and voltage-dependent gating,” *J. Physiol.*, vol. 595, no. 5, pp. 1533–1546, Mar. 2017, doi: 10.1113/JP273189.

[98] C. Muñoz-Garay, J. L. De la Vega-Beltrán, R. Delgado, P. Labarca, R. Felix, and A. Darszon, “Inwardly Rectifying K⁺ Channels in Spermatogenic Cells: Functional Expression and Implication in Sperm Capacitation,” *Dev. Biol.*, vol. 234, no. 1, pp. 261–274, Jun. 2001, doi: 10.1006/dbio.2001.0196.

[99] N. Mannowetz, N. M. Naidoo, S. A. S. Choo, J. F. Smith, and P. V. Lishko, “Slo1 is the principal potassium channel of human spermatozoa,” *eLife*, vol. 2, p. e01009, 2013, doi: 10.7554/eLife.01009.

[100] C. Brenker, Y. Zhou, A. Müller, F. A. Echeverry, C. Trötschel, A. Poetsch, X.-M. Xia, W. Bönigk, C. J. Lingle, U. B. Kaupp, and T. Strünker, “The Ca²⁺ -activated K⁺ current of human sperm is mediated by Slo3,” *eLife*, vol. 3, no. 3, p. e01438, Mar. 2014, doi: 10.7554/eLife.01438.

[101] R. P. Demott and S. S. Suarez, “Hyperactivated sperm progress in the mouse oviduct,” *Biol. Reprod.*, vol. 46, no. 5, pp. 779–85, May 1992.

[102] M. R. Miller, S. A. Mansell, S. A. Meyers, and P. V. Lishko, “Flagellar ion channels of sperm: similarities and differences between species,” *Cell Calcium*, vol. 58, no. 1, 2015, doi: 10.1016/j.ceca.2014.10.009.

[103] N. Mundt, M. Spehr, and P. V. Lishko, “TRPV4 is the temperature-sensitive ion channel of human sperm,” *eLife*, vol. 7, Jul. 2018, doi: 10.7554/eLife.35853.

[104] K. C. Hoover, “Smell with inspiration: The evolutionary significance of olfaction,” *American Journal of Physical Anthropology*, vol. 143, no. SUPPL. 51. Am J Phys Anthropol, pp. 63–74, 2010, doi: 10.1002/ajpa.21441.

[105] L. Stowers and M. Spehr, “The Vomeronasal Organ,” in *Handbook of Olfaction and Gustation*, Hoboken, NJ, USA: John Wiley & Sons, Inc, 2015, pp. 1113–1132.

[106] L. Weiss, I. Manzini, and T. Hassenklöver, “Olfaction across the water–air interface in anuran amphibians,” *Cell and Tissue Research*, vol. 383, no. 1. Springer Science and Business Media Deutschland GmbH, 2021, doi: 10.1007/s00441-020-03377-5.

[107] H. L. Eisthen, “Evolution of vertebrate olfactory systems,” *Brain. Behav. Evol.*, vol. 50, no. 4, pp. 222–233, Jan. 1997, doi: 10.1159/000113336.

[108] G. Bertmar, “Evolution of Vomeronasal Organs in Vertebrates,” *Evolution (N. Y.)*, vol. 35, no. 2, pp. 359–366, Mar. 1981, doi: 10.1111/j.1558-5646.1981.tb04893.x.

[109] L. Silva and A. Antunes, “Vomeronasal Receptors in Vertebrates and the Evolution of Pheromone Detection,” *Annual Review of Animal Biosciences*, vol. 5. Annual Reviews Inc., pp. 353–370, Feb. 08, 2017, doi: 10.1146/annurev-animal-022516-022801.

[110] M. Andersson, *Sexual Selection*. Princeton Univ. Press, 1994.

[111] F. Zufall and S. D. Munger, “From odor and pheromone transduction to the organization of the sense of smell,” *Trends in Neurosciences*, vol. 24, no. 4. Elsevier Ltd, pp. 191–193, Apr. 01, 2001, doi: 10.1016/S0166-2236(00)01765-3.

9 References

- [112] H. Breer, J. Fleischer, and J. Strotmann, "The sense of smell: Multiple olfactory subsystems," in *Cellular and Molecular Life Sciences*, Jul. 2006, vol. 63, no. 13, pp. 1465–1475, doi: 10.1007/s00018-006-6108-5.
- [113] M. Ma, "Encoding olfactory signals via multiple chemosensory systems," *Critical Reviews in Biochemistry and Molecular Biology*, vol. 42, no. 6. Taylor & Francis, pp. 463–480, Nov. 2007, doi: 10.1080/10409230701693359.
- [114] S. D. Munger, T. Leinders-Zufall, and F. Zufall, "Subsystem organization of the mammalian sense of smell," *Annual Review of Physiology*, vol. 71. Annu Rev Physiol, pp. 115–140, Mar. 2009, doi: 10.1146/annurev.physiol.70.113006.100608.
- [115] H. Grüneberg, "A ganglion probably belonging to the N. terminalis system in the nasal mucosa of the mouse," *Z. Anat. Entwicklungsgesch.*, vol. 140, no. 1, pp. 39–52, Jan. 1973, doi: 10.1007/BF00520716.
- [116] Rodolfo-Masera and T., "Su l'esistenza di un particolare organo olfattivo nel setto nasale della cavia e di altri roditori," *Arch. Ital. Anat. Embriol.*, vol. 48, pp. 157–213, 1943.
- [117] F. Scalia and S. S. Winans, "The differential projections of the olfactory bulb and accessory olfactory bulb in mammals," *J. Comp. Neurol.*, vol. 161, no. 1, pp. 31–55, 1975, doi: 10.1002/cne.901610105.
- [118] D. Y. Lin, S. Z. Zhang, E. Block, and L. C. Katz, "Encoding social signals in the mouse main olfactory bulb," *Nature*, vol. 434, no. 7032, pp. 470–477, Mar. 2005, doi: 10.1038/nature03414.
- [119] F. Xu, M. Schaefer, I. Kida, J. Schafer, N. Liu, D. L. Rothman, F. Hyder, D. Restrepo, and G. M. Shepherd, "Simultaneous activation of mouse main and accessory olfactory bulbs by odors or pheromones," *J. Comp. Neurol.*, vol. 489, no. 4, pp. 491–500, Sep. 2005, doi: 10.1002/cne.20652.
- [120] P. A. Brennan and K. M. Kendrick, "Mammalian social odours: Attraction and individual recognition," *Philosophical Transactions of the Royal Society B: Biological Sciences*, vol. 361, no. 1476. Royal Society, pp. 2061–2078, Dec. 29, 2006, doi: 10.1098/rstb.2006.1931.
- [121] C. Dulac and S. Wagner, "Genetic Analysis of Brain Circuits Underlying Pheromone Signaling," *Annu. Rev. Genet.*, vol. 40, no. 1, pp. 449–467, Dec. 2006, doi: 10.1146/annurev.genet.39.073003.093937.
- [122] M. Spehr, K. R. Kelliher, X. H. Li, T. Boehm, T. Leinders-Zufall, and F. Zufall, "Essential role of the main olfactory system in social recognition of major histocompatibility complex peptide ligands," *J. Neurosci.*, vol. 26, no. 7, pp. 1961–1970, Feb. 2006, doi: 10.1523/JNEUROSCI.4939-05.2006.
- [123] M. Spehr, J. Spehr, K. Ukhanov, K. R. Kelliher, T. Leinders-Zufall, and F. Zufall, "Parallel processing of social signals by the mammalian main and accessory olfactory systems," in *Cellular and Molecular Life Sciences*, Jul. 2006, vol. 63, no. 13, pp. 1476–1484, doi: 10.1007/s00018-006-6109-4.
- [124] Z. Wang, C. B. Sindreu, V. Li, A. Nudelman, G. C. K. Chan, and D. R. Storm, "Pheromone detection in male mice depends on signaling through the type 3 adenylyl cyclase in the main olfactory epithelium," *J. Neurosci.*, vol. 26, no. 28, pp. 7375–7379, Jul. 2006, doi: 10.1523/JNEUROSCI.1967-06.2006.

9 References

- [125] R. Dooley, A. Mashukova, B. Toetter, H. Hatt, and E. M. Neuhaus, "Purinergic receptor antagonists inhibit odorant-mediated CREB phosphorylation in sustentacular cells of mouse olfactory epithelium," *BMC Neurosci.*, vol. 12, no. 1, p. 86, Aug. 2011, doi: 10.1186/1471-2202-12-86.
- [126] D. G. Moulton and L. M. Beidler, "Structure and function in the peripheral olfactory system," *Physiological reviews*, vol. 47, no. 1. Physiol Rev, pp. 1–52, 1967, doi: 10.1152/physrev.1967.47.1.1.
- [127] P. Mombaerts, F. Wang, C. Dulac, S. K. Chao, A. Nemes, M. Mendelsohn, J. Edmondson, and R. Axel, "Visualizing an olfactory sensory map," *Cell*, vol. 87, no. 4, pp. 675–686, Jan. 1996, doi: 10.1016/S0092-8674(00)81387-2.
- [128] S. Serizawa, K. Miyamichi, H. Takeuchi, Y. Yamagishi, M. Suzuki, and H. Sakano, "A Neuronal Identity Code for the Odorant Receptor-Specific and Activity-Dependent Axon Sorting," *Cell*, vol. 127, no. 5, pp. 1057–1069, Dec. 2006, doi: 10.1016/j.cell.2006.10.031.
- [129] T. Imai and H. Sakano, "Roles of odorant receptors in projecting axons in the mouse olfactory system," *Current Opinion in Neurobiology*, vol. 17, no. 5. Elsevier Current Trends, pp. 507–515, Oct. 01, 2007, doi: 10.1016/j.conb.2007.08.002.
- [130] J. Strotmann, S. Conzelmann, A. Beck, P. Feinstein, H. Breer, and P. Mombaerts, "Local permutations in the glomerular array of the mouse olfactory bulb," *J. Neurosci.*, vol. 20, no. 18, pp. 6927–6938, Sep. 2000, doi: 10.1523/jneurosci.20-18-06927.2000.
- [131] M. T. Shipley and M. Ennis, "Functional organization of olfactory system," *Journal of Neurobiology*, vol. 30, no. 1. J Neurobiol, pp. 123–176, May 1996, doi: 10.1002/(SICI)1097-4695(199605)30:1<123::AID-NEU11>3.0.CO;2-N.
- [132] N. E. Schoppa and N. N. Urban, "Dendritic processing within olfactory bulb circuits," *Trends in Neurosciences*, vol. 26, no. 9. Elsevier Ltd, pp. 501–506, Sep. 01, 2003, doi: 10.1016/S0166-2236(03)00228-5.
- [133] S. Ghosh, S. D. Larson, H. Hefzi, Z. Marnoy, T. Cutforth, K. Dokka, and K. K. Baldwin, "Sensory maps in the olfactory cortex defined by long-range viral tracing of single neurons," *Nature*, vol. 472, no. 7342, pp. 217–222, Apr. 2011, doi: 10.1038/nature09945.
- [134] K. Miyamichi, F. Amat, F. Moussavi, C. Wang, I. Wickersham, N. R. Wall, H. Taniguchi, B. Tasic, Z. J. Huang, Z. He, E. M. Callaway, M. A. Horowitz, and L. Luo, "Cortical representations of olfactory input by trans-synaptic tracing," *Nature*, vol. 472, no. 7342, pp. 191–199, Apr. 2011, doi: 10.1038/nature09714.
- [135] D. L. Sosulski, M. Lissitsyna Bloom, T. Cutforth, R. Axel, and S. R. Datta, "Distinct representations of olfactory information in different cortical centres," *Nature*, vol. 472, no. 7342, pp. 213–219, Apr. 2011, doi: 10.1038/nature09868.
- [136] T. D. Wyatt, *Pheromones and Animal Behavior: Chemical signals and signatures*, 2nd ed. Cambridge University Press., 2014.
- [137] A. W. Kaur, T. Ackels, T. H. Kuo, A. Cichy, S. Dey, C. Hays, M. Kateri, D. W. Logan, T. F. Marton, M. Spehr, and L. Stowers, "Murine pheromone proteins constitute a context-dependent combinatorial code governing multiple social behaviors," *Cell*, vol. 157, no. 3, pp. 676–688, Apr. 2014, doi: 10.1016/j.cell.2014.02.025.
- [138] J. Mohrhardt, M. Nagel, D. Fleck, Y. Ben-Shaul, and M. Spehr, "Signal detection and

9 References

coding in the accessory olfactory system," *Chem. Senses*, vol. 43, no. 9, pp. 667–695, 2018, doi: 10.1093/chemse/bjy061.

[139] P. Karlson and M. Lüscher, "'Pheromones': A new term for a class of biologically active substances," *Nature*, vol. 183, no. 4653, pp. 55–56, 1959, doi: 10.1038/183055a0.

[140] D. Trotier and K. B. Døving, "'Anatomical Description of a New Organ in the Nose of Domesticated Animals' by Ludvig Jacobson (1813)," *Chem. Senses*, vol. 23, no. 6, pp. 743–754, 1998, doi: 10.1093/chemse/23.6.743.

[141] M. Meredith, "Sensory processing in the main and accessory olfactory systems: Comparisons and contrasts," *J. Steroid Biochem. Mol. Biol.*, vol. 39, no. 4 PART 2, pp. 601–614, 1991, doi: 10.1016/0960-0760(91)90258-7.

[142] M. Halpern and A. Martínez-Marcos, "Structure and function of the vomeronasal system: An update," *Progress in Neurobiology*, vol. 70, no. 3. Elsevier Ltd, pp. 245–318, 2003, doi: 10.1016/S0301-0082(03)00103-5.

[143] M. Meredith, D. M. Marques, R. J. O'Connell, and F. L. Stern, "Vomeronasal pump: Significance for male hamster sexual behavior," *Science (80-.)*, vol. 207, no. 4436, pp. 1224–1226, 1980, doi: 10.1126/science.7355286.

[144] M. Meredith, "Chronic recording of vomeronasal pump activation in awake behaving hamsters," *Physiol. Behav.*, vol. 56, no. 2, pp. 345–354, Aug. 1994, doi: 10.1016/0031-9384(94)90205-4.

[145] K. C. P. Wilson and G. Raisman, "Age-related changes in the neurosensory epithelium of the mouse vomeronasal organ: Extended period of post-natal growth in size and evidence for rapid cell turnover in the adult," *Brain Res.*, vol. 185, no. 1, pp. 103–113, Mar. 1980, doi: 10.1016/0006-8993(80)90675-7.

[146] V. Ghiaroni, F. Fieni, R. Tirindelli, P. Pietra, and A. Bigiani, "Ion conductances in supporting cells isolated from the mouse vomeronasal organ," *J. Neurophysiol.*, vol. 89, no. 1, pp. 118–127, Jan. 2003, doi: 10.1152/jn.00545.2002.

[147] L. Belluscio, G. Koentges, R. Axel, and C. Dulac, "A map of pheromone receptor activation in the mammalian brain," *Cell*, vol. 97, no. 2, pp. 209–220, Apr. 1999, doi: 10.1016/S0092-8674(00)80731-X.

[148] I. Rodriguez, P. Feinstein, and P. Mombaerts, "Variable patterns of axonal projections of sensory neurons in the mouse vomeronasal system," *Cell*, vol. 97, no. 2, pp. 199–208, Apr. 1999, doi: 10.1016/S0092-8674(00)80730-8.

[149] C. Dulac and A. T. Torello, "Molecular detection of pheromone signals in mammals: From genes to behaviour," *Nat. Rev. Neurosci.*, vol. 4, no. 7, pp. 551–562, 2003, doi: 10.1038/nrn1140.

[150] J. F. Bellringer, P. M. Hester Pratt, and E. B. Keverne, "Involvement of the vomeronasal organ and prolactin in pheromonal induction of delayed implantation in mice," *J. Reprod. Fertil.*, vol. 59, no. 1, pp. 223–228, 1980, doi: 10.1530/jrf.0.0590223.

[151] M. Halpern and N. Frumin, "Roles of the vomeronasal and olfactory systems in prey attack and feeding in adult garter snakes," *Physiol. Behav.*, vol. 22, no. 6, pp. 1183–1189, Jun. 1979, doi: 10.1016/0031-9384(79)90274-9.

[152] Y. Isogai, S. Si, L. Pont-Lezica, T. Tan, V. Kapoor, V. N. Murthy, and C. Dulac, "Molecular organization of vomeronasal chemoreception," *Nature*, vol. 478, no. 7368, pp. 241–245,

9 References

Oct. 2011, doi: 10.1038/nature10437.

[153] T. D. Wyatt, "Fifty years of pheromones," *Nature*, vol. 457, no. 7227. Nature, pp. 262–263, Jan. 15, 2009, doi: 10.1038/457262a.

[154] P. S. Xu, D. Lee, and T. E. Holy, "Experience-Dependent Plasticity Drives Individual Differences in Pheromone-Sensing Neurons," *Neuron*, vol. 91, no. 4, pp. 878–892, Aug. 2016, doi: 10.1016/j.neuron.2016.07.034.

[155] S. A. Roberts, A. J. Davidson, L. McLean, R. J. Beynon, and J. L. Hurst, "Pheromonal induction of spatial learning in mice," *Science (80-.)*, vol. 338, no. 6113, pp. 1462–1465, Dec. 2012, doi: 10.1126/science.1225638.

[156] R. L. Doty, *The Great Pheromone Myth* | Johns Hopkins University Press Books. The Johns Hopkins University Press., 2010.

[157] M. Novotny, B. Jemiolo, S. Harvey, D. Wiesler, and A. Marchlewska-Koj, "Adrenal-mediated endogenous metabolites inhibit puberty in female mice," *Science (80-.)*, vol. 231, no. 4739, pp. 722–725, 1986, doi: 10.1126/science.3945805.

[158] M. V. Novotny, W. Ma, D. Wiesler, and L. Žídek, "Positive identification of the puberty-accelerating pheromone of the house mouse: The volatile ligands associating with the major urinary protein," *Proc. R. Soc. B Biol. Sci.*, vol. 266, no. 1432, pp. 2017–2022, Oct. 1999, doi: 10.1098/rspb.1999.0880.

[159] H. Kimoto, S. Haga, K. Sato, and K. Touhara, "Sex-specific peptides from exocrine glands stimulate mouse vomeronasal sensory neurons," *Nature*, vol. 437, no. 7060, pp. 898–901, Oct. 2005, doi: 10.1038/nature04033.

[160] D. M. Ferrero, L. M. Moeller, T. Osakada, N. Horio, Q. Li, D. S. Roy, A. Cichy, M. Spehr, K. Touhara, and S. D. Liberles, "A juvenile mouse pheromone inhibits sexual behaviour through the vomeronasal system," *Nature*, vol. 502, no. 7471, pp. 368–371, 2013, doi: 10.1038/nature12579.

[161] T. Leinders-Zufall, A. P. Lane, A. C. Puche, W. Ma, M. V. Novotny, M. T. Shipley, and F. Zufall, "Ultrasensitive pheromone detection by mammalian vomeronasal neurons," *Nature*, vol. 405, no. 6788, pp. 792–796, Jun. 2000, doi: 10.1038/35015572.

[162] A. Cavaggioni and C. Mucignat-Caretta, "Major urinary proteins, α (2U)-globulins and aphrodisin," *Biochimica et Biophysica Acta - Protein Structure and Molecular Enzymology*, vol. 1482, no. 1–2. Biochim Biophys Acta, pp. 218–228, Oct. 18, 2000, doi: 10.1016/S0167-4838(00)00149-7.

[163] S. A. Cheetham, M. D. Thom, F. Jury, W. E. R. Ollier, R. J. Beynon, and J. L. Hurst, "The Genetic Basis of Individual-Recognition Signals in the Mouse," *Curr. Biol.*, vol. 17, no. 20, pp. 1771–1777, Oct. 2007, doi: 10.1016/j.cub.2007.10.007.

[164] D. W. Logan, T. F. Marton, and L. Stowers, "Species Specificity in Major Urinary Proteins by Parallel Evolution," *PLoS One*, vol. 3, no. 9, p. e3280, Sep. 2008, doi: 10.1371/journal.pone.0003280.

[165] R. J. Beynon, J. L. Hurst, S. J. Gaskell, S. J. Hubbard, R. E. Humphries, N. Malone, A. D. Marie, L. Martinsen, C. M. Nevison, C. E. Payne, D. H. L. Robertson, and C. Veggerby, "Mice, Mups and Myths: Structure-Function Relationships of the Major Urinary Proteins," in *Chemical Signals in Vertebrates 9*, Springer US, 2001, pp. 149–156.

[166] S. D. Armstrong, D. H. L. Robertson, S. A. Cheetham, J. L. Hurst, and R. J. Beynon,

9 References

“Structural and functional differences in isoforms of mouse major urinary proteins: A male-specific protein that preferentially binds a male pheromone,” *Biochem. J.*, vol. 391, no. 2, pp. 343–350, Oct. 2005, doi: 10.1042/BJ20050404.

[167] F. Nodari, F. F. Hsu, X. Fu, T. F. Holekamp, L. F. Kao, J. Turk, and T. E. Holy, “Sulfated steroids as natural ligands of mouse pheromone-sensing neurons,” *J. Neurosci.*, vol. 28, no. 25, pp. 6407–6418, Jun. 2008, doi: 10.1523/JNEUROSCI.1425-08.2008.

[168] T. Sturm, T. Leinders-Zufall, B. MačEk, M. Walzer, S. Jung, B. Pö默merl, S. Stevanović, F. Zufall, P. Overath, and H. G. Rammensee, “Mouse urinary peptides provide a molecular basis for genotype discrimination by nasal sensory neurons,” *Nat. Commun.*, vol. 4, no. 1, pp. 1–10, Mar. 2013, doi: 10.1038/ncomms2610.

[169] P. Overath, T. Sturm, and H. G. Rammensee, “Of volatiles and peptides: In search for MHC-dependent olfactory signals in social communication,” *Cellular and Molecular Life Sciences*, vol. 71, no. 13. Birkhauser Verlag AG, pp. 2429–2442, Jul. 01, 2014, doi: 10.1007/s00018-014-1559-6.

[170] M. Černá, B. Kuntová, P. Talacko, R. Stopková, and P. Stopka, “Differential regulation of vaginal lipocalins (OBP, MUP) during the estrous cycle of the house mouse,” *Sci. Rep.*, vol. 7, no. 1, pp. 1–10, Dec. 2017, doi: 10.1038/s41598-017-12021-2.

[171] D. W. Logan, “The complexity of pheromone-mediated behaviour in mammals,” *Current Opinion in Behavioral Sciences*, vol. 2, no. 2. Elsevier Ltd, pp. 96–101, Apr. 01, 2015, doi: 10.1016/j.cobeha.2014.10.011.

[172] J. M. Mudge, S. D. Armstrong, K. McLaren, R. J. Beynon, J. L. Hurst, C. Nicholson, D. H. Robertson, L. G. Wilming, and J. L. Harrow, “Dynamic instability of the major urinary protein gene family revealed by genomic and phenotypic comparisons between C57 and 129 strain mice,” *Genome Biol.*, vol. 9, no. 5, May 2008, doi: 10.1186/gb-2008-9-5-r91.

[173] J. L. Hurst and R. J. Beynon, “Scent wars: The chemobiology of competitive signalling in mice,” *BioEssays*, vol. 26, no. 12. Bioessays, pp. 1288–1298, Dec. 2004, doi: 10.1002/bies.20147.

[174] D. H. L. Robertson, J. L. Hurst, M. S. Bolgar, S. J. Gaskell, and R. J. Beynon, “Molecular Heterogeneity of Urinary Proteins in Wild House Mouse Populations,” *Rapid Commun. Mass Spectrom.*, vol. 11, no. 7, pp. 786–790, Apr. 1997, doi: 10.1002/(SICI)1097-0231(19970422)11:7<786::AID-RCM876>3.0.CO;2-8.

[175] S. A. Roberts, D. M. Simpson, S. D. Armstrong, A. J. Davidson, D. H. Robertson, L. McLean, R. J. Beynon, and J. L. Hurst, “Darcin: A male pheromone that stimulates female memory and sexual attraction to an individual male’s odour,” *BMC Biol.*, vol. 8, Jun. 2010, doi: 10.1186/1741-7007-8-75.

[176] P. Chamero, T. F. Marton, D. W. Logan, K. Flanagan, J. R. Cruz, A. Saghatelian, B. F. Cravatt, and L. Stowers, “Identification of protein pheromones that promote aggressive behaviour,” *Nature*, vol. 450, no. 7171, pp. 899–902, Dec. 2007, doi: 10.1038/nature05997.

[177] E. Hoffman, L. Pickavance, T. Thippeswamy, R. J. Beynon, and J. L. Hurst, “The male sex pheromone darcin stimulates hippocampal neurogenesis and cell proliferation in the subventricular zone in female mice,” *Front. Behav. Neurosci.*, vol. 9, no. APR, p. 106, Apr. 2015, doi: 10.3389/fnbeh.2015.00106.

9 References

[178] S. Haga, T. Hattori, T. Sato, K. Sato, S. Matsuda, R. Kobayakawa, H. Sakano, Y. Yoshihara, T. Kikusui, and K. Touhara, “The male mouse pheromone ESP1 enhances female sexual receptive behaviour through a specific vomeronasal receptor,” *Nature*, vol. 466, no. 7302, pp. 118–122, Jul. 2010, doi: 10.1038/nature09142.

[179] K. K. Ishii, T. Osakada, H. Mori, N. Miyasaka, Y. Yoshihara, K. Miyamichi, and K. Touhara, “A Labeled-Line Neural Circuit for Pheromone-Mediated Sexual Behaviors in Mice,” *Neuron*, vol. 95, no. 1, pp. 123–137.e8, Jul. 2017, doi: 10.1016/j.neuron.2017.05.038.

[180] T. Osakada, K. K. Ishii, H. Mori, R. Eguchi, D. M. Ferrero, Y. Yoshihara, S. D. Liberles, K. Miyamichi, and K. Touhara, “Sexual rejection via a vomeronasal receptor-triggered limbic circuit,” *Nat. Commun.*, vol. 9, no. 1, pp. 1–15, Dec. 2018, doi: 10.1038/s41467-018-07003-5.

[181] J. H. Brann, J. C. Dennis, E. E. Morrison, and D. A. Fadool, “Type-specific inositol 1,4,5-trisphosphate receptor localization in the vomeronasal organ and its interaction with a transient receptor potential channel, TRPC2,” *J. Neurochem.*, vol. 83, no. 6, pp. 1452–1460, Dec. 2002, doi: 10.1046/j.1471-4159.2002.01266.x.

[182] M. Spehr, H. Hatt, and C. H. Wetzel, “Arachidonic acid plays a role in rat vomeronasal signal transduction,” *J. Neurosci.*, vol. 22, no. 19, pp. 8429–8437, Oct. 2002, doi: 10.1523/jneurosci.22-19-08429.2002.

[183] P. Lucas, K. Ukhanov, T. Leinders-Zufall, and F. Zufall, “A diacylglycerol-gated cation channel in vomeronasal neuron dendrites is impaired in TRPC2 mutant mice: Mechanism of pheromone transduction,” *Neuron*, vol. 40, no. 3, pp. 551–561, Oct. 2003, doi: 10.1016/S0896-6273(03)00675-5.

[184] P. Chamero, T. Leinders-Zufall, and F. Zufall, “From genes to social communication: Molecular sensing by the vomeronasal organ,” *Trends in Neurosciences*, vol. 35, no. 10. Trends Neurosci, pp. 597–606, Oct. 2012, doi: 10.1016/j.tins.2012.04.011.

[185] I. Rodriguez, K. Del Punta, A. Rothman, T. Ishii, and P. Mombaerts, “Multiple new and isolated families within the mouse superfamily of V1r vomeronasal receptors,” *Nat. Neurosci.*, vol. 5, no. 2, pp. 134–140, 2002, doi: 10.1038/nn795.

[186] D. Roppolo, S. Vollery, C.-D. Kan, C. Lüscher, M.-C. Broillet, and I. Rodriguez, “Gene cluster lock after pheromone receptor gene choice,” *EMBO J.*, vol. 26, no. 14, pp. 3423–3430, Jul. 2007, doi: 10.1038/sj.emboj.7601782.

[187] J. M. Young and B. J. Trask, “V2R gene families degenerated in primates, dog and cow, but expanded in opossum,” *Trends in Genetics*, vol. 23, no. 5. pp. 212–215, May 2007, doi: 10.1016/j.tig.2007.03.004.

[188] S. D. Liberles, L. F. Horowitz, D. Kuang, J. J. Contos, K. L. Wilson, J. Siltberg-Liberles, D. A. Liberles, and L. B. Buck, “Formyl peptide receptors are candidate chemosensory receptors in the vomeronasal organ,” *Proc. Natl. Acad. Sci. U. S. A.*, vol. 106, no. 24, pp. 9842–9847, Jun. 2009, doi: 10.1073/pnas.0904464106.

[189] S. Rivière, L. Challet, D. Fluegge, M. Spehr, and I. Rodriguez, “Formyl peptide receptor-like proteins are a novel family of vomeronasal chemosensors,” *Nature*, vol. 459, no. 7246, pp. 574–577, May 2009, doi: 10.1038/nature08029.

[190] M. Halpern, L. S. Shapiro, and C. Jia, “Differential localization of G proteins in the opossum vomeronasal system,” *Brain Res.*, vol. 677, no. 1, pp. 157–161, Apr. 1995, doi:

9 References

10.1016/0006-8993(95)00159-N.

[191] P. Chamero, V. Katsoulidou, P. Hendrix, B. Bufe, R. Roberts, H. Matsunami, J. Abramowitz, L. Birnbaumer, F. Zufall, and T. Leinders-Zufall, "G protein Gao is essential for vomeronasal function and aggressive behavior in mice," *Proc. Natl. Acad. Sci. U. S. A.*, vol. 108, no. 31, pp. 12898–12903, Aug. 2011, doi: 10.1073/pnas.1107770108.

[192] A. Berghard and L. B. Buck, "Sensory transduction in vomeronasal neurons: Evidence for Gao, Gai2, and adenylyl cyclase II as major components of a pheromone signaling cascade," *J. Neurosci.*, vol. 16, no. 3, pp. 909–918, Feb. 1996, doi: 10.1523/jneurosci.16-03-00909.1996.

[193] C. Dulac and R. Axel, "A novel family of genes encoding putative pheromone receptors in mammals," *Cell*, vol. 83, no. 2, pp. 195–206, Oct. 1995, doi: 10.1016/0092-8674(95)90161-2.

[194] G. Herrada and C. Dulac, "A novel family of putative pheromone receptors in mammals with a topographically organized and sexually dimorphic distribution," *Cell*, vol. 90, no. 4, pp. 763–773, Aug. 1997, doi: 10.1016/S0092-8674(00)80536-X.

[195] T. E. Holy, C. Dulac, and M. Meister, "Responses of vomeronasal neurons to natural stimuli," *Science (80-)*, vol. 289, no. 5484, pp. 1569–1572, Sep. 2000, doi: 10.1126/science.289.5484.1569.

[196] J. Krieger, A. Schmitt, D. Löbel, T. Gudermann, G. Schultz, H. Breer, and I. Boekhoff, "Selective activation of G protein subtypes in the vomeronasal organ upon stimulation with urine-derived compounds," *J. Biol. Chem.*, vol. 274, no. 8, pp. 4655–4662, Feb. 1999, doi: 10.1074/jbc.274.8.4655.

[197] C. Yang and R. J. Delay, "Calcium-activated chloride current amplifies the response to urine in mouse vomeronasal sensory neurons," *J. Gen. Physiol.*, vol. 135, no. 1, pp. 3–13, Jan. 2010, doi: 10.1085/jgp.200910265.

[198] S. Kim, L. Ma, and C. R. Yu, "Requirement of calcium-activated chloride channels in the activation of mouse vomeronasal neurons," *Nat. Commun.*, vol. 2, no. 1, pp. 1–7, Jun. 2011, doi: 10.1038/ncomms1368.

[199] M. Dibattista, A. Amjad, D. K. Maurya, C. Sagheedu, G. Montani, R. Tirindelli, and A. Menini, "Calcium-activated chloride channels in the apical region of mouse vomeronasal sensory neurons," *J. Gen. Physiol.*, vol. 140, no. 1, pp. 3–15, Jul. 2012, doi: 10.1085/jgp.201210780.

[200] S. Hagendorf, D. Fluegge, C. Engelhardt, and M. Spehr, "Homeostatic control of sensory output in basal vomeronasal neurons: Activity-dependent expression of ether-à-go-go-related gene potassium channels," *J. Neurosci.*, vol. 29, no. 1, pp. 206–221, Jan. 2009, doi: 10.1523/JNEUROSCI.3656-08.2009.

[201] E. R. Liman and D. P. Corey, "Electrophysiological characterization of chemosensory neurons from the mouse vomeronasal organ," *J. Neurosci.*, vol. 16, no. 15, pp. 4625–4637, Aug. 1996, doi: 10.1523/jneurosci.16-15-04625.1996.

[202] R. Shimazaki, "Electrophysiological Properties and Modeling of Murine Vomeronasal Sensory Neurons in Acute Slice Preparations," *Chem. Senses*, vol. 31, no. 5, pp. 425–435, Mar. 2006, doi: 10.1093/chemse/bjj047.

[203] J. Spehr, S. Hagendorf, J. Weiss, M. Spehr, T. Leinders-Zufall, and F. Zufall, "Ca 2-

9 References

Calmodulin Feedback Mediates Sensory Adaptation and Inhibits Pheromone-Sensitive Ion Channels in the Vomeronasal Organ," 2009, doi: 10.1523/JNEUROSCI.5416-08.2009.

[204] E. Quaglino, M. Giustetto, P. Panzanelli, D. Cantino, A. Fasolo, and M. Sasso-Pognetto, "Immunocytochemical localization of glutamate and γ -aminobutyric acid in the accessory olfactory bulb of the rat," *J. Comp. Neurol.*, vol. 408, no. 1, pp. 61–72, May 1999, doi: 10.1002/(SICI)1096-9861(19990524)408:1<61::AID-CNE5>3.0.CO;2-F.

[205] K. Del Punta, A. Puche, N. C. Adams, I. Rodriguez, and P. Mombaerts, "A divergent pattern of sensory axonal projections is rendered convergent by second-order neurons in the accessory olfactory bulb," *Neuron*, vol. 35, no. 6, pp. 1057–1066, Sep. 2002, doi: 10.1016/S0896-6273(02)00904-2.

[206] S. Wagner, A. L. Gresser, A. T. Torello, and C. Dulac, "A Multireceptor Genetic Approach Uncovers an Ordered Integration of VNO Sensory Inputs in the Accessory Olfactory Bulb," *Neuron*, vol. 50, no. 5, pp. 697–709, Jun. 2006, doi: 10.1016/j.neuron.2006.04.033.

[207] J. Larriva-Sahd, "The accessory olfactory bulb in the adult rat: A cytological study of its cell types, neuropil, neuronal modules, and interactions with the main olfactory system," *J. Comp. Neurol.*, vol. 510, no. 3, pp. 309–350, Sep. 2008, doi: 10.1002/cne.21790.

[208] S. Takami and P. P. C. Graziadei, "Morphological complexity of the glomerulus in the rat accessory olfactory bulb-a Golgi study," *Brain Res.*, vol. 510, no. 2, pp. 339–342, Mar. 1990, doi: 10.1016/0006-8993(90)91387-V.

[209] S. Takami and P. P. C. Graziadei, "Light microscopic golgi study of mitral/tufted cells in the accessory olfactory bulb of the adult rat," *J. Comp. Neurol.*, vol. 311, no. 1, pp. 65–83, 1991, doi: 10.1002/cne.903110106.

[210] J. B. Castro, K. R. Hovis, and N. N. Urban, "Recurrent dendrodendritic inhibition of accessory olfactory bulb mitral cells requires activation of group I metabotropic glutamate receptors," *J. Neurosci.*, vol. 27, no. 21, pp. 5664–5671, May 2007, doi: 10.1523/JNEUROSCI.0613-07.2007.

[211] C. Jia, W. R. Chen, and G. M. Shepherd, "Synaptic organization and neurotransmitters in the rat accessory olfactory bulb," *J. Neurophysiol.*, vol. 81, no. 1, pp. 345–355, 1999, doi: 10.1152/jn.1999.81.1.345.

[212] M. Taniguchi and H. Kaba, "Properties of reciprocal synapses in the mouse accessory olfactory bulb," *Neuroscience*, vol. 108, no. 3, pp. 365–370, Dec. 2001, doi: 10.1016/S0306-4522(01)00427-4.

[213] M. Gorin, C. Tsitoura, A. Kahan, K. Watznauer, D. R. Drose, M. Arts, R. Mathar, S. O'Connor, I. L. Hanganu-Opatz, Y. Ben-Shaul, and M. Spehr, "Interdependent Conductances Drive Infraslow Intrinsic Rhythmogenesis in a Subset of Accessory Olfactory Bulb Projection Neurons," *J. Neurosci.*, vol. 36, no. 11, pp. 3127–44, Mar. 2016, doi: 10.1523/JNEUROSCI.2520-15.2016.

[214] C. Tsitoura, S. T. Malinowski, J. Mohrhardt, R. Degen, B. T. DiBenedictis, Y. Gao, K. Watznauer, K. Gerhold, M. Nagel, M. Weber, M. Rothermel, I. L. Hanganu-Opatz, Y. Ben-Shaul, I. G. Davison, and M. Spehr, "Synchronous infra-slow oscillations organize ensembles of accessory olfactory bulb projection neurons into distinct microcircuits," *J. Neurosci.*, vol. 40, no. 21, pp. 4203–4218, May 2020, doi: 10.1523/JNEUROSCI.2925-

9 References

19.2020.

- [215] A. Zylbertal, Y. Yarom, and S. Wagner, "Synchronous infra-slow bursting in the mouse accessory olfactory bulb emerge from interplay between intrinsic neuronal dynamics and network connectivity," *J. Neurosci.*, vol. 37, no. 10, pp. 2656–2672, Mar. 2017, doi: 10.1523/JNEUROSCI.3107-16.2017.
- [216] A. Martinez-Marcos, "On the organization of olfactory and vomeronasal cortices," *Progress in Neurobiology*, vol. 87, no. 1. Prog Neurobiol, pp. 21–30, Jan. 12, 2009, doi: 10.1016/j.pneurobio.2008.09.010.
- [217] N. Gutiérrez-Castellanos, C. Pardo-Bellver, F. Martínez-García, and E. Lanuza, "The vomeronasal cortex - afferent and efferent projections of the posteromedial cortical nucleus of the amygdala in mice," *Eur. J. Neurosci.*, vol. 39, no. 1, pp. 141–158, Jan. 2014, doi: 10.1111/ejn.12393.
- [218] L. Stowers and S. D. Liberles, "State-dependent responses to sex pheromones in mouse," *Current Opinion in Neurobiology*, vol. 38. Elsevier Ltd, pp. 74–79, Jun. 01, 2016, doi: 10.1016/j.conb.2016.04.001.
- [219] A. Mohedano-Moriano, P. Pro-Sistiaga, I. Ubeda-Bañon, C. De La Rosa-Prieto, D. Saiz-Sánchez, and A. Martinez-Marcos, "VIR and V2R segregated vomeronasal pathways to the hypothalamus," *Neuroreport*, vol. 19, no. 16, pp. 1623–1626, Oct. 2008, doi: 10.1097/WNR.0b013e328314b8d4.
- [220] G. A. Kevetter and S. S. Winans, "Connections of the corticomedial amygdala in the golden hamster. II. Efferents of the 'olfactory amygdala,'" *J. Comp. Neurol.*, vol. 197, no. 1, pp. 99–111, 1981, doi: 10.1002/cne.901970108.
- [221] G. D. Petrovich, N. S. Canteras, and L. W. Swanson, "Combinatorial amygdalar inputs to hippocampal domains and hypothalamic behavior systems," *Brain Research Reviews*, vol. 38, no. 1–2. Brain Res Brain Res Rev, pp. 247–289, 2001, doi: 10.1016/S0165-0173(01)00080-7.
- [222] U. Boehm, Z. Zou, and L. B. Buck, "Feedback loops link odor and pheromone signaling with reproduction," *Cell*, vol. 123, no. 4, pp. 683–695, Nov. 2005, doi: 10.1016/j.cell.2005.09.027.
- [223] C. A. Moffatt, "Steroid hormone modulation of olfactory processing in the context of socio-sexual behaviors in rodents and humans," *Brain Research Reviews*, vol. 43, no. 2. Elsevier, pp. 192–206, Oct. 01, 2003, doi: 10.1016/S0165-0173(03)00208-X.
- [224] H. Yoon, L. W. Enquist, and C. Dulac, "Olfactory inputs to hypothalamic neurons controlling reproduction and fertility," *Cell*, vol. 123, no. 4, pp. 669–682, Nov. 2005, doi: 10.1016/j.cell.2005.08.039.
- [225] P. A. Brennan and E. B. Keverne, "Neural mechanisms of mammalian olfactory learning," *Prog. Neurobiol.*, vol. 51, no. 4, pp. 457–481, 1997, doi: 10.1016/S0301-0082(96)00069-X.
- [226] C. F. Yang and N. M. Shah, "Representing sex in the brain, one module at a time," *Neuron*, vol. 82, no. 2. Cell Press, pp. 261–278, Apr. 16, 2014, doi: 10.1016/j.neuron.2014.03.029.
- [227] R. D. Broadwell and D. M. Jacobowitz, "Olfactory relationships of the telencephalon and diencephalon in the rabbit. III. The ipsilateral centrifugal fibers to the olfactory bulbar and retrobulbar formations," *J. Comp. Neurol.*, vol. 170, no. 3, pp. 321–345, 1976, doi:

9 References

10.1002/cne.901700305.

[228] S. Fan and M. Luo, "The organization of feedback projections in a pathway important for processing pheromonal signals," *Neuroscience*, vol. 161, no. 2, pp. 489–500, Jun. 2009, doi: 10.1016/j.neuroscience.2009.03.065.

[229] R. S. Smith and R. C. Araneda, "Cholinergic modulation of neuronal excitability in the accessory olfactory bulb," *J. Neurophysiol.*, vol. 104, no. 6, pp. 2963–2974, Dec. 2010, doi: 10.1152/jn.00446.2010.

[230] L. Oboti, E. Russo, T. Tran, D. Durstewitz, and J. G. Corbin, "Amygdala corticofugal input shapes mitral cell responses in the accessory olfactory bulb," *eNeuro*, vol. 5, no. 3, May 2018, doi: 10.1523/ENEURO.0175-18.2018.

[231] A. Agarwal, A. Mulgund, A. Hamada, and M. R. Chyatte, "A unique view on male infertility around the globe," *Reprod. Biol. Endocrinol.*, vol. 13, no. 1, p. 37, Dec. 2015, doi: 10.1186/s12958-015-0032-1.

[232] I. D. Sharlip, J. P. Jarow, A. M. Belker, L. I. Lipshultz, M. Sigman, A. J. Thomas, P. N. Schlegel, S. S. Howards, A. Nehra, M. D. Damewood, J. W. Overstreet, and R. Sadovsky, "Best practice policies for male infertility," *Fertil. Steril.*, vol. 77, no. 5, pp. 873–882, 2002, doi: 10.1016/S0015-0282(02)03105-9.

[233] "WHO | WHO Manual for the Standardized Investigation, Diagnosis and Management of the Infertile Male," *WHO*, 2014.

[234] "Male Infertility EAU Guidelines on," 2016.

[235] A. E. Carlson, T. A. Quill, R. E. Westenbroek, S. M. Schuh, B. Hille, and D. F. Babcock, "Identical Phenotypes of CatSper1 and CatSper2 Null Sperm," *J. Biol. Chem.*, vol. 280, no. 37, pp. 32238–32244, Sep. 2005, doi: 10.1074/jbc.M501430200.

[236] S. S. Suarez, "Control of hyperactivation in sperm," *Hum. Reprod. Update*, vol. 14, no. 6, pp. 647–657, Sep. 2008, doi: 10.1093/humupd/dmn029.

[237] A. E. Carlson, R. E. Westenbroek, T. Quill, D. Ren, D. E. Clapham, B. Hille, D. L. Garbers, and D. F. Babcock, "CatSper1 required for evoked Ca²⁺ entry and control of flagellar function in sperm," *Proc. Natl. Acad. Sci. U. S. A.*, vol. 100, no. 25, pp. 14864–8, Dec. 2003, doi: 10.1073/pnas.2536658100.

[238] J. Jin, N. Jin, H. Zheng, S. Ro, D. Tafolla, K. M. Sanders, and W. Yan, "Catsper3 and Catsper4 Are Essential for Sperm Hyperactivated Motility and Male Fertility in the Mouse1," *Biol. Reprod.*, vol. 77, no. 1, pp. 37–44, Jul. 2007, doi: 10.1095/biolreprod.107.060186.

[239] B. Navarro, Y. Kirichok, J.-J. Chung, and D. E. Clapham, "Ion channels that control fertility in mammalian spermatozoa," *Int. J. Dev. Biol.*, vol. 52, no. 5–6, pp. 607–613, 2008, doi: 10.1387/ijdb.072554bn.

[240] T. A. Quill, S. A. Sugden, K. L. Rossi, L. K. Doolittle, R. E. Hammer, and D. L. Garbers, "Hyperactivated sperm motility driven by CatSper2 is required for fertilization," *Proc. Natl. Acad. Sci. U. S. A.*, vol. 100, no. 25, pp. 14869–14874, Dec. 2003, doi: 10.1073/pnas.2136654100.

[241] J. F. Smith, O. Syritsyna, M. Fellous, C. Serres, N. Mannowetz, Y. Kirichok, and P. V Lishko, "Disruption of the principal, progesterone-activated sperm Ca²⁺ channel in a CatSper2-deficient infertile patient," *Proc. Natl. Acad. Sci. U. S. A.*, vol. 110, no. 17, pp. 6823–8,

9 References

Apr. 2013, doi: 10.1073/pnas.1216588110.

[242] S. Sumigama, S. Mansell, M. Miller, P. V Lishko, G. N. Cherr, S. A. Meyers, and T. Tollner, "Progesterone Accelerates the Completion of Sperm Capacitation and Activates CatSper Channel in Spermatozoa from the Rhesus Macaque.," *Biol. Reprod.*, vol. 93, no. 6, p. 130, Dec. 2015, doi: 10.1095/biolreprod.115.129783.

[243] W. Skinner, N. Mannowetz, P. Lishko, and N. Roan, "Single-cell Motility Analysis of Tethered Human Spermatozoa," *BIO-PROTOCOL*, vol. 9, no. 5, 2019, doi: 10.21769/bioprotoc.3182.

[244] A. L. Hodgkin and A. F. Huxley, "A quantitavie description of membrane current and its application to conduction and excitation in nerve," *J. Physiol. I*, vol. 7, pp. 500–544.

[245] E. Neher, B. Sakmann, and J. H. Steinbach, "The extracellular patch clamp: a method for resolving currents through individual open channels in biological membranes.," *Pflügers Arch. Eur. J. Physiol.*, vol. 375, no. 2, pp. 219–28, Jul. 1978.

[246] D. Lee, M. Kume, and T. E. Holy, "Sensory coding mechanisms revealed by optical tagging of physiologically defined neuronal types," *Science (80-)*, vol. 366, no. 6471, pp. 1384–1389, Dec. 2019, doi: 10.1126/science.aax8055.

[247] S. E. G. Lampe, B. K. Kaspar, and K. D. Foust, "Intravenous injections in neonatal mice," *J. Vis. Exp.*, no. 93, p. e52037, Nov. 2014, doi: 10.3791/52037.

[248] P. Thévenaz, U. E. Ruttimann, and M. Unser, "A pyramid approach to subpixel registration based on intensity," *IEEE Trans. Image Process.*, vol. 7, no. 1, pp. 27–41, 1998, doi: 10.1109/83.650848.

[249] M. Parvinen and A. Ruokonen, "Endogenous Steroids in the Rat Seminiferous Tubules. Comparison of the Stages of the Epithelial Cycle Isolated by Transillumination-Assisted Microdissection," *J. Androl.*, vol. 3, no. 4, pp. 211–220, Jul. 1982, doi: 10.1002/j.1939-4640.1982.tb00672.x.

[250] P. S. Tung and I. B. Fritz, "Characterization of Rat Testicular Peritubular Myoid Cells in Culture: α -Smooth Muscle Isoactin is a Specific Differentiation Marker1," *Biol. Reprod.*, vol. 42, no. 2, pp. 351–365, Dec. 1989, doi: 10.1095/biolreprod42.2.351.

[251] R. A. North, "Molecular physiology of P2X receptors," *Physiol. Rev.*, vol. 82, no. 4, pp. 1013–67, Oct. 2002, doi: 10.1152/physrev.00015.2002.

[252] D. L. Donnelly-Roberts, M. T. Namovic, P. Han, and M. F. Jarvis, "Mammalian P2X7 receptor pharmacology: comparison of recombinant mouse, rat and human P2X7 receptors," *Br. J. Pharmacol.*, vol. 157, no. 7, pp. 1203–1214, Aug. 2009, doi: 10.1111/j.1476-5381.2009.00233.x.

[253] C. Coddou, Z. Yan, T. Obsil, J. Pablo Huidobro-Toro, and S. S. Stojilkovic, "Activation and regulation of purinergic P2X receptor channels," *Pharmacol. Rev.*, vol. 63, no. 3, pp. 641–683, Sep. 2011, doi: 10.1124/pr.110.003129.

[254] B. S. Khakh, W. R. Proctor, T. V. Dunwiddie, C. Labarca, and H. A. Lester, "Allosteric control of gating and kinetics at P2X4 receptor channels," *J. Neurosci.*, vol. 19, no. 17, pp. 7289–7299, Sep. 1999, doi: 10.1523/jneurosci.19-17-07289.1999.

[255] R. J. Evans, C. Lewis, G. Buell, S. Valera, R. A. North, and A. Surprenant, "Pharmacological characterization of heterologously expressed ATP-gated cation channels (P2x purinoceptors).," *Mol. Pharmacol.*, vol. 48, no. 2, 1995.

9 References

[256] L. Smith, “Good planning and serendipity: Exploiting the Cre/Lox system in the testis,” *Reproduction*, vol. 141, no. 2. Reproduction, pp. 151–161, Feb. 2011, doi: 10.1530/REP-10-0404.

[257] A. Wirth, Z. Benyó, M. Lukasova, B. Leutgeb, N. Wettschureck, S. Gorbey, P. Orsy, B. Horváth, C. Maser-Gluth, E. Greiner, B. Lemmer, G. Schütz, S. Gutkind, and S. Offermanns, “G12-G13-LARG-mediated signaling in vascular smooth muscle is required for salt-induced hypertension,” *Nat. Med.*, vol. 14, no. 1, pp. 64–68, Jan. 2008, doi: 10.1038/nm1666.

[258] T. Strünker, N. Goodwin, C. Brenker, N. D. Kashikar, I. Weyand, R. Seifert, and U. B. Kaupp, “The CatSper channel mediates progesterone-induced Ca²⁺ influx in human sperm,” *Nature*, vol. 471, no. 7338, pp. 382–386, Mar. 2011, doi: 10.1038/nature09769.

[259] L. De Toni, A. Garolla, M. Menegazzo, S. Magagna, A. Di Nisio, I. Šabović, M. S. Rocca, V. Scattolini, A. Filippi, and C. Foresta, “Heat sensing receptor TRPV1 is a mediator of thermotaxis in human spermatozoa,” *PLoS One*, vol. 11, no. 12, pp. 1–18, 2016, doi: 10.1371/journal.pone.0167622.

[260] A. Kumar, R. K. Majhi, N. Swain, S. C. Giri, S. Kar, L. Samanta, and C. Goswami, “TRPV4 is endogenously expressed in vertebrate spermatozoa and regulates intracellular calcium in human sperm,” *Biochem. Biophys. Res. Commun.*, vol. 473, no. 4, pp. 781–788, 2016, doi: 10.1016/j.bbrc.2016.03.071.

[261] R. M. Borland, J. D. Biggers, C. P. Lechene, and M. L. Taymor, “Elemental composition of fluid in the human Fallopian tube.,” *J. Reprod. Fertil.*, vol. 58, no. 2, pp. 479–82, Mar. 1980.

[262] C. D. Benham, M. J. Gunthorpe, and J. B. Davis, “TRPV channels as temperature sensors,” *Cell Calcium*, vol. 33, pp. 479–487, 2003, doi: 10.1016/S0143-4160(03)00063-0.

[263] A. D. Güler, H. Lee, T. Iida, I. Shimizu, M. Tominaga, and M. Caterina, “Heat-evoked activation of the ion channel, TRPV4.,” *J. Neurosci.*, vol. 22, no. 15, pp. 6408–14, Aug. 2002, doi: 20026679.

[264] H. Watanabe, J. Vriens, S. H. Suh, C. D. Benham, G. Droogmans, and B. Nilius, “Heat-evoked activation of TRPV4 channels in a HEK293 cell expression system and in native mouse aorta endothelial cells.,” *J. Biol. Chem.*, vol. 277, no. 49, pp. 47044–51, Dec. 2002, doi: 10.1074/jbc.M208277200.

[265] W. Cheng, F. Yang, S. Liu, C. K. Colton, C. Wang, Y. Cui, X. Cao, M. X. Zhu, C. Sun, K. Wang, and J. Zheng, “Heteromeric Heat-sensitive Transient Receptor Potential Channels Exhibit Distinct Temperature and Chemical Response,” *J. Biol. Chem.*, vol. 287, no. 10, pp. 7279–7288, Mar. 2012, doi: 10.1074/jbc.M111.305045.

[266] T. Higuchi, T. Shimizu, T. Fujii, B. Nilius, and H. Sakai, “Gating modulation by heat of the polycystin transient receptor potential channel PKD2L1 (TRPP3),” *Pflugers Arch. Eur. J. Physiol.*, vol. 466, no. 10, pp. 1933–1940, Oct. 2014, doi: 10.1007/s00424-013-1439-1.

[267] C. Moore and W. B. Liedtke, *Osmomechanical-Sensitive TRPV Channels in Mammals*. 2017.

[268] A. K. Vogt-Eisele, K. Weber, M. A. Sherkheli, G. Vielhaber, J. Panten, G. Gisselmann, and H. Hatt, “Monoterpene agonists of TRPV3,” *Br. J. Pharmacol.*, vol. 151, no. 4, pp. 530–540, Jan. 2009, doi: 10.1038/sj.bjp.0707245.

9 References

[269] F. Vincent, A. Acevedo, M. T. Nguyen, M. Dourado, J. DeFalco, A. Gustafson, P. Spiro, D. E. Emerling, M. G. Kelly, and M. A. J. Duncton, “Identification and characterization of novel TRPV4 modulators,” *Biochem. Biophys. Res. Commun.*, vol. 389, no. 3, pp. 490–494, Nov. 2009, doi: 10.1016/j.bbrc.2009.09.007.

[270] M. J. Caterina, M. A. Schumacher, M. Tominaga, T. A. Rosen, J. D. Levine, and D. Julius, “The capsaicin receptor: a heat-activated ion channel in the pain pathway,” *Nature*, vol. 389, no. 6653, pp. 816–824, Oct. 1997, doi: 10.1038/39807.

[271] C. Harteneck, “Pregnenolone Sulfate: From Steroid Metabolite to TRP Channel Ligand,” *Molecules*, vol. 18, no. 10, pp. 12012–12028, Sep. 2013, doi: 10.3390/molecules181012012.

[272] S. Bevan, T. Quallo, and D. A. Andersson, “TRPV1,” in *Handbook of experimental pharmacology*, vol. 222, 2014, pp. 207–245.

[273] E. N. Senning, M. D. Collins, A. Stratiiievska, C. A. Ufret-Vincenty, and S. E. Gordon, “Regulation of TRPV1 ion channel by phosphoinositide (4,5)-bisphosphate: the role of membrane asymmetry,” *J. Biol. Chem.*, vol. 289, no. 16, pp. 10999–1006, Apr. 2014, doi: 10.1074/jbc.M114.553180.

[274] J. Vriens and T. Voets, “Sensing the heat with TRPM3,” *Pflügers Arch. - Eur. J. Physiol.*, vol. 470, no. 5, pp. 799–807, May 2018, doi: 10.1007/s00424-017-2100-1.

[275] W. Everaerts, X. Zhen, D. Ghosh, J. Vriens, T. Gevaert, J. P. Gilbert, N. J. Hayward, C. R. McNamara, F. Xue, M. M. Moran, T. Strassmaier, E. Uykal, G. Owsianik, R. Vennekens, D. De Ridder, B. Nilius, C. M. Fanger, and T. Voets, “Inhibition of the cation channel TRPV4 improves bladder function in mice and rats with cyclophosphamide-induced cystitis,” *Proc. Natl. Acad. Sci. U. S. A.*, vol. 107, no. 44, pp. 19084–9, Nov. 2010, doi: 10.1073/pnas.1005333107.

[276] D. M. Bautista, J. Siemens, J. M. Glazer, P. R. Tsuruda, A. I. Basbaum, C. L. Stucky, S. E. Jordt, and D. Julius, “The menthol receptor TRPM8 is the principal detector of environmental cold,” *Nature*, vol. 448, no. 7150, pp. 204–208, Jul. 2007, doi: 10.1038/nature05910.

[277] M. Maurer, N. Papotto, J. Sertel-Nakajima, M. Schueler, R. De Col, F. Möhrlen, K. Messlinger, S. Frings, and R. W. Carr, “Photoactivation of olfactory sensory neurons does not affect action potential conduction in individual trigeminal sensory axons innervating the rodent nasal cavity,” *PLoS One*, vol. 14, no. 8, Aug. 2019, doi: 10.1371/journal.pone.0211175.

[278] M. Diaz-Quesada, I. A. Youngstrom, Y. Tsuno, K. R. Hansen, M. N. Economo, and M. Wachowiak, “Inhalation frequency controls reformatting of mitral/tufted cell odor representations in the olfactory bulb,” *J. Neurosci.*, vol. 38, no. 9, pp. 2189–2206, Feb. 2018, doi: 10.1523/JNEUROSCI.0714-17.2018.

[279] M. Smear, R. Shusterman, R. O’Connor, T. Bozza, and D. Rinberg, “Perception of sniff phase in mouse olfaction,” *Nature*, vol. 479, no. 7373, pp. 397–400, Nov. 2011, doi: 10.1038/nature10521.

[280] J. L. Hurst, C. E. Payne, C. M. Nevison, A. D. Marie, R. E. Humphries, D. H. L. Robertson, A. Cavaggioni, and R. J. Beynon, “Individual recognition in mice mediated by major urinary proteins,” *Nature*, vol. 414, no. 6864, pp. 631–634, Dec. 2001, doi:

9 References

10.1038/414631a.

[281] I. Aprea, T. Nö The-Menchén, G. W. Dougherty, J. Raidt, N. T. Loges, T. Kaiser, J. Wallmeier, H. Olbrich, T. Strücker, S. Kliesch, P. Pennekamp, and H. Omran, "Motility of efferent duct cilia aids passage of sperm cells through the male reproductive system," doi: 10.1093/molehr/gaab009.

[282] M. Albrecht, R. Rämsch, F. M. Köhn, J. U. Schwarzer, and A. Mayerhofer, "Isolation and cultivation of human testicular peritubular cells: A new model for the investigation of fibrotic processes in the human testis and male infertility," *J. Clin. Endocrinol. Metab.*, vol. 91, no. 5, pp. 1956–1960, May 2006, doi: 10.1210/jc.2005-2169.

[283] F. Romano, A. Tripiciano, B. Muciaccia, P. De Cesaris, E. Ziparo, F. Palombi, and A. Filippini, "The contractile phenotype of peritubular smooth muscle cells is locally controlled: Possible implications in male fertility," *Contraception*, vol. 72, no. 4. Elsevier USA, pp. 294–297, Oct. 01, 2005, doi: 10.1016/j.contraception.2005.03.009.

[284] A. Mayerhofer, "Human testicular peritubular cells: More than meets the eye," *Reproduction*, vol. 145, no. 5. BioScientifica, pp. 145–107, May 01, 2013, doi: 10.1530/REP-12-0497.

[285] B. Pickering, S. D. Birkett, S. E. F. Guldenaar, H. D. Nicholson, R. T. S. Worley, and L. Yavachev, "Oxytocin in the Testis: What, Where, and Why?," *Ann. N. Y. Acad. Sci.*, vol. 564, no. 1 Regulation of, pp. 198–209, Jul. 1989, doi: 10.1111/j.1749-6632.1989.tb25898.x.

[286] J. L. Hargrove, R. R. Seeley, and L. C. Ellis, "Rabbit testicular contractions: bimodal interaction of prostaglandin E1 with other agonists," *Am. J. Physiol.*, vol. 228, no. 3, pp. 810–814, 1975, doi: 10.1152/ajplegacy.1975.228.3.810.

[287] O. Hovatta, "Contractility and structure of adult rat seminiferous tubules in organ culture," *Zeitschrift für Zellforsch. und mikroskopische Anat.*, vol. 130, no. 2, pp. 171–179, Jun. 1972, doi: 10.1007/BF00306955.

[288] B. Navarro, K. Miki, and D. E. Clapham, "ATP-activated P2X2 current in mouse spermatozoa," *Proc. Natl. Acad. Sci. U. S. A.*, vol. 108, no. 34, pp. 14342–14347, Aug. 2011, doi: 10.1073/pnas.1111695108.

[289] M. Tantama, "Activity-dependent ATP release from neurons and astrocytes," *FASEB J.*, vol. 33, no. S1, pp. 635.21-635.21, Apr. 2019, doi: 10.1096/FASEBJ.2019.33.1_SUPPLEMENT.635.21.

[290] J. Zhang, E. Kornecki, J. Jackman, and Y. H. Ehrlich, "ATP secretion and extracellular protein phosphorylation by CNS neurons in primary culture," *Brain Res. Bull.*, vol. 21, no. 3, pp. 459–464, Sep. 1988, doi: 10.1016/0361-9230(88)90159-1.

[291] I. Carneiro, M. A. Timóteo, I. Silva, C. Vieira, C. Baldaia, F. Ferreira, M. Silva-Ramos, and P. Correia-de-Sá, "Activation of P2Y₆ receptors increases the voiding frequency in anaesthetized rats by releasing ATP from the bladder urothelium," *Br. J. Pharmacol.*, vol. 171, no. 14, pp. 3404–3419, Jul. 2014, doi: 10.1111/bph.12711.

[292] B. Button, S. F. Okada, C. B. Frederick, W. R. Thelin, and R. C. Boucher, "Mechanosensitive ATP release maintains proper mucus hydration of airways," *Sci. Signal.*, vol. 6, no. 279, pp. ra46–ra46, Jun. 2013, doi: 10.1126/scisignal.2003755.

[293] M. Welsh, P. T. K. Saunders, N. Atanassova, R. M. Sharpe, and L. B. Smith, "Androgen

9 References

action via testicular peritubular myoid cells is essential for male fertility," *FASEB J.*, vol. 23, no. 12, pp. 4218–4230, Dec. 2009, doi: 10.1096/fj.09-138347.

[294] H. Welter, C. Kampfer, S. Lauf, R. Feil, J. U. Schwarzer, F.-M. Köhn, and A. Mayerhofer, "Partial loss of contractile marker proteins in human testicular peritubular cells in infertility patients," *Andrology*, vol. 1, no. 2, pp. 318–324, Mar. 2013, doi: 10.1111/j.2047-2927.2012.00030.x.

[295] D. Ren, B. Navarro, G. Perez, A. C. Jackson, S. Hsu, Q. Shi, J. L. Tilly, and D. E. Clapham, "A sperm ion channel required for sperm motility and male fertility," *Nature*, vol. 413, no. 6856, pp. 603–609, Oct. 2001, doi: 10.1038/35098027.

[296] S. G. Brown, S. J. Publicover, S. A. Mansell, P. V Lishko, H. L. Williams, M. Ramalingam, S. M. Wilson, C. L. R. Barratt, K. A. Sutton, and S. M. Da Silva, "Depolarization of sperm membrane potential is a common feature of men with subfertility and is associated with low fertilization rate at IVF," *Hum. Reprod.*, vol. 31, no. 6, pp. 1147–57, Jun. 2016, doi: 10.1093/humrep/dew056.

[297] T. K. Berger, D. M. Fußhöller, N. Goodwin, W. Bönigk, A. Müller, N. Dokani Khesroshahi, C. Brenker, D. Wachten, E. Krause, U. B. Kaupp, and T. Strünker, "Post-translational cleavage of Hv1 in human sperm tunes pH- and voltage-dependent gating," *J. Physiol.*, vol. 595, no. 5, pp. 1533–1546, Mar. 2017, doi: 10.1113/JP273189.

[298] C. Brenker, Y. Zhou, A. Müller, F. A. Echeverry, C. Trötschel, A. Poetsch, X.-M. Xia, W. Bönigk, C. J. Lingle, U. B. Kaupp, and T. Strünker, "The Ca^{2+} -activated K^+ current of human sperm is mediated by Slo3," *eLife*, vol. 3, p. e01438, Mar. 2014, doi: 10.7554/eLife.01438.

[299] Y. Geng, J. J. Ferreira, V. Dzikunu, A. Butler, P. Lybaert, P. Yuan, K. L. Magleby, L. Salkoff, and C. M. Santi, "A genetic variant of the sperm-specific SLO3 K^+ channel has altered pH and Ca^{2+} sensitivities," *J. Biol. Chem.*, vol. 292, no. 21, pp. 8978–8987, May 2017, doi: 10.1074/jbc.M117.776013.

[300] H. L. Williams, S. Mansell, W. Alasmari, S. G. Brown, S. M. Wilson, K. A. Sutton, M. R. Miller, P. V. Lishko, C. L. R. Barratt, S. J. Publicover, and S. Martins da Silva, "Specific loss of CatSper function is sufficient to compromise fertilizing capacity of human spermatozoa," *Hum. Reprod.*, vol. 30, no. 12, p. dev243, Oct. 2015, doi: 10.1093/humrep/dev243.

[301] G. Orta, G. Ferreira, O. José, C. L. Treviño, C. Beltrán, and A. Darszon, "Human spermatozoa possess a calcium-dependent chloride channel that may participate in the acrosomal reaction," *J. Physiol.*, vol. 590, no. 11, pp. 2659–75, Jun. 2012, doi: 10.1113/jphysiol.2011.224485.

[302] T. T. Turner, P. K. Hartmann, and S. S. Howards, "In vivo sodium, potassium, and sperm concentrations in the rat epididymis," *Fertil. Steril.*, vol. 28, no. 2, pp. 191–194, 1977, doi: 10.1016/s0015-0282(16)42382-4.

[303] A. Valeri, D. Mianné, F. Merouze, L. Bujan, A. Altobelli, and J. Masson, "Scrotal temperature in 258 healthy men, randomly selected from a population of men aged 18 to 23 years old. Statistical analysis, epidemiologic observations, and measurement of the testicular diameters," *Prog. Urol.*, vol. 3, no. 3, pp. 444–52, Jun. 1993.

[304] A. Bahat, I. Tur-Kaspa, A. Gakamsky, L. C. Giojalas, H. Breitbar, and M. Eisenbach,

9 References

“Thermotaxis of mammalian sperm cells: A potential navigation mechanism in the female genital tract,” *Nat. Med.*, vol. 9, no. 2, pp. 1–2, 2003, doi: 10.1038/nm0203-149.

[305] S. Norris, “Basal body temperature in ovulation,” *Can. Med. Assoc. J.*, vol. 67, no. 4, pp. 336–338, Oct. 1952.

[306] K. Ho, C. A. Wolff, and S. S. Suarez, “CatSper-null mutant spermatozoa are unable to ascend beyond the oviductal reservoir,” *Reprod. Fertil. Dev.*, vol. 21, no. 2, pp. 345–50, 2009.

[307] M. E. Teves, H. A. Guidobaldi, D. R. Uñates, R. Sanchez, W. Miska, S. J. Publicover, A. A. M. Garcia, and L. Giojalas, “Molecular mechanism for human sperm chemotaxis mediated by progesterone,” *PLoS One*, vol. 4, no. 12, p. 8211, 2009, doi: 10.1371/journal.pone.0008211.

[308] M. R. El-Talatini, A. H. Taylor, J. C. Elson, L. Brown, A. C. Davidson, and J. C. Konje, “Localisation and function of the endocannabinoid system in the human ovary,” *PLoS One*, vol. 4, no. 2, p. e4579, 2009, doi: 10.1371/journal.pone.0004579.

[309] R. H. F. Hunter and H. Rodriguez-Martinez, “Capacitation of mammalian spermatozoa in vivo, with a specific focus on events in the fallopian tubes,” *Mol. Reprod. Dev.*, vol. 67, no. 2, pp. 243–250, Feb. 2004, doi: 10.1002/mrd.10390.

[310] H. Watanabe, J. Vriens, A. Janssens, R. Wondergem, G. Droogmans, and B. Nilius, “Modulation of TRPV4 gating by intra- and extracellular Ca^{2+} ,” *Cell Calcium*, vol. 33, no. 5–6, pp. 489–95, 2003.

[311] C. B. Phelps, R. R. Wang, S. S. Choo, and R. Gaudet, “Differential regulation of TRPV1, TRPV3, and TRPV4 sensitivity through a conserved binding site on the ankyrin repeat domain,” *J. Biol. Chem.*, vol. 285, no. 1, pp. 731–740, 2010, doi: 10.1074/jbc.M109.052548.

[312] P. V. Lishko, E. Procko, X. Jin, C. B. Phelps, and R. Gaudet, “The Ankyrin Repeats of TRPV1 Bind Multiple Ligands and Modulate Channel Sensitivity,” *Neuron*, vol. 54, no. 6, pp. 905–918, Jun. 2007, doi: 10.1016/j.neuron.2007.05.027.

[313] P. E. Visconti, D. Krapf, J. L. de la Vega-Beltrán, J. J. Acevedo, and A. Darszon, “Ion channels, phosphorylation and mammalian sperm capacitation,” *Asian J. Androl.*, vol. 13, no. 3, pp. 395–405, May 2011, doi: 10.1038/aja.2010.69.

[314] T. Wegierski, U. Lewandrowski, B. Müller, A. Sickmann, and G. Walz, “Tyrosine phosphorylation modulates the activity of TRPV4 in response to defined stimuli,” *J. Biol. Chem.*, vol. 284, no. 5, pp. 2923–33, Jan. 2009, doi: 10.1074/jbc.M805357200.

[315] K.-I. Hamano, T. Kawanishi, A. Mizuno, M. Suzuki, and Y. Takagi, “Involvement of Transient Receptor Potential Vanilloid (TRPV) 4 in mouse sperm thermotaxis,” *J. Reprod. Dev.*, vol. 62, no. 4, pp. 415–22, Aug. 2016, doi: 10.1262/jrd.2015-106.

[316] P. G. Decaen, M. Delling, T. N. Vien, and D. E. Clapham, “Direct recording and molecular identification of the calcium channel of primary cilia,” *Nature*, vol. 504, no. 7479, pp. 315–318, 2013, doi: 10.1038/nature12832.

[317] X. Liu, T. Vien, J. Duan, S. H. Sheu, P. G. DeCaen, and D. E. Clapham, “Polycystin-2 is an essential ion channel subunit in the primary cilium of the renal collecting duct epithelium,” *eLife*, vol. 7, Feb. 2018, doi: 10.7554/eLife.33183.

[318] S. Field, K.-L. Riley, D. T. Grimes, H. Hilton, M. Simon, N. Powles-Glover, P. Siggers, D.

9 References

Bogani, A. Greenfield, and D. P. Norris, "Pkd1l1 establishes left-right asymmetry and physically interacts with Pkd2," *Development*, vol. 138, no. 6, pp. 1131–1142, Mar. 2011, doi: 10.1242/dev.058149.

[319] G. J. Pazour, J. T. San Agustin, J. A. Follit, J. L. Rosenbaum, and G. B. Witman, "Polycystin-2 localizes to kidney cilia and the ciliary level is elevated in orpk mice with polycystic kidney disease," *Current Biology*, vol. 12, no. 11. Curr Biol, pp. R378–R380, Jun. 04, 2002, doi: 10.1016/S0960-9822(02)00877-1.

[320] S. M. Nauli, F. J. Alenghat, Y. Luo, E. Williams, P. Vassilev, X. Li, A. E. H. Elia, W. Lu, E. M. Brown, S. J. Quinn, D. E. Ingber, and J. Zhou, "Polycystins 1 and 2 mediate mechanosensation in the primary cilium of kidney cells," *Nat. Genet.*, vol. 33, no. 2, pp. 129–137, Feb. 2003, doi: 10.1038/ng1076.

[321] Y. Chen, Z. Zhang, X. Y. Lv, Y. D. Wang, Z. G. Hu, H. Sun, R. Z. Tan, Y. H. Liu, G. H. Bian, Y. Xiao, Q. W. Li, Q. T. Yang, J. Z. Ai, L. Feng, Y. Yang, Y. Q. Wei, and Q. Zhou, "Expression of Pkd2l2 in testis is implicated in spermatogenesis," *Biol. Pharm. Bull.*, vol. 31, no. 8, pp. 1496–1500, Aug. 2008, doi: 10.1248/bpb.31.1496.

[322] N. Vora, R. Perrone, and D. W. Bianchi, "Reproductive Issues for Adults With Autosomal Dominant Polycystic Kidney Disease," *American Journal of Kidney Diseases*, vol. 51, no. 2. Am J Kidney Dis, pp. 307–318, Feb. 2008, doi: 10.1053/j.ajkd.2007.09.010.

[323] M. Li Vecchi, P. Cianfrone, R. Damiano, and G. Fuiano, "Infertility in adults with polycystic kidney disease," *Nephrol. Dial. Transplant.*, vol. 18, no. 1, pp. 190–191, Jan. 2003, doi: 10.1093/ndt/18.1.190.

[324] H. Okada, H. Fujioka, N. Tatsumi, M. Fujisawa, K. Gohji, S. Arakawa, H. Kato, S. I. Kobayashi, S. Isojima, and S. Kamidono, "Assisted reproduction for infertile patients with 9 + 0 immotile spermatozoa associated with autosomal dominant polycystic kidney disease," *Hum. Reprod.*, vol. 14, no. 1, pp. 110–113, 1999, doi: 10.1093/humrep/14.1.110.

[325] M. K. Chung, H. Lee, and M. J. Caterina, "Warm temperatures activate TRPV4 in mouse 308 keratinocytes," *J. Biol. Chem.*, vol. 278, no. 34, pp. 32037–32046, Aug. 2003, doi: 10.1074/jbc.M303251200.

[326] K. Shibasaki, M. Suzuki, A. Mizuno, and M. Tominaga, "Effects of body temperature on neural activity in the hippocampus: Regulation of resting membrane potentials by transient receptor potential vanilloid 4," *J. Neurosci.*, vol. 27, no. 7, pp. 1566–1575, Feb. 2007, doi: 10.1523/JNEUROSCI.4284-06.2007.

[327] X. Ma, K. T. Cheng, C. O. Wong, R. G. O'Neil, L. Birnbaumer, I. S. Ambudkar, and X. Yao, "Heteromeric TRPV4-C1 channels contribute to store-operated Ca²⁺ entry in vascular endothelial cells," *Cell Calcium*, vol. 50, no. 6, pp. 502–509, 2011, doi: 10.1016/j.ceca.2011.08.006.

[328] L. Michalick, "TRPV4 in Ventilator-induced Lung Injury – Mechanisms of Endothelial Mechanotransduction and Barrier Regulation in the Lung," Dissertation, FU Berlin, 2017.

[329] K. Ha, M. Nobuhara, Q. Wang, R. V. Walker, F. Qian, C. Schartner, E. Cao, and M. Delling, "The heteromeric pc-1/pc-2 polycystin complex is activated by the pc-1 n-terminus," *Elife*, vol. 9, pp. 1–23, Oct. 2020, doi: 10.7554/eLife.60684.

[330] Y. Yu, M. H. Ulbrich, M. H. Li, S. Dobbins, W. K. Zhang, L. Tong, E. Y. Isacoff, and J. Yang,

9 References

“Molecular mechanism of the assembly of an acid-sensing receptor ion channel complex,” *Nat. Commun.*, vol. 3, p. 1252, 2012, doi: 10.1038/ncomms2257.

[331] Q. Su, F. Hu, X. Ge, J. Lei, S. Yu, T. Wang, Q. Zhou, C. Mei, and Y. Shi, “Structure of the human PKD1-PKD2 complex,” *Science (80-.)*, vol. 361, no. 6406, p. eaat9819, Sep. 2018, doi: 10.1126/science.aat9819.

[332] J. Bedford, “Effects of elevated temperature on the epididymis and testis: experimental studies,” *Adv Exp Med Biol.*, vol. 286, pp. 19–32, 1991.

[333] F. Pouille and N. E. Schoppa, “Cannabinoid Receptors Modulate Excitation of an Olfactory Bulb Local Circuit by Cortical Feedback,” *Front. Cell. Neurosci.*, vol. 12, no. March, pp. 1–15, 2018, doi: 10.3389/fncel.2018.00047.

[334] V. Lage-Rupprecht, L. Zhou, G. Bianchini, S. S. Aghvami, M. Mueller, B. Rózsa, M. Sassoè-Pognetto, and V. Egger, “Presynaptic nmdars cooperate with local spikes toward gaba release from the reciprocal olfactory bulb granule cell spine,” *eLife*, vol. 9, pp. 1–27, Oct. 2020, doi: 10.7554/eLife.63737.

[335] G. C. R. Ellis-Davies, “Two-Photon Uncaging of Glutamate,” *Front. Synaptic Neurosci.*, vol. 10, p. 48, Jan. 2019, doi: 10.3389/fnsyn.2018.00048.

[336] E. Demir, K. Li, N. Bobrowski-Khoury, J. I. Sanders, R. J. Beynon, J. L. Hurst, A. Kepecs, and R. Axel, “The pheromone darcin drives a circuit for innate and reinforced behaviours,” *Nature*, vol. 578, no. 7793, pp. 137–141, Feb. 2020, doi: 10.1038/s41586-020-1967-8.

[337] T. Ackels, “Physiological investigation of chemosensory mechanisms in the mammalian olfactory and vomeronasal system,” *Diss. RWTH Aachen Univ.*, 2015.

[338] L. Lo and D. J. Anderson, “A Cre-dependent, anterograde trans-synaptic viral tracer for mapping output pathways of genetically marked neurons,” *Neuron*, 2011, doi: 10.1016/j.neuron.2011.12.002.

10 Acknowledgement

Diese Arbeit wäre nicht zu realisieren gewesen ohne den wesentlichen Beitrag einiger Menschen, bei denen ich mich ganz herzlich bedanken möchte.

An erster Stelle gilt mein Dank meinem Doktorvater Prof. Dr. Marc Spehr, welcher mich seit nunmehr sieben Jahren wissenschaftlich begleitet und unterstützt. Durch deine ausgeprägte Leidenschaft für die Wissenschaft hast du auch mich angesteckt und durchweg motiviert. Danke, für deine Unterstützung und dein Vertrauen in mich und die Möglichkeit meine wissenschaftliche Selbstständigkeit zu üben. Du hast mich stets gefordert, sodass ich nicht nur wissenschaftlich, sondern auch persönlich während meiner Zeit in deinem Labor wachsen durfte. Ich bedanke mich außerdem für die Unterstützung bei der Umsetzung meines Forschungsaufenthaltes in den USA, sowie der Möglichkeit an internationalen Konferenzen teilnehmen zu können. Ich freue mich auf eine weitere Zusammenarbeit in der Zukunft mit dir.

I wish to express my sincerest gratitude to Prof. Polina Lishko for the opportunity to learn and research in her laboratory at UC Berkeley. Thank you for letting me work on such an interesting project and for granting me the independence I needed. I appreciate all the fruitful scientific discussions during my stay and the kind working atmosphere among all members of the Lishko group inside and outside of work. I left with a much broader scientific and personal horizon. Thank you all so much!

Ein weiteres Dankeschön geht an alle ehemaligen und derzeitigen Mitglieder der AG Chemosensorik. Ich werde meine Zeit mit euch sehr vermissen und kann mir nur wünschen, dass ich auch in Zukunft in einem so kollegialen und unterstützenden Umfeld arbeiten darf. I want to thank my collaborators - Prof. Artur Mayerhofer, Prof. Herman Wagner, Em. Prof. Rob Beynon, and Prof. Jeremy McIntyre - for constructive cooperation and much appreciated support of my research.

I am a member of the RTG2416 Multisenses-Multiscales and would like to thank the German Research Foundation (DFG) for funding as well as the German Academic Exchange Service (DAAD) for financial support during my research abroad.

10 Acknowledgement

Schlussendlich gilt mein größter Dank meinen Eltern und meinem Partner Daniel. Es ist nur schwer in Worte zu fassen wie sehr eure Unterstützung zu meinem Gelingen beigetragen hat. Danke für euer Interesse, eure endlose Geduld mit mir und eure warmen Worte an kritischen Tagen. Ich bin so froh euch zu haben!

11 Curriculum vitae

Contact information:

Name: Nadine Mundt
E-mail: n.mundt@sensorik.rwth-aachen.de

Personal information:

Date of Birth: 20.05.1992
Place of Birth: Düren-Birkesdorf, Germany
Citizenship: German

Education:

09/2016 Master of Science in Biology, RWTH Aachen University
(with distinction)
09/2014 Bachelor of Science in Biology, RWTH Aachen University
05/2011 Allgemeine Hochschulreife, Franken-Gymnasium Zülpich

Research Experience:

09/2018-present Research Training Group RTG2416, German Research Foundation
06/2017-present Doctoral studies at RWTH Aachen University,
Dept. of Chemosensation, PI: Prof. Dr. Marc Spehr
06/2017 - 08/2018 Junior specialist, University of California in Berkeley,
Dept. of Molecular and Cellular Biology,
PI: Associate professor Polina Lishko, PhD
10/2015 - 09/2016 Master thesis work at RWTH Aachen University,
Dept. of Chemosensation, PI: Prof. Dr. Marc Spehr
10/2014 - 10/2015 Student assistant at RWTH Aachen University,
Dept. of Chemosensation, PI: Prof. Dr. Marc Spehr
12/2013 - 09/2014 Bachelor thesis work at RWTH Aachen University,
Dept. of Chemosensation, PI: Prof. Dr. Marc Spehr

Teaching experience:

05/2018 Teaching instructor at "Frontiers in Reproduction: Molecular and Cellular Concepts and Applications- 2018" course, Marine Biological Laboratory; Woods Hole, MA, USA. Co-taught the sperm electrophysiology method and ion channel measurement techniques

2016 to present Teaching instructor in the practical animal physiology course Bachelor level, RWTH Aachen University

2019 and 2020 Lecturer in the animal physiology module, Reproduction, Bachelor level, RWTH Aachen University

Publication list:

Bachelor's thesis: "Analysis of the molecular and cellular fundamentals of spermatogenesis in mice" (excellent; 1.0), RWTH Aachen University, September 2014

Master's thesis: "Physiological analysis of purinergic signaling mechanisms in the mouse testes" (excellent; 1.0), RWTH Aachen University, September 2016

Publications (peer-reviewed):

- Fleck D, **Mundt N**, Bruentgens F, Machado P, Veitinger T, Veitinger S, Engelhardt CH, Spehr J, Spehr M: Distinct purinergic signaling pathways in prepubescent mouse spermatogonia, *Journal of General Physiology* (2016)
- Mannowetz N, **Mundt N**, Lishko PV: Reply to Brenker et al.: The plant triterpenoid pristimerin inhibits calcium influx into human spermatozoa via CatSper, *PNAS* (2018)
- Mundt N**, Spehr M, Lishko PV: TRPV4 is the temperature sensitive ion channel of human sperm, *eLife* (2018)
- Fleck D, Kenzler L, **Mundt N**, Strauch M, Uesaka N, Moosmann R, Brüntgens F, Missel A, Mayerhofer A, Merhof

D, Spehr J, Spehr M: ATP activation of peritubular cells drives testicular sperm transport, eLife (2021)

Liu B, **Mundt N**, Miller M, Clapham D, Kirichok Y, Lishko PV: Recording Electrical Currents across the Plasma Membrane of Mammalian Sperm Cells, JoVE (2021)

Piedrahita P, Krings M, Nikolay P, **Mundt N**, Quezada G, Masaquiza E, Wagner H: Integrity of and damage to wings, feather vanes and serrations of barn owls, Zoology (2021)

Missel A, Walenta L, Eubler K, **Mundt N**, Heikelä H, Pickl U, Trottmann M, Popper B, Poutanen M, Strauss L, Köhn FM, Kunz L, Spehr M, Mayerhofer A: Testicular adenosine acts as a pro-inflammatory molecule: role of testicular peritubular cells, Molecular Human Reproduction (2021)

Conference posters: "Immunohistochemical characterization of purinoceptor expression during spermatogenesis" Purines 2014, Bonn (GER), July 2014

"Immunohistochemical characterization of purinoceptor expression during spermatogenesis" SSR 2015, 48th Annual Meeting of the Society for the Study of Reproduction, San Juan, Puerto Rico (USA), June 2015

"TRPV4 is the temperature-sensitive ion channel of human sperm" Göttingen Meeting of the German Neuroscience society, Göttingen (GER), 2019

Conference talks: Platform Presentation and Session Chair: "DSper – The Depolarizing Channel of Human Sperm", Biophysical Society Meeting, San Francisco (USA), February 2018

Oral presentation:
"DSper - The Depolarizing Channel of Human Sperm",

Tracking Life Symposium at RWTH Aachen University, Aachen (GER), October 2018

Platform Presentation:
"DSper – The Depolarizing Channel of Human Sperm".
52th Meeting of the Society for the Study of Reproduction, San Jose (USA), July 2019

Coordinator, host, and lecturer of the "Women in Academia day 2019", RTG 2416, RWTH Aachen University, August 2019

Awards and Grants:

10/2015 – 09/2016	Deutschlandstipendium
2016	Dean's list RWTH Aachen University
2016	Springorum Denkmünze, RWTH Aachen University
06/2017 – 05/2018:	Jahresstipendium DAAD: Governmental fellowship for PhD students working abroad
2019:	"Best International Abstract Award" by the Society for the Study of Reproduction
2019:	Trainee Travel Award by the SSR to attend the annual meeting of the Society for the Study of Reproduction in San Jose (USA)
2019:	Travel Award by the Male Contraceptive Initiative to attend the annual meeting of the Society for the Study of Reproduction in San Jose (USA)
2020:	Nomination and Invitation to attend the 70th multidisciplinary Nobel Laureate Meeting in Lindau (GER)

12 Eidesstattliche Erklärung

Nadine Mundt

erklärt hiermit, dass diese Dissertation und die darin dargelegten Inhalte die eigenen sind und selbstständig, als Ergebnis der eigenen originären Forschung, generiert wurden.

Hiermit erkläre ich an Eides statt:

1. Diese Arbeit wurde vollständig oder größtenteils in der Phase als Doktorandin dieser Fakultät und Universität angefertigt;
2. Sofern irgendein Bestandteil dieser Dissertation zuvor für einen akademischen Abschluss oder eine andere Qualifikation an dieser oder einer anderen Institution verwendet wurde, wurde dies klar angezeigt;
3. Wenn immer andere eigene- oder Veröffentlichungen Dritter herangezogen wurden, wurden diese klar benannt;
4. Wenn aus anderen eigenen- oder Veröffentlichungen Dritter zitiert wurde, wurde stets die Quelle hierfür angegeben. Diese Dissertation ist vollständig meine eigene Arbeit, mit der Ausnahme solcher Zitate;
5. Alle wesentlichen Quellen von Unterstützung wurden benannt;
6. Wenn immer ein Teil dieser Dissertation auf der Zusammenarbeit mit anderen basiert, wurde von mir klar gekennzeichnet, was von anderen und was von mir selbst erarbeitet wurde;
7. Teile dieser Arbeit wurden zuvor veröffentlicht und zwar in: eLife (DOI: 10.7554/eLife.35853 und DOI: 10.7554/eLife.62885)

Datum: 25.05.2021

Unterschrift